

DISS. ETH NO. 25219

# **Linkage between fracture network, stress heterogeneities and induced seismicity in deep geothermal reservoirs**

A thesis submitted to attain the degree of  
DOCTOR OF SCIENCES of ETH ZURICH  
(Dr. sc. ETH Zurich)

presented by

**Mohammad Javad Afshari Moein**

M.Sc. Reservoir Geoscience and Engineering,  
École Nationale Supérieure du Pétrole et des Moteurs (IFP School)

born on 08.04.1988

citizen of Iran

accepted on the recommendation of

Prof. Dr. Simon Löw, examiner  
Prof. Dr. Benoît Valley, co-examiner  
Dr. Keith Evans, co-examiner  
Prof. Dr. Olivier Bour, external examiner

2018



# Abstract

---

Enhanced Geothermal Systems (EGS) intend to extract the heat stored in the earth's crust by circulating a fluid like water between injection and production wells. The heat exchange between the fluid and high temperature (ideally higher than 150°C) host rocks permits producing energy from production fluid. Since the host formations of desirable temperatures are mostly found in crystalline low-porosity basement rocks, the fluid flow is developed through the fracture network. However, the natural production rate from these reservoirs are typically lower than economic thresholds. Thus, commercial developments of EGS reservoirs require permeability enhancement or creation through hydraulic stimulation, in which massive pressurized fluid is injected into the target reservoir. High pressure fluid injection increases the pore pressure and reduces the effective normal stress on fracture planes, and results in shearing of rough surfaces or creating new fractures that are expected to enhance the permeability of the rock mass. However, displacement on fracture surfaces induces microseismicity, which may include destructive events, too. This particular problem has led to suspension of two geothermal projects in Basel and Saint-Gallen, Switzerland. Hence, the main challenge in developing commercial geothermal developments is to enhance the permeability without inducing damaging events.

Induced seismicity is a complex interaction between pre-existing fracture network, pore-pressure propagation and in-situ stress conditions. Thus the preliminary step towards a reliable seismic risk and hazard assessment, is characterizing the fracture network in different scales. Nevertheless, fracture network characterization is a challenging task at early project stages, especially when a single borehole penetrates the target reservoir. The primary source of information on the natural fractures within the reservoir volume stems from the borehole data. In addition to that, induced seismicity reveals some information on the 3D structures within the reservoir volume, too. Furthermore, the local stress heterogeneities in borehole scale is largely controlled by the slip on fractures and geometrical characteristics of the network. Thus, the potential relations amongst the fracture network, stress heterogeneities and induced seismicity would result in practical implications such as constraining the 3D clustering and length distribution of fracture as well as maximum seismic magnitude forecast during the hydraulic stimulation.

The preliminary step toward exploring these relations is to characterize the fracture network from borehole data. Borehole data may be characterized by scaling laws to study potential scale-invariance and possibly relate it to the scaling of stress heterogeneity and induced seismicity. Before establishing such relations, the limitations of fracture network sampling and power-law scaling of borehole data should be clarified. Detailed analysis of synthetic and borehole data clarified that the correlation function delivers the true fractal dimension of fracture patterns. The analysis of natural fractures derived from borehole images of two geothermal reservoirs of Basel and Soultz-sous-Forêts confirmed the fractal spacing of fracture sets and the entire

datasets, in more than two order of magnitude. Further analysis on the synthetic 3D fractal fracture networks (a network in which the spatial distribution of fracture centers are scale-invariant and the fracture length follows a power-law distribution) revealed the possible limitations and associated uncertainty of using available stereological relationships (the relationships among the 1D, 2D and 3D spatial distribution of fractures in a fractal network). Further analysis on the available borehole data showed no clear trend of correlation dimension with depth.

Induced seismicity patterns also tend to exhibit scale-invariant characteristics. A detailed analysis on the seismicity in the Basel geothermal reservoir exhibited the potential scaling relationships in clustering and size distribution of induced events. Synthetic fracture networks as a representative of rupture planes interpreted the clustering and size distribution of induced events and clarified the effect of microseismic specific influential factors such as hypocentral location uncertainties, existence of a fractured zone and repeating events on the observed seismicity. The similarity between the scaling characteristics of induced seismicity and fractal fracture networks led to introduce a statistical seismicity model, which includes the spatial clustering and size distribution of potential rupture planes. This model could forecast the maximum seismic magnitude of induced events based on the scaling of early seismicity patterns in hydraulic stimulation with increasing injection time and stimulated volume.

Adopting the hypothesis that stress heterogeneities are strongly controlled by natural fractures and their geometrical characteristics, a novel stress-based tomography was developed in a Bayesian framework. This inversion technique is capable to characterize the fracture network and its heterogeneity in deep geothermal resources. This technique used local variations of in-situ principal stress components (at least one orientation and one magnitude) along boreholes and the prior information on the fracture network. The Markov sequence compared the simulated stress profile with the observed stress profiles on the borehole and accepted possible realizations using Metropolis-Hastings (MH) acceptance criteria. The Markov Chain Monte Carlo (MCMC) algorithm stored a large number of realizations in an ensemble. Then, a selection of accepted realizations visualized the possible fracture locations and corresponding lengths in a fracture probability map. This technique was successfully tested on simple synthetic and complex outcrop-based fracture networks.

Finally, the stress heterogeneities in borehole scale shows scale-invariant characteristics in different wavelengths. Adopting the same hypothesis that the stress heterogeneities are controlled by slip on natural fractures, 2D fracture networks were generated to relate the scaling of stress heterogeneities and key network characteristics. Analysis on the synthetic data showed weak reverse correlation between the fracture length exponent and fractal dimension of stress heterogeneities. In addition, fracture density largely affected the stress profiles on boreholes.



# Zusammenfassung

---

Enhanced Geothermal Systems (EGS) sollen die in der Erdkruste gespeicherte Wärme durch die Zirkulation einer Flüssigkeit, wie zum Beispiel Wasser, zwischen Injektions- und Produktionsbrunnen fördern. Der Wärmeaustausch zwischen der Flüssigkeit und dem Hochtemperatur-Wirtsgestein (idealerweise höher als 150 ° C) erlaubt die Erzeugung von Energie aus der Produktionsflüssigkeit. Da die Wirtformationen der gewünschten Temperaturen meist in niedrigporösen Kristallin-Gesteinen vorkommen, findet der Flüssigfluss in Bruchnetzwerken statt. Die natürliche Produktionsrate aus diesen Lagerstätten ist jedoch typischerweise niedriger als die erforderlichen Schwellenwerte für eine wirtschaftliche Produktion. Daher erfordern kommerzielle Entwicklungen von EGS-Reservoirs eine Verbesserung der Permeabilität durch hydraulische Stimulationen, bei der Fluide unter Hochdruck in das Ziel-Reservoir gepresst werden. Die Hochdruckinjektion von Fluiden erhöht den Porendruck, reduziert die effektive Normalspannung auf Bruchebenen und führt zum Scheren entlang rauher Oberflächen oder zur Erzeugung neuer Risse, von denen erwartet wird, dass sie die Durchlässigkeit der Gesteinsmasse erhöhen. Verschiebungen an Bruchflächen induzieren jedoch Mikroseismizität, was auch spürbare und zerstörerische Folgen beinhalten kann. Dieses spezielle Problem hat bereits dazu geführt, dass zwei EGS-Projekte in der Schweiz in den Geothermieanlagen Basel und St. Gallen eingestellt wurden. Daher besteht die größte Herausforderung bei der Entwicklung kommerzieller EGS-Entwicklungen darin, die Durchlässigkeit zu erhöhen, ohne schädliche Ereignisse hervorzurufen.

Induzierte Seismizität ist eine komplexe Wechselwirkung zwischen bereits bestehendem Bruchnetzwerk, Porendruckausbreitung und in-situ Spannungsbedingungen. Der vorbereitende Schritt hin zu einer zuverlässigen seismischen Risiko- und Gefährdungsbeurteilung charakterisiert somit das Bruchnetzwerk in verschiedenen Maßstäben. Dennoch ist die Charakterisierung von Bruchnetzwerken eine Herausforderung in frühen Projektphasen, insbesondere, wenn lediglich ein einzelnes Bohrloch das Zielreservoir durchdringt. Die primäre Quelle für Informationen über die natürlichen Brüche innerhalb des Reservoirvolumens stammt aus diesen Bohrlochdaten. Zusätzlich zeigt die induzierte Seismizität auch Informationen über die 3D-Strukturen innerhalb des Reservoirvolumens. Darüber hinaus werden die lokalen Spannungsheterogenitäten im Bohrlochmaßstab weitgehend durch Scherversatz entlang existierender Brüche und die geometrischen Eigenschaften des Netzwerks gesteuert. Die potentiellen Beziehungen zwischen dem Bruchnetzwerk, den Spannungsheterogenitäten und der induzierten Seismizität würden somit zu praktischen Implikationen führen, wie zum Beispiel das Einschränken der 3D-Clusterbildung und der Längenverteilung der Brüche, sowie die Vorhersage des maximalen seismischen Magnitude während der hydraulischen Stimulation. Der vorläufige Schritt zur Erforschung dieser Beziehungen ist eine Charakterisierung des Bruchnetzwerks anhand von Bohrlochdaten. Bohrlochdaten können durch Skalierungsgesetze charakterisiert werden, um potentielle Skaleninvarianz zu untersuchen und möglicherweise mit

der Skalierung von Stressheterogenität und induzierter Seismizität in Beziehung zu setzen. Bevor solche Beziehungen hergestellt werden, sollten die Grenzen der Bruchnetz-Probenahme und der potenzgesetz Skalierung von Bohrlochdaten geklärt werden. Eine detaillierte Analyse von synthetischen Daten und Bohrlochdaten verdeutlichte, dass die Korrelationsfunktion die wahre fraktale Dimension von Bruchmustern liefert. Die Analyse von natürlichen Brüchen aus Bohrbildern von zwei geothermischen Reservoiren (Basel und Soultz-sous-Forêts) bestätigte das fraktale Verhalten von Brüchen und der gesamten Datensätze in mehr als zwei Größenordnungen. Eine weitere Analyse der synthetischen fraktalen 3D-Bruchnetzwerke (ein Netzwerk, in dem die räumliche Verteilung der Bruchzentren skaleninvariant ist und die Bruchlänge einer Potenzgesetzverteilung folgt) hat die möglichen Einschränkungen und die damit verbundene Unsicherheit der Verwendung verfügbarer stereologischer Beziehungen (der Beziehungen aufgezeigt unter der 1D, 2D und 3D räumlichen Verteilung von Brüchen in einem fraktalen Netzwerk). Eine weitere Analyse der verfügbaren Bohrlochdaten zeigte keinen eindeutigen Trend der Korrelationsdimension mit der Tiefe.

Induzierte Seismizitätsmuster neigen auch dazu, skaleninvariante Eigenschaften aufzuweisen. Eine detaillierte Analyse der Seismizität im geothermischen Reservoir in Basel zeigte die potenziellen Skalierungsbeziehungen in der Clusterbildung und Größenverteilung von induzierten Ereignissen. Synthetische Bruchnetzwerke als Vertreter von Bruchflächen interpretierten die Clusterbildung und Größenverteilung von induzierten Ereignissen und klärten den Einfluss von mikroseismischen spezifischen Einflussfaktoren wie hypozentralen Standortunsicherheiten, Existenz einer fragmentierten Zone und wiederholten Ereignissen auf die beobachtete Seismizität auf. Die Ähnlichkeit zwischen den Skalierungseigenschaften von induzierter Seismizität und fraktalen Bruchnetzwerken führte zur Einführung eines statistischen Seismizitätsmodells, das die räumliche Clusterbildung und Größenverteilung potentieller Bruchflächen in Beziehung setzt. Dieses Modell könnte die maximale Magnitude induzierter seismischer Ereignisse vorhersagen, basierend auf der Skalierung früher Seismizitätsmuster in der hydraulischen Stimulation mit zunehmender Injektionszeit und stimuliertem Volumen.

Ausgehend von der Hypothese, dass Stressheterogenitäten durch natürliche Brüche und ihren geometrischen Eigenschaften stark kontrolliert werden, wurde eine neuartige stressbasierte Tomographie in einer Bayesischen Umgebung entwickelt. Diese Inversionstechnik ist in der Lage, das Bruchnetzwerk und seine Heterogenität in tiefen geothermischen Ressourcen zu charakterisieren. Diese Inversionstechnik verwendete lokale Variationen von in-situ-Hauptspannungskomponenten (mindestens eine Orientierung und eine Magnitude) entlang von Bohrlöchern und die vorherige Information über das Bruchnetzwerk. Die Markov-Sequenz verglich das simulierte Spannungsprofil mit den beobachteten Spannungsprofilen auf dem Bohrloch und akzeptierte mögliche Realisierungen unter Verwendung von Metropolis-Hastings (MH) Akzeptanzkriterien. Der Markov Chain Monte Carlo (MCMC) -Algorithmus speicherte eine große Anzahl von Realisierungen in einem Ensemble. Eine Auswahl akzeptierter Realisierungen visualisierte die möglichen Bruchstellen und entsprechenden Längen in einer

Bruchwahrscheinlichkeitskarte. Diese Technik wurde erfolgreich an einfachen synthetischen und komplexen Aufschluss-basierten Bruchnetzen getestet.

Die Spannungsheterogenitäten im Bohrlochmaßstab zeigen schließlich skaleninvariante Eigenschaften in verschiedenen Wellenlängen. Mit der gleichen Hypothese, dass die Stressheterogenitäten durch Gleiten auf natürliche Brüchen kontrolliert werden, wurden 2D-Bruchnetzwerke generiert, um die Skalierung von Stressheterogenitäten und wichtigen Netzwerkeigenschaften in Beziehung zu setzen. Die Analyse der synthetischen Daten zeigte eine schwache umgekehrte Korrelation zwischen dem Bruchlängenexponenten und der fraktalen Dimension der Stressheterogenitäten. Darüber hinaus beeinflusste die Bruchdichte die Spannungsprofile von Bohrlöchern stark.



# Contents

---

<b>1</b>	<b>Introduction .....</b>	<b>23</b>
1.1	General context .....	23
1.2	Reservoir engineering simulation.....	24
1.3	Characterization of geothermal reservoir .....	25
1.3.1	Fracture network .....	25
1.3.2	In-situ stress.....	25
1.3.3	Induced seismicity.....	26
1.4	Fractal geometry and power-law scaling .....	27
1.5	Open scientific questions .....	28
1.6	Thesis objectives .....	28
1.7	Thesis structure .....	30
<b>2</b>	<b>Fractal scaling of fracture patterns in deep boreholes and implications to constrain discrete fracture network models .....</b>	<b>31</b>
2.1	Introduction .....	34
2.2	Synthetic fracture network model .....	36
2.2.1	DFN generation methodology.....	37
2.2.2	2D fractal DFN generation.....	38
2.2.3	Effect of geometric boundaries on 2D fractal DFNs.....	43
2.2.4	3D DFN generation and verification.....	46
2.2.5	Stereological analysis .....	47
2.3	1D spatial distribution of fractures.....	50
2.3.1	Synthetic fractures.....	50
2.3.2	Natural fractures in deep boreholes.....	54

2.4	Minimum number of fractures required for a robust estimation of $D_{1D}$ .....	60
2.5	Fractal profile of spatial distribution versus depth.....	62
2.6	Discussion .....	63
2.7	Conclusions .....	67
<b>3</b>	<b>Maximum magnitude forecast in hydraulic stimulation based on clustering and size distribution of early microseismicity .....</b>	<b>69</b>
3.1	Introduction .....	71
3.2	Microseismicity in Basel geothermal site .....	73
3.2.1	Spatial distribution .....	73
3.2.2	Rupture radius distribution.....	73
3.3	Synthetic fracture network model .....	75
3.3.1	Uncertainty of hypocentral locations .....	76
3.3.2	Existence of a fractured zone .....	76
3.3.3	Repeating events .....	77
3.4	Geometrical forecast approach.....	78
3.4.1	Methodology .....	79
3.4.2	Time dependency of clustering and size distribution of seismicity in Basel .....	80
3.4.3	Application to Basel .....	81
3.5	Discussions and conclusion.....	82
<b>4</b>	<b>Fracture network characterization using stress-based tomography .....</b>	<b>85</b>
4.1	Introduction .....	87
4.2	In-situ stress characterization .....	90
4.3	Methodology .....	92
4.3.1	Forward simulation of stress variability in a fractured domain .....	92
4.3.2	Principles of Bayesian inversion.....	94
4.3.3	Inversion methodology.....	95

4.4	Test cases.....	98
4.4.1	Simple synthetic network.....	99
4.4.2	Outcrop-based network.....	99
4.5	Results.....	102
4.5.1	Simple synthetic case.....	103
4.5.2	Out-crop based case.....	105
4.6	Discussion and conclusions.....	107
<b>5</b>	<b>Preliminary analysis of the linkage between scaling of stress heterogeneities and fracture network.....</b>	<b>109</b>
5.1	Introduction.....	111
5.2	Power-law scaling.....	113
5.2.1	Fracture network.....	113
5.2.2	Stress heterogeneities.....	114
5.2.3	Microearthquakes.....	116
5.3	Methodology.....	116
5.3.1	Assumptions.....	117
5.3.2	DFN generation.....	117
5.3.3	Modeling of stress variability.....	118
5.3.4	Analyses of the generated stress field.....	118
5.4	Results of the parameter study.....	120
5.4.1	Relation between scaling of stress and fracture length exponent.....	120
5.4.2	Relation between scaling of stress and fracture intensity ( $P_{21}$ ).....	121
5.5	Discussion and conclusions.....	121
<b>6</b>	<b>Conclusions and outlook.....</b>	<b>125</b>
6.1	Conclusions.....	125
6.2	Outlook and perspective.....	128

<b>Bibliography .....</b>	<b>129</b>
<b>Appendix A .....</b>	<b>149</b>
<b>Appendix B .....</b>	<b>153</b>
<b>Appendix C .....</b>	<b>157</b>



# List of Figures

---

Figure 1-1. Schematic representation of PhD objectives. This PhD thesis aims to relate fracture network characteristics, stress heterogeneities and induced seismicity in the context of an interlinked, self-organized fractal system. .... 29

Figure 2-1. Illustration of the procedure for populating the probability distribution map generated using the Multiplicative Cascade process with fracture centers, and then assigning a power-law length distribution to the fractures that is consistent with equation 2.1. The vector  $U$  in the center is the fracture assignment vector. .... 42

Figure 2-2. (a) Realization of a fracture density distribution in a domain of 500 m for a fractal dimension of 1.5 and an  $l_{min}$  of 2 m (b) A DFN realization generated from (a) using a length exponent  $a = 2$ . The fracture density parameter,  $\alpha$ , was taken as 0.3 so as to give approximately 1677 fractures (c) Correlation function of fracture centers  $C(r)$  computed from the density distribution in (a), together with the local slope and the slope expected for  $D = 1.5$ . (d) Verification that the cumulative frequency distribution of length computed from (b) is linear with a slope equal to  $1-a$  on a log-log plot..... 43

Figure 2-3. (a) Realization of a random fractal DFN generated in a domain of length 100m (outlined in red) with exponents of  $a=1.5$  and  $D=1.5$ , and no geometric boundary imposed (i.e. some longer fractures extend outside the frame boundary at  $\pm 100$  m). (b) The same DFN generated in (a), but with all fractures that extend outside the domain removed. (c) The same DFN generated in (a), but with fractures that extend outside the domain truncated. (d) Realization of a random fractal DFN generated in a domain of length 100 m (outlined in red) with exponents of  $a=2.5$  and  $D=1.5$ , and no boundary imposed. (e) The same DFN generated in (d) but with all fractures that extend outside the domain removed. (f) The same DFN generated in (d), but with fractures that extend outside the domain truncated. .... 44

Figure 2-4. Effect on correlation functions and length distributions of applying different approaches to the problem of fractures that extend beyond the domain boundary, namely to remove the fractures (blue), or to trim them so they do not extend beyond the domain boundary (green). The curves obtained by including such fractures with their true length are shown for comparison (brown), (a) Correlation functions and their log-log slope, and (b) length distributions derived from the DFNs in Figure 2.3a and 2.3b which correspond to the case  $a = 1.5$ . The log-log slopes of the  $C(r)$  functions should be flat and equal to 1.5,

the correlation dimension of 1.5 shown by the black dashed line. (c) Correlation functions and their log-log slopes and (d) length distributions derived from the DFNs in Figure 2.3d and 2.3e which correspond to the case  $a = 2.5$ . ..... 46

Figure 2-5. (a) A synthetic 3D network generated in a 500 m domain using dual power-law model with  $D = 2.7$ ,  $a = 2.8$ ,  $l_{\min} = 10$  m and  $\alpha = 0.02$ . b) Correlation function and its local slope of the generated network. c) Complementary cumulative length distribution of the generated network ( $N$  is the number of fractures larger than size of  $R$ )..... 47

Figure 2-6. Stereology plot of 1D lines sampling a 2D fractal fracture network. (a) Values of  $D_{1D}$  obtained from DFN realizations with random fracture orientations generated with  $a = 1.5$  as a function of  $D_{2D}$ . For a given  $D_{2D}$  value, the red line in the box denotes the median value of  $D_{1D}$  taken over the realizations, and the lower and upper edges of the box denote the 25 and 75 percentile values respectively whose difference denotes the inter quartile range (IQR). The horizontal short black lines lie 1.5IQRs from the upper and lower edges of the 25 and 75 percentiles. Red crosses are realization falling outside this range. (b) Same as (a) but with  $a_{2D} = 2.5$  with random fracture orientations. (c) Same as (a) but with  $a_{2D} = 1.5$  and two perpendicular sets. (d) Same as (a) but with  $a_{2D} = 2.5$  and two orthogonal sets. .... 51

Figure 2-7. Stereology plot of 1D lines sampling a 3D fractal fracture network. (a) Values of  $D_{1D}$  obtained from DFN realizations with random fracture orientations generated with a length exponent  $a_{2D} = 1.5$  as a function of  $D_{3D}$  with random orientations. (b) Same as (a) but for a length exponent  $a_{2D} = 2.5$  with random orientations. .... 52

Figure 2-8. (a) A schematic view of a synthetic fracture pattern on a 1D scanline, generated using 1D multiplicative cascade process with a  $D_{1D} = 0.75$ ,  $L = 512$  m and  $n = 16$ . For the sake of visibility, only 64 m of the entire domain is plotted. The number of fractures in the entire domain is 1,000. (b) Two-point correlation function and its local slope of the synthetic 1D scanline generated in a. (c) Box-counting analysis and its corresponding local slope of the synthetic 1D scanline generated in a. (d) Complementary cumulative distribution of spacing and its local slope of the synthetic 1D scanline generated in (a). 54

Figure 2-9. Application of three different techniques to compute the fractal dimension of fracture patterns in Basel-1 borehole, a) two-point correlation function, b) box-counting technique and c) statistical distribution of spacing. .... 56

Figure 2-10. Correlation and log-log slope functions of fracture sets in the Basel-1 well. The best-fit horizontal line to the log-log slope function over the  $r$  range of 2-200 m which gives the value of  $D_{1D}$  is shown together with the standard deviation. The range of  $r$  over

which fractal scaling is seen is indicated between the vertical lines drawn at the 1 sigma variation of $D_{ID}$ . (a) set 1, (b) set 2, (c) set 3, (d) set 4. ....	57
Figure 2-11. Same as Figure 2.10 but for the four fracture sets identified in the GPK3 well at the Soultz geothermal site: (a) set 1, (b) set 2, (c) set 3, (d) set 4. ....	58
Figure 2-12. Same as Figure 2.10 but for the four fracture sets identified in the GPK4 well at the Soultz geothermal site: (a) set 1, (b) set 2, (c) set 3, (d) set 4. ....	59
Figure 2-13. Correlation and log-log slope functions derived from all fractures (grouped into one dataset regardless of their orientation) intersecting (a) the Basel-1 well, (b) the GPK3 well (c) the GPK4 well. ....	60
Figure 2-14. (a) Scatter plot of $D_{ID}$ values obtained by stepping (variable-length) windows that contain a given numbers of fractures with an offset of 10 fracture along a scanline at $X = -178$ . The given number of fractures ranged from 5 to the total fracture number in steps of 1. The red lines denote the median and upper and lower quartiles of the statistical distribution of $D_{ID}$ values obtained for each fracture number. (b) Standard deviation of the local slope over the fractal range associated with the estimation of the $D_{ID}$ values for variable number of fracture included in the sample. ....	62
Figure 2-15. (a) Profile of the density of fractures in the Basel-1 well per 10m interval. (b) Variation of correlation dimension in moving windows containing 300 fractures with 200 overlaps in Basel-1. The error bars represent the standard deviation of the local slope within the fractal range. ....	64
Figure 2-16. (a) Profile of the density of fracture in the GPK3 well per 10m interval. (b) Variation of correlation dimension in moving windows containing 500 fractures with 400 overlaps in GPK3. (c) Profile of the density of fractures in the GPK4 well per 10m interval. (d) Variation of correlation dimension in moving windows containing 500 fractures with 400 overlaps in GPK4. The error bars represent the standard deviation of the local slope within the fractal range. ....	65
Figure 3-1. (a) Top and side view of the spatial scattering of microearthquake hypocenters relative to the casing shoe in Basel geothermal system (Kraft and Deichmann 2014). (b) Frequency size distribution of microearthquakes and estimates of b-value using maximum likelihood estimates. (c) Correlation function and its local slope. (d) Complementary cumulative rupture radius distribution ( $R$ ) for different stress drops. ....	74
Figure 3-2. (a) A 3D random DFN with $D = 2.7$ , $a = 3.5$ and $\alpha = 0.1$ . (b) Effect of 93 m uncertainty in fracture center locations on the resulting spatial distribution of a random realization of the initial network. (c) 3D view of a 40 m width fractured zone. (d) Spatial	

organization of a fractured zone. (e) Spatial organization of the network merging two networks in a and c. (f) Effect of 100 repeaters in a maximum 5 m distance from 10 randomly selected fractures (10 repeaters belong to each fracture)..... 78

Figure 3-3. (a) Dependence of rupture radius exponent on the number of events in Basel geothermal site. (b) Dependence of rupture clustering on the number events in Basel. (c) Calibration of the seismicity model to the first 100 events (learning phase) during the injection phase and simulation of rupture radius distribution with increasing the encompassing volume in Basel geothermal reservoir. (d) Prediction of maximum moment magnitude  $M_w$  of Basel geothermal reservoir as a function of encompassing volume with an assumption of  $\Delta\sigma = 10$  MPa. .... 81

Figure 4-1. (a) A typical image log of GPK4 borehole drilled into Soultz-sous-Forêts EGS including the natural fractures and stress induced fractures (ADITFs and EDITFs). (b) and (c) depict an example of reflectivity and borehole radius from Basel-1 well, including borehole breakouts along with a natural fracture (Valley et al. 2014). .... 91

Figure 4-2. (a) Estimates of principal stress magnitudes in Basel EGS (Valley and Evans 2015b). (b) Orientation of minimum principal horizontal stress inferred from borehole breakouts in the borehole drilled into Basel EGS (Valley and Evans 2009). .... 92

Figure 4-3. Overview of the MCMC algorithm:  $\theta$  denotes the model vector,  $\theta_i$  is the last accepted model,  $\theta'$  is the proposed model,  $\xi$  is the observation vector (the stress measurements),  $f(\theta)$  is the forward model,  $\alpha$  is the Metropolis-Hastings acceptance criteria, and  $L$  is the likelihood function. The initially generated DFN goes into the loop, and the DFN is updated by the movement of a randomly selected fracture. Each realization is evaluated using Metropolis-Hastings criteria (SIM is the simulated stress perturbation; EXP is the observed or expected stress perturbation), and any accepted realization is stored in the ensemble. The ensemble is finally converted to a probability map using the methodology described in Chapter 5.1..... 98

Figure 4-4. Forward simulation of stress variability within the simple synthetic network given the geometrical characteristics listed in Table 2, and using input parameters for the geomechanical model from Table 1. Figure (a) depicts the  $\sigma_1$ -field and (b) the  $\beta$ -field. Stress magnitude and orientation profiles representing the stress fluctuations along the borehole ( $X = 0$ ) are shown in (c) and (d). .... 100

Figure 4-5. (a) Surface geological model of the Tschingelmad outcrop in Alps. (b) Fracture network mapped from the geological model. The fractures larger than the pre-defined cut-off (8 m) are mapped. (c) Histogram of fracture length distribution. .... 101

Figure 4-6. Forward simulation of stress variability within the outcrop-based fracture network with the characteristics listed in Table 2 and input parameters of the geomechanical model from Table 1, a) $\sigma_1$ field and b) $\beta$ field. Profiles representing the variability are depicted in c) $\sigma_1$ , and d) $\beta$ at $X = 0$ .....	102
Figure 4-7. (a) Misfit evolution of all accepted realizations during the MCMC sampling. The converged range is chosen to be between the 175th and 350th iteration. (b) The initial simple synthetic network; (c) The fracture probability map of the 50 best fit realizations in the ensemble.....	104
Figure 4-8. (a) Profiles of stress magnitude $\sigma_1$ and (b) orientation $\beta$ at the borehole for the simple synthetic case (Figure 4-4c, 4-4d) compared to profiles at the same location of a randomly chosen DFN from the selected range in Figure 4-7b.....	105
Figure 4-9. (a) MCMC convergence trend of accepted realizations for the outcrop-based fracture network; (b) original “true” network compared to (c) the corresponding fracture probability map obtained by inversion.....	106
Figure 4-10. Stress profiles of initial outcrop-based model compared to those a randomly sampled DFN of the final ensemble: (a) variation of $\beta$ , (b) a variation of $\sigma_1$ . The black circle indicate the part of the stress profile highly affected by a fracture tip and which is not well reproduced.....	107
Figure 5-1. (a) Orientation of maximum principal horizontal stress $S_{hmax}$ derived from borehole breakouts and axial drilling induced tension fractures observed in Basel-1 well. The orientation of each breakout leg is averaged for each sampling point (every 40 cm) and then subtracted from the average orientation along the borehole. The logged interval is between 2600-5000 m. (b) PSD function using FFT with a pre-filtering with Hanning window derived for the data provided in a. This figure defines a slope of -1.5 between 1 and 0.01 cycle/m (wavelengths of 1 and 100 m) implying a fractal dimension $D = 1.75$ . .....	115
Figure 5-2. (a) Stress field as a result of applying far-field stresses and slip on fracture surfaces in the depicted fracture network with length exponent of $a=3$ . (b) Stress orientation heterogeneity $\theta$ , on the borehole located at $X = 0$ , deviation from the average. (c) Power Spectral Density (PSD) plot of the stress profile in (b) using the FFT with pre-filtering of data using Hanning window.....	120
Figure 5-3. (a) Box-plot of $D$ values of stress perturbations for each length exponent containing 100 realizations with the same fracture intensity $P_{21}$ of $0.02 \text{ m}^{-1}$ . DFN realizations are generated using the methodology described in section 5.3.2 with the simulation parameters	

listed in Table 5-1. (b) Box-plot of  $D$  values of stress perturbations for each fracture intensity  $P_{21}$  containing 100 realizations with the same length exponent  $a$  of 3..... 121

# List of Tables

---

Table 2-1. Number of fractures in sets and corresponding mean orientations in Basel-1(Ziegler et al., 2015)..... 55

Table 2-2. Number of fractures in recognized sets and corresponding mean orientations in boreholes GPK3 and GPK4 at the Soultz-sous-Forêts site ..... 55

Table 2-3. 1D Fractal dimension of fracture patterns in three deep boreholes and the corresponding range. Correlation dimension obtained from the analyses of fracture intersection spacing in the three wells..... 57

Table 4-1. List of input parameters for geomechanical modeling of fractured rocks using DDM simulator..... 94

Table 4-2. Geometrical characteristics of test cases ..... 99

Table 5-1. Input parameters for modeling the stress variability using DDM approach. Tension positive convention is used for the stress magnitudes..... 119





Dedicated with big thanks to my wonderful wife '*Sevin*' for her love, patience, support and encouragement.



# Acknowledgements

---

The research leading to these results has partially received funding from the European Community's Seventh Framework Program under grant agreement No. 608553 (Project IMAGE). The rest of funding has been provided by chair of Engineering Geology at earth sciences department of ETH Zürich.

Apart from the financial support, this interdisciplinary research project benefited the support, supervision and collaboration of a large number of experts. First of all, I would like to greatly thank Prof. Dr. Benoît Valley, who was my direct supervisor. He has provided a very high quality, precise and kind supervision since the start of this PhD project. In addition, I am thankful to Dr. Keith Evans who initiated this research and provided critical and careful supervision on some parts of this thesis. I also warmly thank Prof. Dr. Simon Löw for giving me this opportunity to work in his group and provided me outstanding support and also continuous supervision throughout my doctoral studies. I would like to deeply appreciate Prof. Dr. Olivier Bour (University of Rennes) for bringing his expertise to the examination committee and fruitful discussions at the early stages of this research. I am also grateful to Prof. Dr. Stefan Wiemer, Dr. Thessa Tormann, Dr Mohammadreza Jalali, Dr. Mark Somogyvari and Prof. Dr. Peter Bayer for bringing their innovation with an active involvement in different aspects of this research.

I would like to acknowledge Prof. Dr. Philippe Davy (University of Rennes), Dr. Caroline Darcel (Itasca), Dr. Chrystel Dezayes (BRGM), Dr. Omid Moradian and Dr. Martin Ziegler for many constructive discussions. Furthermore, I would like thank Hannes Krietsch for the German abstract. I would like to express my gratitude to Bernadette Würstch and Andrea Gossweiler for the administrative support. I would like to thank my colleagues Jaime, Carlos, Nicolas and Ali (my officemates), Bernard, Beneditta, Linwei, Molly, Nikhil, Sophie, Franzi, Larissa, Kerry, Andrea, Maria, Clement, Tobias, Marc, Jordan, Ying and Santos who provided a very friendly and pleasant working environment.

I am also in a great debt to my parents and my family who supported me continuously from the first day of my school until completion of my PhD. In addition, I would like to thank my parents-in-law for their great support.



# 1 Introduction

---

## 1.1 General context

The global tendency to produce CO<sub>2</sub> emission-free energy, public aversion toward nuclear plants and irreversible influence of fossil fuels on human beings and global ecosystem has raised the interest to develop renewable energies (Intergovernmental Panel on Climate Change, IPCC, 2014). In particular, Switzerland has changed its energy policy to phase out the nuclear power plants until 2050 and replace the gap in energy supply with renewable resources. In this context, geothermal energy acts as a potential CO<sub>2</sub>-free energy resource to provide heat or generate electricity. Earth's crust hosts a vast amount of energy in the form of heat that can substantially contribute to energy supply (Bertani 2012; Hirschberg et al. 2014; Tester et al. 2006). In this regard, Swiss Federal Office of Energy (SFOE) has estimated a contribution of about 6-8 percent of annual electricity generation, which may be achieved by geothermal energy systems by 2050 (Hirschberg et al. 2014).

Conventional geothermal (hydrothermal) systems, are t are found where sufficiently high temperatures and hydraulic conductivity is present in water bearing formations or structures. Thus, they are limited to specific geological contexts. When the hydrothermal resource is not present, circulation of fluids (e.g. water) between injection and production wells cannot be achieved economically unless engineering techniques are deployed to increase the rock mass permeability to facilitate the heat exchange with hot rock and to extract the heat stored in the solid rock mass (Hirschberg et al. 2014). These systems are referred as Engineered or Enhanced Geothermal Systems (EGS). However, currently, only a limited number of geothermal power plants are operating in favorable geological conditions with economical flow rates and sufficient heat exchange.

Desirable temperatures (ideally higher than 120°C) for EGS developments in regions with standard geothermal gradient (i.e. 30 °C/km), are typically located between 4-6 km depth. The corresponding host rocks are mostly low-porosity and low-permeability crystalline basements, in which the fluid flow is mainly occurred through the fractures and faults (Davatzes and Hickman 2010; Dezayes et al. 2010; Genter et al. 2010). However, reservoir creation (i.e. engineering of an artificial reservoir with sufficient permeability) is one of the main challenges in developing geothermal energy. The development of the reservoir can be achieved by various

stimulation techniques, namely hydraulic stimulation, thermal stimulation and chemical stimulation. Hydraulic stimulation consists of massive fluid injection at high rate and pressure. The processes involved in permeability creation are complex and not fully understood, but they certainly involve hydro-mechanical coupled response of existing fracture and faults (Evans 2005). Fluid pressure increase may lead to generation of new fractures or failure on pre-existing fractures/faults, because in most cases the in-situ stress state is such that a significant amount of shear stress is resolved on the optimally oriented fractures/structure. Hydraulic shearing may result in permeability enhancement for 2-3 orders of magnitude, which is particularly attractive for EGS developments (Evans et al. 2005a; Häring et al. 2008). When only a small amount of overpressure is required to fail existing fractures, the situation is referred as critically stressed. There is evidences showing that critically stressed conditions are the rule, not the exception (Townend and Zoback 2000).

Failure of fractures in shear is likely a requirement for an efficient and permanent permeability creation, however typically part of stress relief associated with slip is emitted as seismic energy, referred as induced seismicity. The induced seismicity may be relatively large to be felt by public and cause the suspension of geothermal development projects, such as Basel and St. Gallen projects in Switzerland (Edwards et al. 2015; Häring et al. 2008). Hence, the main challenge in EGS developments is optimizing the circulation parameters to create (enhance) permeability without inducing excessive seismicity that may result in damaging events.

## **1.2 Reservoir engineering simulation**

A prerequisite to handle the challenges of EGS technology is to be able to design reservoir engineering operations (e.g. hydraulic stimulation) in a way that the behavior of the reservoir in terms of permeability increase and seismic response can be anticipated. This requires design tools, typically numerical reservoir simulators that include the relevant physical processes involved in hydraulic stimulation. Thus, thermo-hydromechanically coupled numerical tools are being developed to model different aspects of reservoir behavior and evaluate stimulation strategies (e.g. Baisch et al. 2006; Rutqvist and Oldenburg 2008). In order to produce meaningful results, these models must be parametrized with appropriate initial and boundary conditions. This requires a geological model for the reservoir that includes quantitative information on the reservoir key characteristics such as natural fracture network and the in-situ stress state within the target rock mass. The characterization of the target rock mass is thus an important task to perform in order to produce robust design for geothermal reservoir engineering.

### **1.3 Characterization of geothermal reservoir**

A geological model should represent the whole reservoir with a realistic distribution of relevant geological features such as fractures and faults from small to large scales. Moreover, information on in-situ stress state in reservoir is also necessary to include mechanical aspects of the target reservoir to quantitatively assess the induced seismicity hazard and risk (Amann et al. 2017).

#### **1.3.1 Fracture network**

The characterization of fracture network in deep geothermal reservoirs is challenging because typically the host rock is not outcropping. Geophysical techniques from surface are limited in resolution when dealing with great depth and reflection seismic technology is difficult to interpret in crystalline basement rocks, because potential reflectors are inherently not well defined. More detailed information can be acquired when a deep well is drilled through the target rock mass with well logging techniques. The initial source of information about the natural fractures within EGS reservoirs stems from borehole images (e.g. acoustic televiewer logs). These logs permit to identify the position and orientation of fractures along the borehole. Valley and Evans (2015a) provide a summary of the state-of-the-art in reservoir characterization from borehole measurements and identify gaps and research needs.

However, fracture network characterization is challenging at early project stages, especially when data from only a single exploration well penetrating the target reservoir may be available. Fracture network attributes such as length, aperture and spatial distribution control the hydromechanical behavior of fractured rocks. In particular, the fracture length distribution is a key parameter for assessing the connectivity of the fracture network and cannot be constrained with a single wellbore data.

#### **1.3.2 In-situ stress**

Information on the in-situ stress state is fundamental to any seismo-thermo-hydro-mechanical characterization of fractured reservoirs (Amann et al. 2017; Ghassemi 2012; Preisig et al. 2015; Zoback 2010). In-situ stress state characterization is also challenging because no technique exists that can reliably to estimate all stress components in a deep borehole. The knowledge on one hand of the fracture orientations within the reservoir and on the other hand on all the components of the in-situ stress tensor is essential to assess fracture stability and response to hydraulic injection.

In addition, there are evidences that stress is typically highly variable within the reservoir space (these variations are often referred as stress heterogeneities), although the control on this variability is not well understood. One potential explanation is that in-situ stress heterogeneities are largely affected by slip on natural fractures and faults (e.g. Barton and Zoback 1994; McNamara et al. 2015; Pierdominici et al. 2011; Rajabi et al. 2017; Sahara et al. 2014; Valley 2007; Yale 2003). An alternate explanation for stress heterogeneities have been proposed with the potential link with elastic properties variability in the rock mass (e.g. Langenbruch and Shapiro 2014). However, the relation between the in-situ stress heterogeneities and characteristics of natural fractures is not fully understood (Rutqvist 2015; Tsang et al. 2018; Valley et al. 2014).

### **1.3.3 Induced seismicity**

The interaction between the fracture network and fluid pressure induced changes results in induced seismicity (Evans et al. 2005b). The observed dominant double-couple mechanism of induced seismicity suggest that the seismic source is located on planar structures, i.e. fractures and faults, and thus induced seismicity characteristic is likely to carry some information on fractures and fault properties. The combination of focal solutions allow also to put some constraints on the in-situ stress (e.g. Dorbath et al. 2010). Thus, induced seismicity patterns also provide valuable information on some aspects of fracture network that may be applied to generate stochastic realizations of fracture network models known as discrete fracture networks (DFN).

One major challenge in induced seismicity is to develop seismic hazard assessment tools including statistical, physics-based and hybrid forecasting approaches that predict the induced seismicity during hydraulic stimulation (Gaucher et al. 2015). Statistical approaches apply the observed seismicity patterns for real-time hazard assessment, such as traffic light system (Bommer et al. 2006). Physics-based approaches simulate the physical processes (i.e. thermo-hydrromechanical effects) during the hydraulic stimulation based on the reservoir characteristics (e.g. Baisch et al. 2006; McClure and Horne 2011; Rutqvist and Oldenburg 2008). The hybrid approaches use the physics-based reservoir description constrained with the observed seismicity patterns (e.g. Gischig and Wiemer 2013; Goertz-Allmann and Wiemer 2012; Shapiro et al. 2013). However, different approaches have their inherent advantages and drawbacks that are comprehensively discussed by Gaucher et al. (2015).



## 1.4 Fractal geometry and power-law scaling

A common characteristic of the data sets discussed in this section – i.e. fracture network, stress variability at borehole scale, elastic properties and induced seismicity – is that the statistics of their parameters (e.g. magnitude, spacing, length,...) present scale invariant or more generally fractal characteristics. Scaling relationships of seismicity is known since the precursory work of Gutenberg and Richter (1954). Many studies have shown scale invariance in various properties of natural fracture networks (e.g. Bonnet et al. 2001; Kim and Sanderson 2005). Interpretation of sonic logs showed the fractal nature of elastic properties of rock masses (e.g. Goff and Holliger 1999). Analyses of borehole failure show that some components of the in-situ stress follow fractal laws (Day-Lewis et al. 2010; Valley and Evans 2014a; Valley and Evans 2010).

The origin of the prevalence of fractal characteristics in nature isn't entirely clear, although the dominant hypothesis is that this is a facet of the behavior of complex self-organized critical dynamics (Allegre et al. 1982; Bak et al. 1988; Sornette 2006; Sornette et al. 1990). In other terms, this means that the evolution of damage in a rock mass due to long-term deformation imposed by the tectonic forces leads to the observed fractal characteristics. Davy et al. (2010) and Spyropoulos et al. (2002) have shown that the stress interactions between fractures in a growing fracture population can lead to power-law distributions. Fracture attributes such as length distribution is expected to control the seismogenic parameters such as b-value that relates the earthquake frequency and magnitude (Day-Lewis et al. 2010). In-situ stress displays local fluctuations on borehole scales (e.g. Schoenball and Davatzes 2017; Shamir and Zoback 1992; Valley and Evans 2007b) that are also suggested to control the scaling of earthquake magnitude frequency of induced events (Day-Lewis et al. 2010).

All these evidences suggest that these reservoir characteristics are intimately related because they result from the evolution of a common system driven by the same tectonic external forcing. This suggest then that for the very practical task of determining reservoir characteristics, additional value can be gained by treating all the parameters together instead of try to quantify them in isolation. However, this requires that the details of these relationships among the fracture network, stress heterogeneities an induced seismicity is better understood. Under these conditions, improved reservoir models could be developed that may be used to better forecast the reservoir response to stimulation operations and to develop real-time monitoring and seismic risk assessments of hydraulic stimulation.

## **1.5 Open scientific questions**

There has been a large amount of research on understanding the hydraulic stimulation experiments from laboratory scale to large-scale. However, there are many open questions regarding the processes involved in permeability creation and associated seismicity. For a detailed review on the current state-of-the-art in the seismo-hydromechanical response of deep geothermal reservoirs to hydraulic stimulations and current open research questions, refer to Amann et al. (2017). However, specific research questions (RQ) related to this PhD thesis are listed as following:

RQ1) Is the spatial distribution of fracture patterns in deep boreholes following fractal statistics? If yes, is it possible to constrain the 3D spatial distribution of fracture network from 1D borehole data?

RQ2) Is there any similarities between the scaling characteristics of induced seismicity patterns and fracture network?

RQ4) Is there any methodology to constrain the fracture network geometry from stress perturbations at deep boreholes?

RQ3) How are the key fracture network attributes related to the stress variability at borehole scale?

## **1.6 Thesis objectives**

The starting hypothesis of the thesis is that key characteristic of the reservoir, namely the properties of the fracture network, the variability of stress within the rock mass and the seismogenic characteristics of the reservoir are strongly interrelated because they are part of the same self-organized fractal system that evolves under long-term tectonic forcing (Figure 1-1). A set of processes activated during this evolution that include fracture nucleation and growth, fracture instability, stress drop and stress transfer condition the characteristics of the rock mass. Contrary to many studies that have been analyzing fracture network, stress characterization or microseismic analyses independently, this starting hypothesis strongly condition the approach adopted in this thesis, i.e. the characteristics of the reservoir are interrelated and must be studied together. In this context, the primary objective of this PhD thesis is to study the exact nature of the relations among fracture network, stress heterogeneities and induced seismicity in deep geothermal reservoirs. In the development of the work, some specific aspects had to be clarified and studied in details and this conditions the following themes that are developed in the thesis:

1. Characterization of natural fracture patterns in deep crystalline basement rocks with particular emphasis on the scaling of spatial distributions. This is achieved by analyzing the fractures obtained from borehole image logs from Basel and Soultz-sous-Foret and Basel geothermal sites. In addition, the aim is to constrain the spatial distribution of fractures in space using borehole data (response to RQ1).
2. Relating the scaling of fracture network and induced seismicity. Here, the objective is to characterize the spatial patterns of induced microseismicity in the Basel geothermal site and relate them to the scaling of fracture patterns. The purpose is to propose a statistical model that includes the rupture size and spatial clustering of induced events using scaling laws. This model should forecast the maximum magnitude using scaling properties of early time stimulation seismicity patterns (response to RQ2).

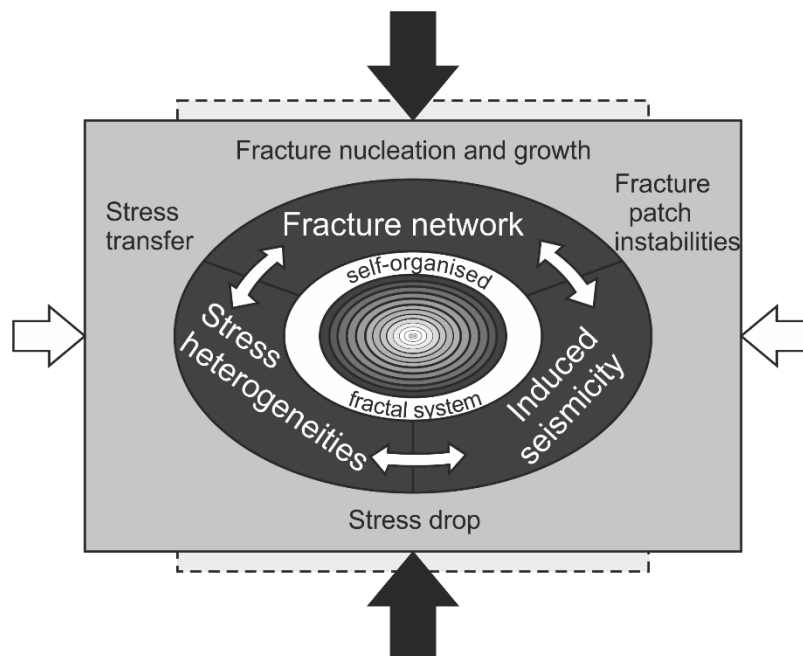


Figure 1-1. Schematic representation of PhD objectives. This PhD thesis aims to relate fracture network characteristics, stress heterogeneities and induced seismicity in the context of an interlinked, self-organized fractal system.

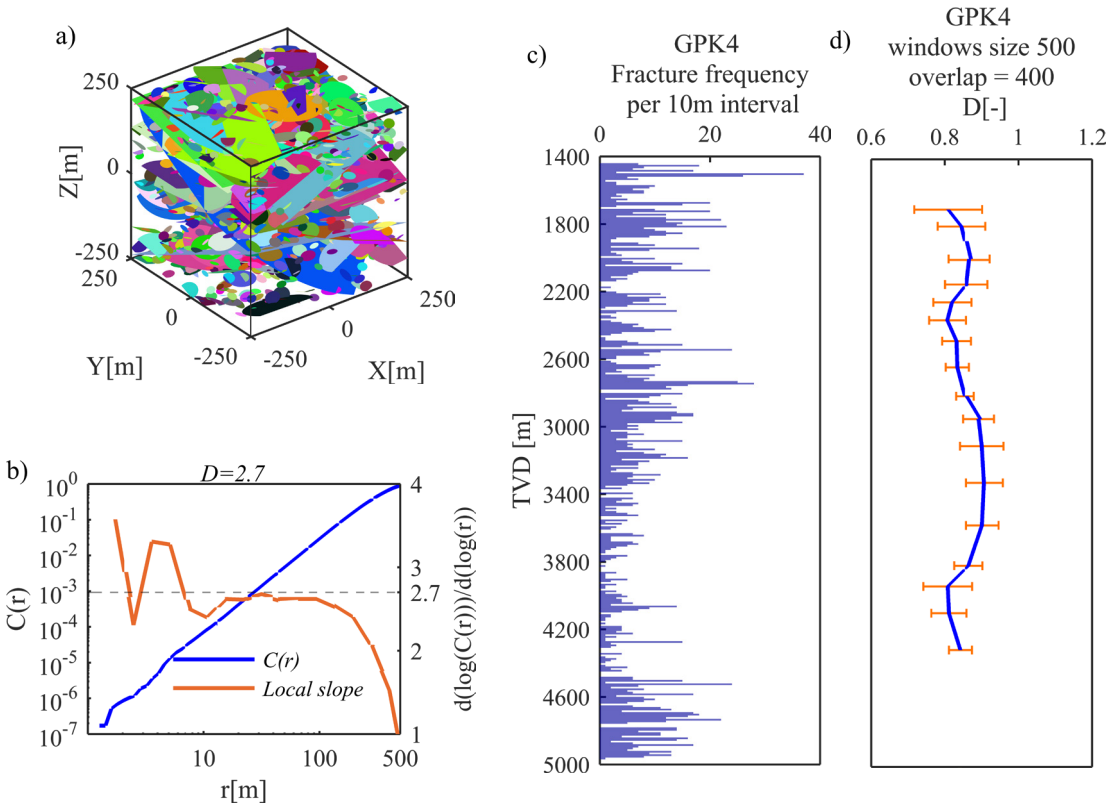
3. Constrain the fracture network characteristics using the in-situ stress heterogeneities at boreholes. The main objective is to develop an inversion framework that can reconstruct the fracture network geometry. A novel concept of stress-based tomography Bayesian framework is expected to characterize the fracture network and its heterogeneity in deep geothermal resources (response to RQ3).

4. Relate the scaling of borehole scale in-situ stress fluctuations to the fracture network characteristics. The objective is to relate the scaling exponents of fracture network attributes such as length and spatial distribution to the scaling of stress heterogeneities at boreholes (response to RQ4).

## **1.7 Thesis structure**

The thesis is structured around the four main objectives of this thesis. Chapters 2-5 are dedicated to these objectives, respectively. They are written in the form of paper manuscripts. These chapters are submission versions of four journal publications. With this paper compilation format, each chapter include its own introduction and literature review. This is why the current introduction is limited to some key messages that motivates the work while detailed reviews are not repeated here but included in each chapters. In addition, further details on these chapters that are not intended for publication are presented in the appendices. Appendices 1-2 provide additional information on chapters 2 and 3. Chapter 6 present a synthesis of the main achievement of the thesis and an outlook.

# 2 Fractal scaling of fracture patterns in deep boreholes and implications to constrain discrete fracture network models



Reproduced from: Afshari Moein, M.J., Valley B., Evans K.F., *Fractal scaling of fracture patterns in deep boreholes and implications to constrain discrete fracture network models*, Rock Mechanics and Rock Engineering Journal (Under review).



## **Abstract**

We present a methodology for generating fractal fracture networks in 1D, 2D and 3D that respect the dual power law model in which the scaling characteristics are set by the two independent parameters of the correlation dimension that pertains to separation of fracture centers, and the length exponent, that governs the distribution of fracture lengths. Synthetic fracture distributions were generated to evaluate the stereological relationships between the scaling parameters of 2D and 3D networks, and the scaling of fracture intersection points along a scanline through the network. The results showed that it is not possible to estimate the 2D and 3D fractal scaling parameters of correlation dimension or length exponent from the 1D correlation dimension of fracturing spacing from scanlines through the network, even if the length exponent is known a-priori. Synthetic 1D distributions of fracture spacing of known correlation dimension were used as a benchmark to test the consistency of estimates of fractal dimension derived from box-counting, two-point correlation, and power law fitting. The results showed that correlation dimension obtained from the two-point correlation method provided the most stable and reliable estimate of the fractal dimension of fractures on 1D scanlines or boreholes. Application of the two-point correlation function to the observed fracture distributions along three deep boreholes in crystalline rock at Basel and Soultz-sous-Forêts showed the distribution was fractal over more than two orders of magnitude in scale, and in all cases the fractal dimensions lay in the range 0.86-0.88. Similar results were obtained for fracture sets of common orientation within the wells, although the fractal dimension ranged between 0.65-0.75.

## 2.1 Introduction

Enhanced Geothermal Systems (EGS) aim to extract the heat from the earth by circulating fluids (e.g. water) between injection and production wells drilled to sufficient depth to reach temperatures higher than 150°C. Outside of areas of recent volcanism, the target reservoirs tend to be found in low-porosity basement rocks, where natural flow occurs primarily through the fracture network (Genter et al. 2010). The natural fracture transmissivity is typically not sufficient for economical flow rates. In order to increase the flow rates, massive fluid injections into the reservoir are performed in order to increase the permeability of the fractured media, a process referred to as hydraulic stimulation. The mechanisms underlying the process are complex and not fully understood. However, massive fluid injection changes the effective stress conditions by increasing the pore pressure within rough-walled fractures, thereby promoting shear failure and attendant dilation, which serves to increase fracture permeability (Evans 2005; Evans et al. 2005). The elevated pore pressure can also generate new fractures. Hydraulic shearing/fracturing is commonly accompanied by microseismic emission that might be relatively large. The public fear of earthquakes has led to project curtailment in some case like in Basel and St. Gallen geothermal projects in Switzerland. Thus, the major challenge in developing geothermal resources is to enhance the permeability of the target reservoir adequately through hydraulic stimulation without inducing damaging seismicity.

In order to design and assess EGS development strategies, a geological model of the target rock mass is required. This geological model should be representative of the whole reservoir with a realistic distribution of relevant geological attributes such as the fracture network geometry from small to large scales. The characterization of the fracture network is especially challenging at early project stages, when data from only a single exploration well penetrating the target reservoir may be available. In particular, the fracture length distribution, which is a key parameter for assessing the connectivity of the fracture network, cannot be constrained with a single wellbore data.

Fracture network characteristics have been studied from outcrops and multi-well study sites where a more complete characterization of the fractures is possible (Cowie et al. 1996). In such situations, it has been observed that several attributes of fracture networks exhibit power-law patterns referred to as fractal organization (Barton 1995; Bonnet et al. 2001; Bour et al. 2002; Davy et al. 1990a; de Dreuzy et al. 2001; de Dreuzy et al. 2002; Lei et al. 2015; Odling et al. 1999). Specifically, power-law scaling has been applied to characterize spatial distribution, trace length, spacing, RQD (Rock Quality Designation, Deere and Deere (1988)), aperture,



surface roughness etc. (Barton and Zoback 1992; Boadu and Long 1994; Bonnet et al. 2001; Power and Tullis 1991). The origin of the prevalence of power-law scaling in nature isn't entirely clear, although several researchers have proposed the implied statistical scaling is a facet of the behavior of complex self-organized critical dynamics (Allegre et al. 1982; Bak et al. 1988; Sornette 2006; Sornette et al. 1990). Davy et al. (2010) and Spyropoulos et al. (2002) have shown that the stress interactions between fractures in a growing fracture population can lead to power-law distributions. This suggests that some relations exist between the characteristics of the fracture network and the stress variability within this fractured rock mass. Particularly when a single fracture is present, the size of the stress perturbation scales linearly to the size of the fracture inducing the perturbation (Eshelby 1957; Pollard and Segall 1987). In a fracture network, such relation becomes non-trivial (Valley et al. 2014). Nevertheless, stress fluctuations are also found to follow power-law scaling, as shown by the study of nearly continuous profiles of borehole failure (Day-Lewis 2007; Valley and Evans 2014). The relation between the power-law scaling of fracture networks and stress fluctuations are not well understood, which is one of the motivations of the current research. Clarification of the potential relation could have important practical implications such as allowing constraints to be placed on attributes of the fracture network like fracture length distribution that are hard to quantify otherwise by observation of stress fluctuations from borehole failure. Further applications could also be envisaged if a clear link could be established between power-law scaling of fracture attributes and the seismogenic parameter of b-value that relates the earthquake frequency and magnitude. Intuitively, one can hypothesize that the magnitude distribution of microearthquakes is partly controlled by the fracture size distribution and the stress state in the reservoir. If the details of these relationships were better understood, it could be possible to use observation at the borehole wall (location and orientation of natural fractures and stress-induced failure) to better anticipate reservoir response to stimulation operations. Thus, the ultimate objective is to relate scaling laws of key reservoir characteristics such as fracture network to stress fluctuations and microseismic magnitude distribution. A necessary step to establish the potential relationships, is to fully understand the characteristics and limitations of the scaling laws in each discipline.

In this paper, we use synthetic fracture networks to explore the limitations of fracture network sampling and power-law scaling of borehole data. We explore the possible extrapolation of 1D fracture patterns intersecting the borehole to a 3D structural model. Then, we outline the scaling characteristics of natural fractures derived from borehole images of two geothermal reservoirs

of Basel and Soultz-sous-Forêts and extract the potential trends of scaling exponent along deep boreholes.

## 2.2 Synthetic fracture network model

In order to analyze the limitations of line sampling and power-law scaling of borehole data and possible extrapolation to a 3D geological model, a discrete fracture network model with valid stereological relationships is required. Discrete fracture networks (DFN) are geometrical representations of fracture attributes derived using stochastic methods and computational tools. The only DFN model we are aware of that respects stereological relationships is a dual-power-law model proposed by Davy et al. (1990b) that is based upon equation 2.1. Here, we begin by presenting a step-by-step methodology for generating a DFN that respects this equation. The DFN model is generated from the following equation that links the fractal spatial patterns of fractures to power-law distributions of fracture length and fracture centers given by:

$$n(l, L). dl = \alpha. L^D l^{-a}. dl, \quad l \in [l_{min}, l_{max}] \quad (2.1)$$

Here,  $n(l, L)dl$  is the number of fractures whose length is in the range  $[l, l + dl]$  and whose center belongs to a cubic volume in three dimensions of side length  $L$ ,  $\alpha$  is a normalization constant related to the fracture intensity,  $D$  is the correlation dimension of fracture centers, and  $a$  is the length exponent. Many researchers have applied this model to study hydraulics and mechanics of fractal DFNs (Darcel et al. 2003c; Harthong et al. 2012; Kim 2007; Verscheure et al. 2012). As an example, when  $a = D + 1$ , the DFN generated is self-similar and the connectivity of the network is scale invariant (Darcel et al. 2003c). Bour et al. (2002) applied this statistical model to evaluate scaling inherent in the fracture network geometry of multiscale fracture maps taken from outcrops in Hornelen basin (Norway). The dual power-law model contains no direct relationship between first-order descriptors, such as  $D$  and  $a$  and hence it is referred to as a first-order model. (Bour and Davy 1999) present a second order relation in which the exponents,  $D$  and  $a$  are related by  $x = \frac{a-1}{D}$ , where  $x$  is the exponent of a power-law including the average distance  $d$  from a fracture to the closest fractures having a larger length (i.e.  $d(l) \sim l^x$ ). Darcel et al. (2003a) introduced another scaling law for the Hornelen basin dataset that relates the mean distance from a fracture center to its nearest neighbor to its length. They related this scaling law to the stress shadow which is present around large fractures. Davy et al. (2010) extended the theory to address the problem of fracture intersections and proposed some simple rules that are not present in first-order model. In this paper, we utilize the initial form of the dual power-law model without any modifications. Values of the two power-law

indices,  $D$  and  $a$ , will be bracketed to ranges suggested by extensive measurements in literature. Specifically, studies of 2D outcrops yield estimates for the correlation dimension  $D$  between 1.3 and 2, and the length exponent  $a$  falls between 1.3 and 3.5 (Bonnet et al. 2001; Renshaw 1999). Unfortunately, no estimates of  $D$  and  $a$  for 3D networks are reported in the literature as there is no direct method to image 3D size distribution of fractures at depth.

Before presenting the DFN generation methodology, it is useful to clarify the technique to compute the fractal dimension ( $D$ ) of fracture patterns. Fractal geometry has been widely utilized to quantify the scaling properties of fracture networks (Chilès 1988; Davy 1993). For a detailed analysis of the scaling in fractured media, we refer to Bonnet et al. (2001). The spatial organization of fractures can be quantified by a box-counting technique (Allegre et al. 1982; Berkowitz and Hadad 1997; La Pointe 1988; Odling 1992) or two-point correlation function (Hentschel and Procaccia 1983a). The traditional box-counting technique is strongly affected by finite size effects, whereas the two-point correlation function is less affected by finite size effects and seems a better method to derive the scaling exponent of the spatial distribution of fracture centers in 2D fracture outcrops (Bonnet et al. 2001; Bour et al. 2002). We illustrate this differences in Section 2.3. The two-point correlation function or correlation integral describes the spatial correlation of fracture centers, and is given by,

$$C(r) = \frac{2}{N_t(N_t - 1)} N_p(r) \sim r^D \quad (2.2)$$

where,  $N_t$  is the total number of fractures, and  $N_p$  is the number of pairs of fractures whose center-to-center distance is less than  $r$  (Bonnet et al. 2001). The correlation dimension ( $D$ ) can be determined by computing the local slope of the correlation function  $C(r)$ . The correlation function has been widely used by Earth scientists to characterize the spatial distribution of micro-fractures in rock samples in granite and also earthquake hypocenters (Hirata et al. 1987). Here, we apply the concept of correlation function 1) to validate our synthetic DFN generator and 2) to analyze 1D fracture patterns in deep boreholes.

### 2.2.1 DFN generation methodology

Here, we briefly review and illustrate some DFN generation methodologies that can be found in the literature, and comment on and their possible implications. The conventional Poisson DFN model, also known as the Baecher model, is an early DFN model developed to study the hydraulic and mechanical behavior of fracture networks (Baecher and Lanney 1978; Baghbanan and Jing 2007; Bour and Davy 1997; Bour and Davy 1998; de Dreuzy et al. 2001; de Dreuzy et al. 2002). The concept behind the Poisson DFN model is to populate a medium with a random

(uniform) distribution of fracture centers (Dershowitz et al. 1993). However, this model is not able to represent the tendency of fracture populations to display clustering at different scales. An alternative that does not suffer from this deficiency is the fractal fracture network approach that generates networks that capture the scaling and clustering seen in real fracture networks.

Two methods to generate fractal fracture networks are reported in the literature; 1) The Levy-Lee flight model and 2) Imposing power-law length distribution to fractal spatial distribution of fracture centers generated by Multiplicative Cascade process. The Levy-Lee flight process is a random walk method that generates fractal fracture networks by imposing power-law steps in random directions between  $0^\circ$  and  $360^\circ$  (Clemo and Smith 1997). The distance between two consecutive fracture centers is selected randomly from a power-law distribution with an exponent of  $D$ , and the fracture length is taken as proportional to the distance from the previous fracture (This methodology is implemented in a commercial software package called Fracman). Since the generation domain of fracture networks is limited, the consecutive fractures might extend outside of the 2D and 3D domain. Therefore the fractal dimension ( $D$ ) of the generated network does not necessarily correspond to the input fractal dimension (Darcel 2002). For this reason, we were unable to obtain a correspondence between output and input  $D$  when using Levy-Lee fractal DFN generator.

The methodology based on the Multiplicative Cascade process has already been described in different papers (Darcel et al. 2003c; Harthong et al. 2012; Verscheure et al. 2012), although details of its implementation are lacking. Thus, here we give a step-by-step description of the implementation we have used. This process includes both the generation of a fractal density distribution in a recursive operation of fragmentation and the allocation of a power-law length distribution, as given in equation 2.1. We begin by describing the methodology used to generate 2D fractal networks before progressing to cover 3D network generation.

## **2.2.2 2D fractal DFN generation**

### **2.2.2.1 Initial parameters**

The input parameters required to generate a 2D DFN are: domain length  $L$ , length exponent  $a$  ( $a > 1$ ), correlation dimension of fracture centers  $D$  ( $1 < D \leq 2$ ), density constant  $\alpha$ , and the minimum length of the fractures  $l_{min}$ . The latter is necessary in order to limit the number of iterations in the fractal density distribution and the total number of fractures  $N_t$ . We expect to have a power-law correlation function (equation 2.2) extending from the minimum length

(e.g. 1 m) upwards over at least two orders of magnitude (100 m). The number of iterations  $n$  required to reach the degree of fragmentation set by the minimum length  $l_{min}$  is computed from:

$$l_{min} = \frac{L}{2^n} \quad (2.3)$$

Since we are defining the domain length ( $L$ ) as one of the inputs of the DFN model, there is no constraint on the maximum fracture length  $l_{max}$  and it can vary depending on the length exponent  $a$ . The total number of fractures  $N_t$  can be calculated by integrating equation 2.2 over the fractures larger than the minimum length as in equation 2.4.

$$N_t = \int_{l_{min}}^{\infty} n(l, L) \cdot dl = \frac{\alpha}{a-1} L^D l_{min}^{-(a-1)} \quad (2.4)$$

### 2.2.2.2 Fractal distribution of density (Multiplicative Cascade process)

The fractal density distribution of fractures of given fractal dimension  $D$  is generated using a so-called Multiplicative Cascade process applied to a domain whose size is  $L$  (Darcel et al. 2003c; Lovejoy and Schertzer 1986; Meakin 1991). We have implemented the methodology described by Darcel et al. (2003c) To summarize, in the first iteration, the domain of size  $L$  is subdivided into  $m$  equal-sized sub-domains. Thus, the ratio of sub-domain side length to domain side length is  $l_{ratio} = \sqrt[m]{L}$ . Then  $n$  initial probabilities,  $P_i$ , are chosen that satisfy equations 2.5 and 2.6,

$$\sum_{i=1}^m \frac{P_i^2}{(l_{ratio})^D} = 1 \quad (2.5)$$

$$\sum_{i=1}^m P_i = 1 \quad (2.6)$$

In our implementation, we follow Darcel et al. (2003c) and take  $l_{ratio} = 2$  and  $m = 4$ . The four probabilities are randomly assigned to each of the sub-domains. In the second iteration, each sub-domain (parent) is itself subdivided into four equal parts (offspring). The same four probabilities used in the first iteration are then multiplied by the probability of the parent sub-domain in question and the results randomly assigned to the four offspring sub-domains (Harthong et al. 2012; Verscheure et al. 2012). The process of division and assignment of permuted and multiplied probabilities is then repeated in subsequent iterations to produce a fractal probability map on the domain that has increasingly fine resolution. The map derived from equations 2.5 and 2.6 defines the second order fractal spectrum of the probability field. For a detailed description on the multi-fractal spectrum of a DFN we refer to Bonnet et al.

(2001) and Hentschel and Procaccia (1983a). For  $n$  iterations, the Multiplicative Cascade process generates  $2^n \times 2^n$  probabilities assigned to sub-blocks whose size from equation 2.3 is  $l_{min} = \frac{L}{2^n}$  (assuming  $l_{ratio} = 2$ ). The fractal probability field generated in this way is taken as a proxy for the fractal fracture density distribution.

### 2.2.2.3 *Assigning random fracture centers according to probability maps*

Although the generation of fractal density distributions is well described in the literature (Darcel et al. 2003c; Harthong et al. 2012; Kim 2007), the further step of populating a given probability density map with a realization of a random fracture network has not been described in detail. Thus, we provide a step-by-step description of the procedure we implemented in our DFN generator, which uses the discrete inverse transform method to extract random distributions from the probability density map. We begin by writing the  $[n \times n]$  probability density map as a  $1 \times n^2$  probability density vector by concatenating successive columns, and then taking the cumulative sum of its elements to obtain the cumulative probability density vector  $CumP$ . The cumulative sum of the probability density vector is close but not necessarily equal to unity due to computational inaccuracy in the multiplicative cascade process. Thus,  $CumP$  is normalized by the cumulative sum, giving a monotonically increasing series whose last element is unity.

Now, a fracture assignment vector  $U$  containing  $N_t$  uniform random numbers between 0 and 1 is generated, where  $N_t$  is the total number of fractures to be used in populating the domain (equation 2.4). That is,

$$U = [ u_1 \ u_2 \ u_3 \ \dots \ u_{N_t} ] . \quad (2.7)$$

The discrete inverse transform method is then used to map each element  $U_i$  of  $U$  to the closest matching element of  $cumP$  according to the inequality,

$$cumP_{j-1} \leq U_i < cumP_j \quad (2.8)$$

Thus, each element  $U_i$  of the fracture assignment vector  $U$  is associated with an element  $cumP_j$  of  $cumP$  and hence the corresponding cell of the probability density map. In this way, fracture centers are uniquely assigned to cells of the probability density map, although elements in  $U$  that have the same value will be mapped to the same cell. The specific distribution realized depends upon the random number set used to form  $U$ . The exact position of the fracture center within a cell is attributed randomly using a uniform probability over the cell.

#### 2.2.2.4 Assigning a fracture length to fracture centers

Since the location of every fracture center is known from the section 2.2.2.3, the next step is to assign a length to each fracture center, respecting equation 2.1. At this stage,  $U$  is the vector containing  $N_t$  random numbers and each random number represents a fracture that has been located inside the domain. We define a length vector  $l_f$ , written as in equation 2.9, whose  $N_t$  elements represent the lengths of each fracture written in descending order (i.e.  $l_{f_1} > l_{f_2} > l_{f_3} > \dots > l_{f_{N_t}}$ )

$$l_f = \left[ l_{f_1} \ l_{f_2} \ l_{f_3} \ \dots \ l_{f_{N_t}} \right] \quad (2.9)$$

The index  $f_i$  for each element of the length vector maps to the corresponding index  $i$  of the fracture assignment vector,  $U_i$ , and thus to locations on the probability density map. The actual fracture length of the vectors  $l_f$  are assigned as follows. For a first-order model, the number of fractures having a length between  $l$  and  $l + dl$  is defined by equation 1. Therefore, the number of fractures whose length is greater or equal to a given length  $l'$  is given by,

$$\int_{l'}^{\infty} n(l, L) \cdot dl = \int_{l'}^{\infty} \alpha \cdot L^D l^{-a} \cdot dl = \frac{\alpha}{a-1} L^D l'^{-(a-1)} \quad (2.10)$$

Now, if we select the first fracture in the length vector whose length is  $l_{f_1}$  ( $= l_{\max}$ ), the number of fractures greater than or equal to  $l_{f_1}$  is equal to 1. Therefore, substituting  $l' = l_{f_1}$  into equation 2.10 and equating to unity gives:

$$\frac{\alpha}{a-1} L^D l_{f_1}^{-(a-1)} = 1 \quad (2.11)$$

Similarly, for any index  $i$  of  $l_f$ , the number of fractures whose length is greater than  $l'_{f_i}$  is  $i$ , and thus,

$$\frac{\alpha}{a-1} L^D l_{f_i}^{-(a-1)} = i \quad (2.12)$$

Rearranging equation 2.12 gives an expression for the length of each fracture,  $l'_{f_i}$ , in the length vector,  $l_{f_i}$ , as.

$$l_{f_i} = \left( \frac{\alpha}{a-1} \frac{L^D}{i} \right)^{\frac{1}{a-1}} \quad (2.13)$$

The described methodology of random DFN generation was implemented in a MATLAB script. Figure 2-1 represents a schematic summary of fractal DFN generation using this methodology.

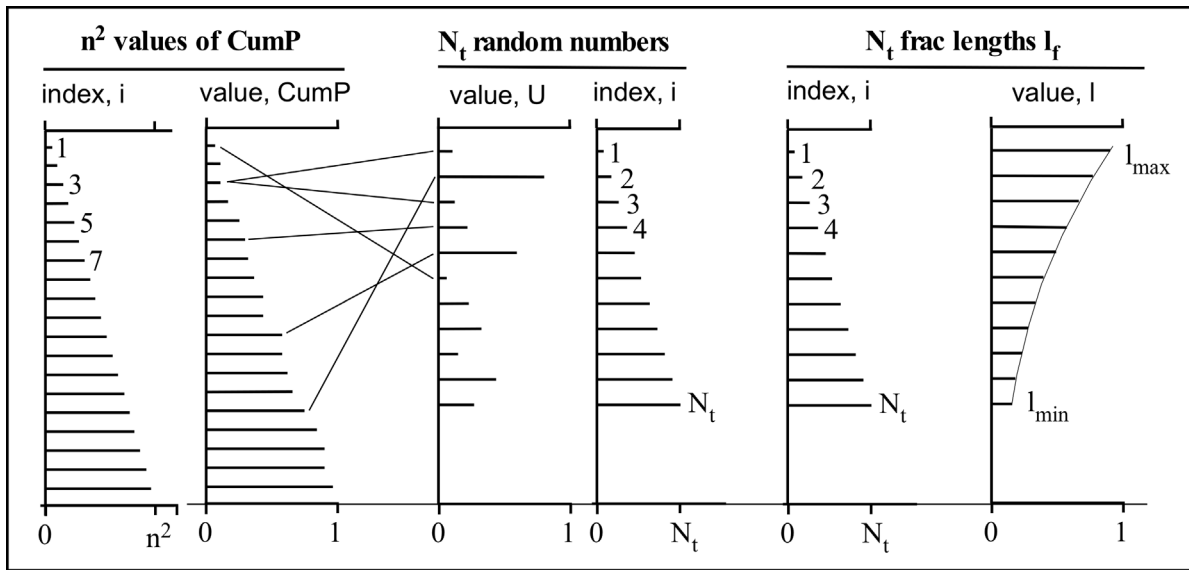


Figure 2-1. Illustration of the procedure for populating the probability distribution map generated using the Multiplicative Cascade process with fracture centers, and then assigning a power-law length distribution to the fractures that is consistent with equation 2.1. The vector  $U$  in the center is the fracture assignment vector.

An example of a fractal probability field generated in a domain of size  $L = 500$  m for a fractal dimension of  $D = 1.5$  is presented in Figure 2-2a. The number of iterations was set to  $n = 6$ . Finer density maps can be obtained by higher number of iterations.

The fractal nature of the distribution of centers and lengths of the resulting DFN was verified by calculating the correlation function and its local slope as well as the complementary cumulative frequency of the length distribution. As an example, the DFN generated with  $D = 1.5$  and  $a = 2$  is shown in Figure 2-2b. The domain size is 500 m, and 5 iterations were performed to give a  $l_{min}$  of 2 m. The two-point correlation function of fracture centers  $C(r)$  given by equation 2.2 was calculated for fracture separations,  $r$ , that were logarithmically uniformly spaced with 20 points for each order of magnitude up to the maximum separation of 500 m. The resulting correlation function is shown in Figure 2-2c, together with the local slope. The slope has a constant value of 1.5 over two orders of magnitude between  $r = 1$ -100 m, as expected. Figure 2-2d shows the logarithm of the number of fractures having a length greater or equal to  $l$  versus the logarithm of  $l$ . The data define a power-law with a slope of  $-1$ , consistent with expectations that the slope should be  $1-a$  [Bonnet et al., 2001].



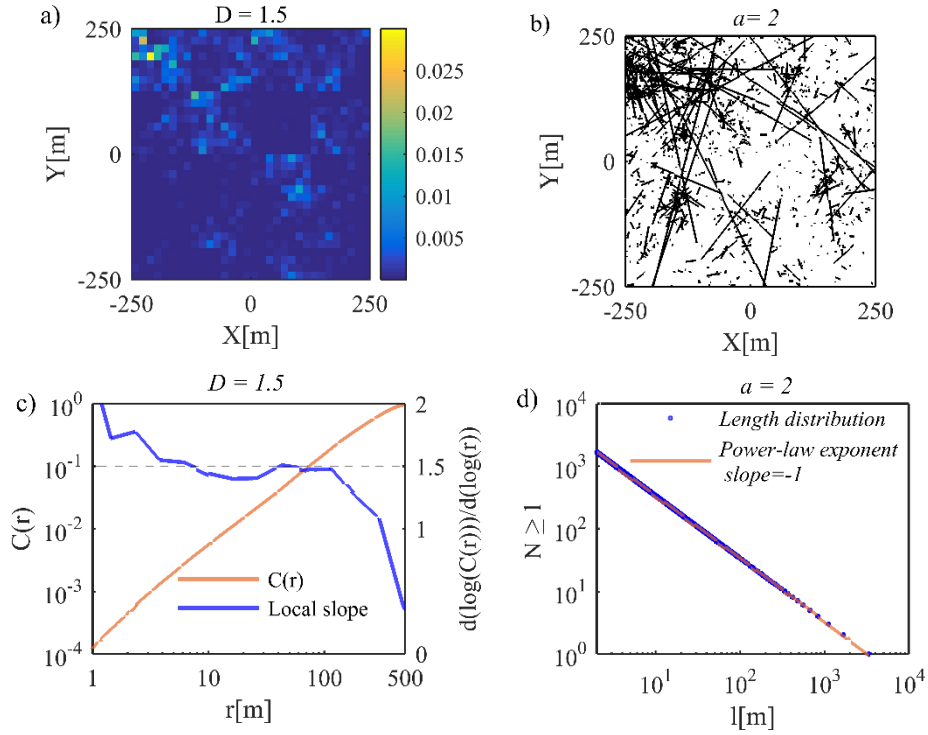


Figure 2-2. (a) Realization of a fracture density distribution in a domain of 500 m for a fractal dimension of 1.5 and an  $l_{\min}$  of 2 m (b) A DFN realization generated from (a) using a length exponent  $a = 2$ . The fracture density parameter,  $\alpha$ , was taken as 0.3 so as to give approximately 1677 fractures (c) Correlation function of fracture centers  $C(r)$  computed from the density distribution in (a), together with the local slope and the slope expected for  $D = 1.5$ . (d) Verification that the cumulative frequency distribution of length computed from (b) is linear with a slope equal to  $1-a$  on a log-log plot.

### 2.2.3 Effect of geometric boundaries on 2D fractal DFNs

Fractures in generated DFNs may extend outside the pre-defined domain ( $L$ ). The application of such DFNs in any modeling scenarios requires a proper understanding of the possible effect of geometric boundaries. The specific geometric boundary implemented may alter the statistics of DFNs from the infinite domain case. In this section, we define two boundary treatment methods and apply them to various 2D DFNs. The first method completely removes those fractures that extend outside the domain length ( $L$ ), and the second trims the fracture sections that protrude out of the domain and reposition the fracture center at the middle of the remaining section. The behavior of fractal DFNs is divided into two main regimes with a transition at  $a = 2$ . We restrict our analysis to the two ranges that lie on either side of the transition and take the width of each range to be consistent with commonly reported natural fracture networks. That is, we take  $1.3 \leq a \leq 2$  and  $2 < a \leq 3.5$ . Higher values of the length exponent  $a$  correspond to a higher ratio of smaller to larger fractures. Thus, values of  $a$  that lie in the first range generate a greater population of large fractures than values that lie in the second range, and hence would

be expected to have higher number of fractures extending outside the domain length and thus have a larger impact on the statistics of the bounded DFN. Figure 2-3 illustrates the results of applying two different boundary treatment methods to the generation of fractal DFNs with length exponents of  $a = 1.5$  and  $a = 2.5$  within a domain of length  $L = 100$  m. The correlation dimension of fracture centers,  $D$  was taken as 1.5 in both cases. Now we explore the spatial distribution and length distribution of DFNs, before and after implementing geometric boundary treatments.

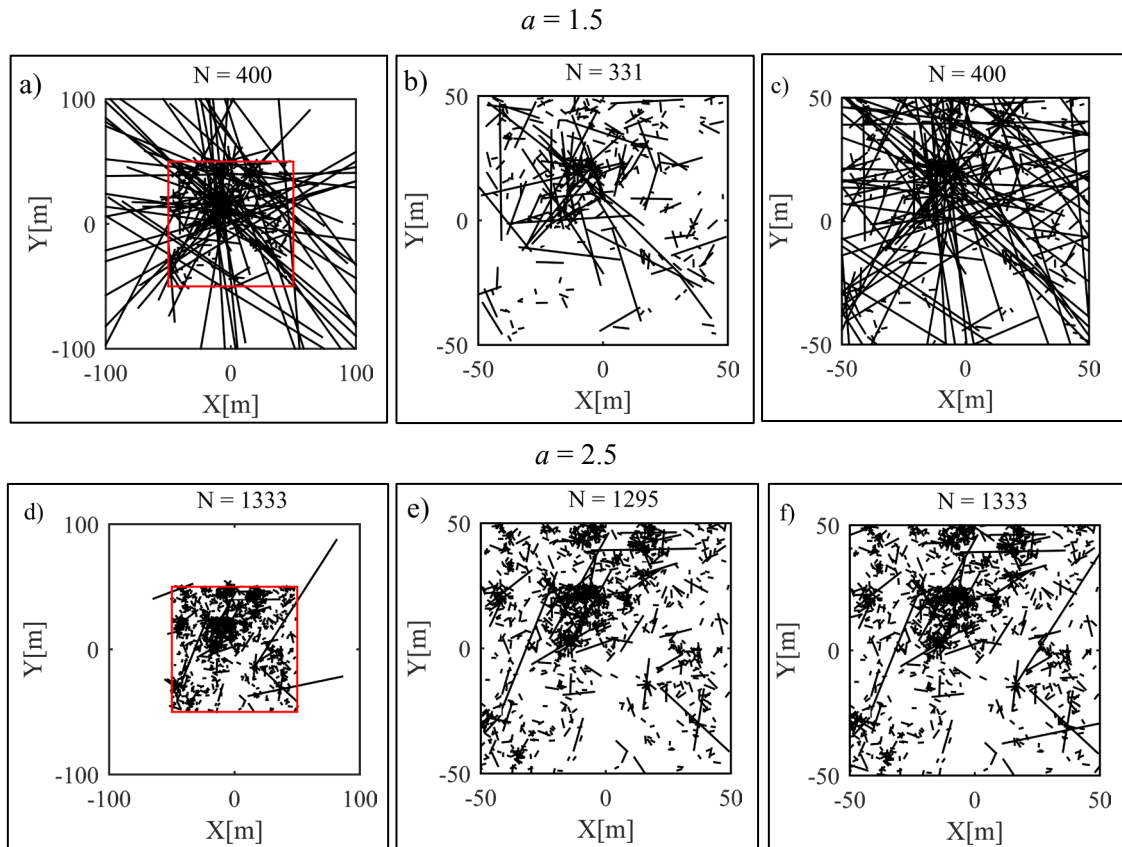


Figure 2-3. (a) Realization of a random fractal DFN generated in a domain of length 100m (outlined in red) with exponents of  $a=1.5$  and  $D=1.5$ , and no geometric boundary imposed (i.e. some longer fractures extend outside the frame boundary at  $\pm 100$  m). (b) The same DFN generated in (a), but with all fractures that extend outside the domain removed. (c) The same DFN generated in (a), but with fractures that extend outside the domain truncated. (d) Realization of a random fractal DFN generated in a domain of length 100 m (outlined in red) with exponents of  $a=2.5$  and  $D=1.5$ , and no boundary imposed. (e) The same DFN generated in (d) but with all fractures that extend outside the domain removed. (f) The same DFN generated in (d), but with fractures that extend outside the domain truncated.

### ***2.2.3.1.1 Removal or trimming of fractures that extend outside the domain***

Figure 2-4a shows the correlation functions,  $C(r)$ , and their log-log slope derived from the DFNs shown in Figures 2.3a-2.3c for the case  $a = 1.5$  that differ in the way fractures that extend outside the domain are treated. The curves denoted ‘fractures remain’ are for the case where all fractures are counted with their true length, regardless of whether they extend outside the domain boundary shown in red in Figure 2-3a. This is presented as a reference. There are 69 that extend outside the domain, which is 17 percent of the total number of fractures. The curve denoted ‘fractures removed’ correspond to the case where these 69 fractures are removed (i.e. Figure 2-3). Clearly, removing the fractures completely has a negligible impact on the correlation function, and the log-log slope, which do not differ significantly from the reference case where all fractures are included. The curve denoted ‘fractures trimmed’ corresponds to the case where fractures are truncated at the domain boundary. It should be noted that truncating the fractures does not change the total number of fractures. However, it does affect the coordinates of the trimmed fracture centers, and hence could affect the statistics of the distance between fracture centers. The log-log slope curve of the trimmed DFN in Figure 2-4a lies slightly above the reference curve defined for all fractures, although not greatly so. The cumulative length distributions for the three cases are shown in Figure 2-4b. Here, the effect of removing the fractures is to progressively deplete the distribution at all length scales, whereas trimming the fractures limits depletion to only the longer fractures. Figure 2-4c and Figure 2-4d show the corresponding correlation functions with their log-log slope functions, and the cumulative length distributions for a DFN generated with  $a = 2.5$ . Again, curves are shown for the cases where fractures that extend outside the domain are either retained with their full length, removed, or trimmed (i.e. Figure 2-3d-Figure 2-3f respectively). For the realization used in this example, 38 fractures extend outside the domain, which is 2% of the total number of fractures. Evidently, the effect of removing or trimming the fractures on the correlation functions and their associated log-log slope functions is negligible, and the cumulative length distributions differ significantly only at fracture lengths greater than 20 m.

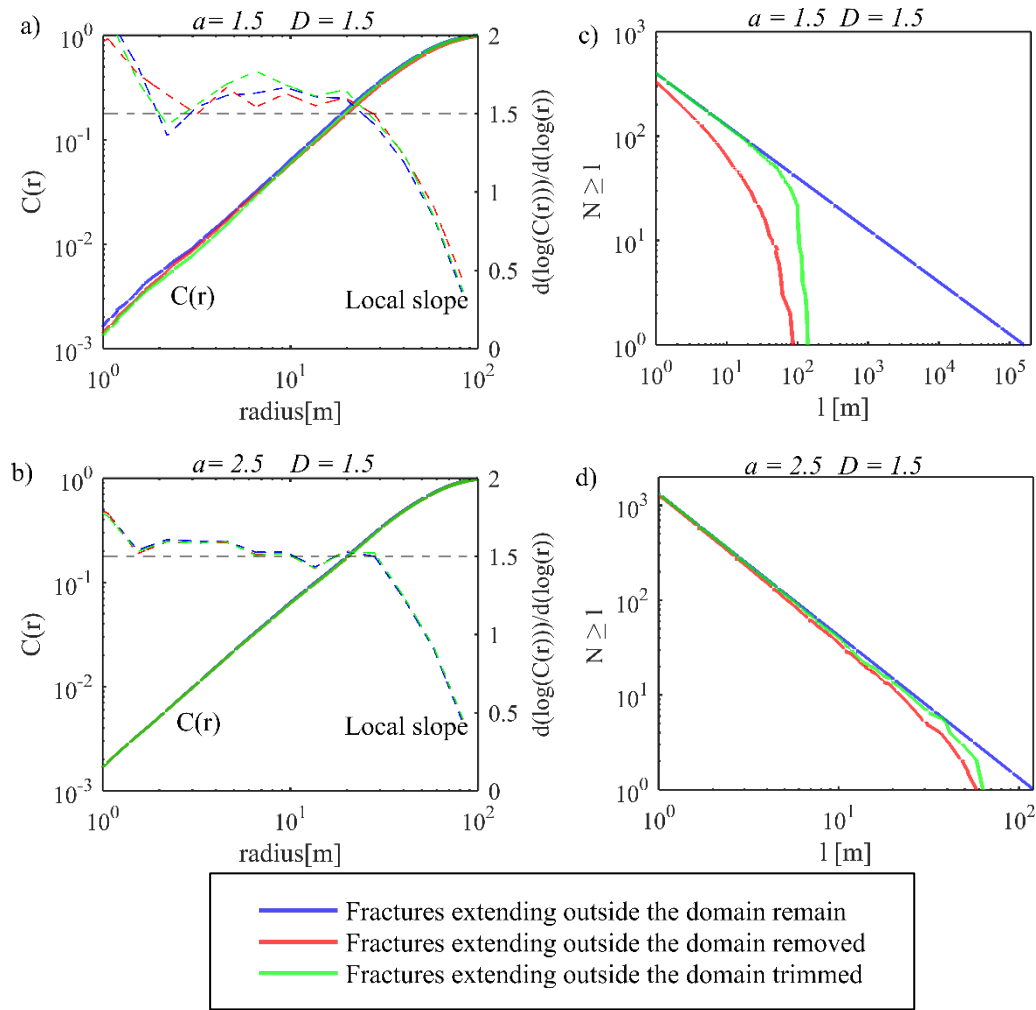


Figure 2-4. Effect on correlation functions and length distributions of applying different approaches to the problem of fractures that extend beyond the domain boundary, namely to remove the fractures (blue), or to trim them so they do not extend beyond the domain boundary (green). The curves obtained by including such fractures with their true length are shown for comparison (brown), (a) Correlation functions and their log-log slope, and (b) length distributions derived from the DFNs in Figure 2.3a and 2.3b which correspond to the case  $a = 1.5$ . The log-log slopes of the  $C(r)$  functions should be flat and equal to 1.5, the correlation dimension of 1.5 shown by the black dashed line. (c) Correlation functions and their log-log slopes and (d) length distributions derived from the DFNs in Figure 2.3d and 2.3e which correspond to the case  $a = 2.5$ .

## 2.2.4 3D DFN generation and verification

DFN generation in three dimensions is identical to two dimensions, except that the density distribution is slightly different. A 3D probability map of a given fractal dimension is produced by generating eight initial probabilities (instead of four as in 2D fragmentation), subdividing each block into to eight sub-blocks, assigning a random permutation of the eight initial probabilities to the sub-blocks of each parent, and finally multiplying the permuted probabilities

by the parent probability. The rest of the generation methodology follows the 2D procedure. Figure 2-5a represents a 3D DFN generated in a 500 m domain using the dual power-law model with the parameters  $D = 2.7$ ,  $a = 2.8$ ,  $\alpha = 0.02$  and  $l_{min} = 10$  m. Figure 2-5b and Figure 2-5c demonstrate the fractal nature of the spatial and length distributions of the fracture network respectively ( $r$  and  $R$  represents the distance between fracture centers and the radius of a fracture plane). For this demonstration, fractures that extend outside the domain boundary were included with their full length.

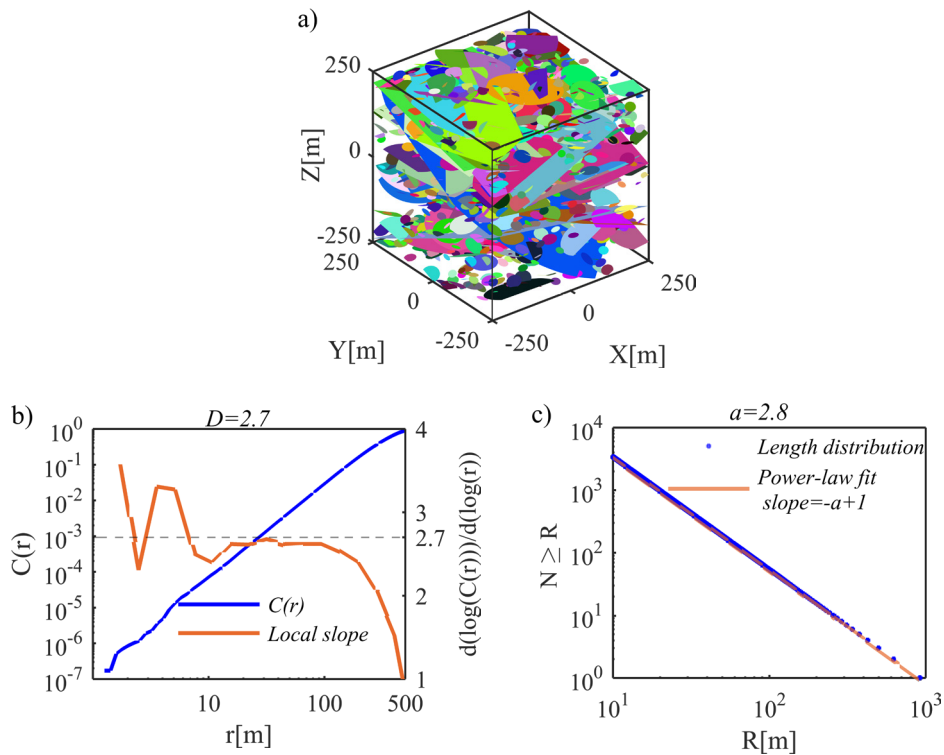


Figure 2-5. (a) A synthetic 3D network generated in a 500 m domain using dual power-law model with  $D = 2.7$ ,  $a = 2.8$ ,  $l_{min} = 10$  m and  $\alpha = 0.02$ . b) Correlation function and its local slope of the generated network. c) Complementary cumulative length distribution of the generated network ( $N$  is the number of fractures larger than size of  $R$ ).

### 2.2.5 Stereological analysis

Stereological relationships relate the geometrical properties of a DFN in different dimensions (e.g. a 2D trace plane intersecting 3D network or a 1D scanline intersecting a 2D trace plane). A detailed stereological analysis of fractal DFNs is presented by Darcel et al. (2003b). In this section, we focus on the relationships derived for relating 1D scanlines intersecting 2D and 3D synthetic networks. For the length distributions, there is a simple relationship between  $a_{2D}$  and  $a_{1D}$  given by equation 2.14.

$$a_{1D} = a_{2D} - 1 \quad (2.14)$$

Since the lengths of fractures intersecting a borehole are essentially not observable, this relationship is not relevant here. The exponent of the spatial distribution of fracture centers ( $D_{2D}$ ) in a 2D  $L \times L$  domain is related to the exponent of the spatial distribution of fracture intersections of a 1D scanline of length  $L$  ( $D_{1D}$ ) by a relation whose form depends on the length exponent of the DFN, as given in equations 2.15-2.17, and Darcel et al. (2003b):

$$D_{1D} = 1, \quad a_{2D} \leq 2 \text{ and } a_{2D} \leq D_{2D} \quad (2.15)$$

$$D_{1D} = D_{2D} - a_{2D} + 1, \quad a_{2D} \leq 2 \text{ and } a_{2D} \geq D_{2D} \quad (2.16)$$

$$D_{1D} = D_{2D} - 1, \quad a_{2D} \geq 2 \quad (2.17)$$

Darcel et al. (2003b) performed numerical simulations attempt to verify the above stereological relationships in synthetic DFNs, but found that they were only partly valid. Here we use a different approach to stereological analysis to clarify the range of validity of equations 2.15-2.17.

For the 2D stereological analysis, we generate fractal fracture networks in a domain of  $512 \times 512 \text{ m}^2$  and trim the outliers. The length exponent is assumed to lie between 1.5-3.5 *and* correlation dimensions of fracture centers vary between 1-2. The minimum length of the fractures in the each model is set to 1 m. Then, we place scanlines in every 1 m parallel to X and Y-axis (i.e. 1025 scanlines in total) and compute the location of the fracture intersections on each scanline. The correlation function of these intersections (fracture locations) provides an estimate of the  $D_{1D}$  within the range of 1-100 m. Finally, we plot the values of  $D_{1D}$  as a function of  $D_{2D}$ .

The analysis was performed on two sets of 2D fractal DFNs with different length exponents of  $a_{2D} = 1.5$  and  $a_{2D} = 2.5$ . For each length exponent, the correlation dimension  $D_{2D}$  was varied from 1.1 to 1.9 in steps of 0.1 (i.e.  $D_{2D} = 1.1, 1.2, \dots, 1.9$ ), and a single DFN with random fracture orientation generated for each step. For each value of length exponent  $a_{2D}$ , the constant  $\alpha$  in equation 2.1 was adjusted for each step to produce a large and constant number of fractures centered in the domain, thereby eliminating the effects of the number of fractures on the analysis whilst ensuring a large number of intersections with 1D sampling lines. For  $a_{2D} = 1.5$ ,  $\alpha$  was chosen so as to produce approximately 20,000 fractures (approximate  $P_{21}$  of 40), whilst a value that generated approximately 200,000 (approximate  $P_{21}$  of 4) was used for  $a_{2D} = 2.5$ . The difference in the number of fractures compensates for the tendency for  $a_{2D} = 2.5$  to generate proportionally fewer larger fractures and hence fewer intersections. Scan lines were defined across the DFNs (1025 scanlines of size  $L$  placed in every 1 m parallel to x-axis and y-axis) and

the 1D correlation dimension,  $D_{1D}$ , computed. Figure 2-6a shows the resulting values of  $D_{1D}$  obtained as a function of  $D_{2D}$  for  $a_{2D} = 1.5$  together with the trends expected from equations 2.15 and 2.16. Clearly, for  $D_{2D} \geq a_{2D} = 1.5$ , the values of  $D_{1D}$  scatter closely around 1, which is consistent with expectations from equation 2.15. However, for  $D_{2D} \leq a_{2D}$ , the analysis indicates a progressive discrepancy between the values of  $D_{1D}$  obtained from the realizations and the stereological relationship of equation 2.16. Similar observations are reported by Darcel et al. (2003b) who referred to this range as a transition regime.

The corresponding results for a length exponent of 2.5 are shown in Figure 2-6b together with the expected trend from equation 2.17. It is evident that the  $D_{1D}$  values derived from the scan lines overestimate the values expected from equation 2.17 for all values of  $D_{2D}$ , the overestimate increasing for smaller values of  $D_{2D}$ . Similar results were found by Darcel et al (2003b) who plotted only the average values of the  $D_{1D}$  values as a function of  $D_{2D}$ .

The stereological analyses presented above consider DFNs that have a random orientation of fractures. However, fractures mapped in boreholes or outcrops commonly fall into one of several discrete orientation sets that reflect the fracture families present in the rock mass. As an example, Ziegler et al. (2015) used a fracture imaging log run in the Basel-1 borehole to characterize the natural fracture distribution in the rock mass penetrated by the well. They identified six potential fracture sets based on their orientation. To investigate the impact of preferred orientation of fractures on the stereological analysis, a 2D fractal DFNs were generated that contained only two fracture sets which subtended angles of  $45^\circ$  and  $135^\circ$  from x-axis. The procedure and parameter values used in the stereological analyses were the same as those applied for the random fracture orientation cases. The results, shown in Figure 2-6c and Figure 2-6d for  $a = 1.5$  and  $a = 2.5$  respectively, are almost similar to the random orientation cases. Various fracture orientation configurations have been tested leading to the same conclusion.

It is of practical interest to examine the stereological relationship between fractures sampled along 1D scan lines (i.e. boreholes) cutting through 3D fracture networks. Darcel et al. (2003b) have shown the equations defining the theoretical stereological relationships between 2D trace planes and 3D synthetic networks are given by equations 2.18-2.20.

$$D_{2D} = 2, \quad a_{3D} \leq 2 \text{ and } a_{3D} \leq D_{3D} - 1 \quad (2.18)$$

$$D_{2D} = D_{3D} - a_{3D} + 1, \quad a_{3D} \leq 2 \text{ and } a_{3D} \geq D_{3D} - 1 \quad (2.19)$$

$$D_{2D} = D_{3D} - 1, \quad a_{3D} \geq 2 \quad (2.20)$$

Combining the above 3D to 2D equations with the 2D to 1D relations of equations 2.15-2.17 gives the required 3D to 1D equations as equations 2.21-2.22.

$$D_{1D} = 1, \quad a_{3D} \leq 2 \quad (2.21)$$

$$D_{1D} = D_{3D} - 2, \quad a_{3D} \geq 2 \quad (2.22)$$

We performed a similar stereological analysis to those done previously, this time using 3D DFNs generated with  $a = 1.5$  and  $2.5$ , and  $D_{3D}$  varied from  $2.1$  to  $2.9$  in steps of  $0.1$ . Fracture orientations were random. For each DFN generated for each step, the 1D correlation dimension,  $D_{1D}$  was measured along 512 boreholes aligned with the z-axis and spaced every meter in the x-axis direction. The resulting  $D_{1D}$  values are shown as a function of  $D_{3D}$  in Figure 2-7a and Figure 2-7b for  $a = 1.5$  and  $2.5$  respectively, together with the trends from equations 2.21-2.22. For all values of  $a_{3D}$ , the computed  $D_{1D}$  remains in average close to 1, which illustrate the impossibility to extract 3D fractal dimension from 1D samples.

### 2.3 1D spatial distribution of fractures

Fractal geometry has widely been applied to characterize 1D scanlines in natural fracturing systems (Boadu and Long 1994; Ledésert et al. 1993; Manning 1994; Merceron and Velde 1991; Moein et al. 2016; Roy et al. 2014). Here, we review the available techniques to estimate the fractal dimension of fractures intersecting 1D scanlines. Then, we apply these techniques to estimate the fractal dimension of synthetic patterns of known fractal dimension to find out the best and most reliable methodology to characterize 1D fracture patterns.

#### 2.3.1 Synthetic fractures

We applied the multiplicative cascade process to generate 1D fractal patterns with a given fractal dimension, which is described in section 2.2.2. The main differences are: 1) the generation domain that is reduced to a line of size  $L$  m (instead of a square of  $L \times L$  m<sup>2</sup>) and the number of initial probabilities that are reduced to 2 (instead of four). The fragmentation process is done with a division of domain size into two subdomains in each iteration (i.e.  $l_{ratio} = 2$ ). The initial parameters required to generate fractal patterns of fractures on a single scanline are the number of iterations  $n$ , the number of fracture population  $N_f$  and the scanline length of  $L$ . For our application, since we are interested in the spatial distribution of intersection only, we skip the steps that assigns fracture length to fracture locations on scanlines. Here, we set  $L = 512$  m,  $n = 16$  and populate 1,000 random fracture locations with a fractal dimension of  $D_{1D} = 0.75$ . Figure 2-8a represents a schematic representation of fractures on a sample synthetic scanline with original length of 512 m. For the sake of visibility, only 64 m of the scanline is



presented in this figure. Then, we apply three different techniques to estimate the fractal dimension of this synthetic 1D scanline and evaluate the limitation and accuracy of each methodology.

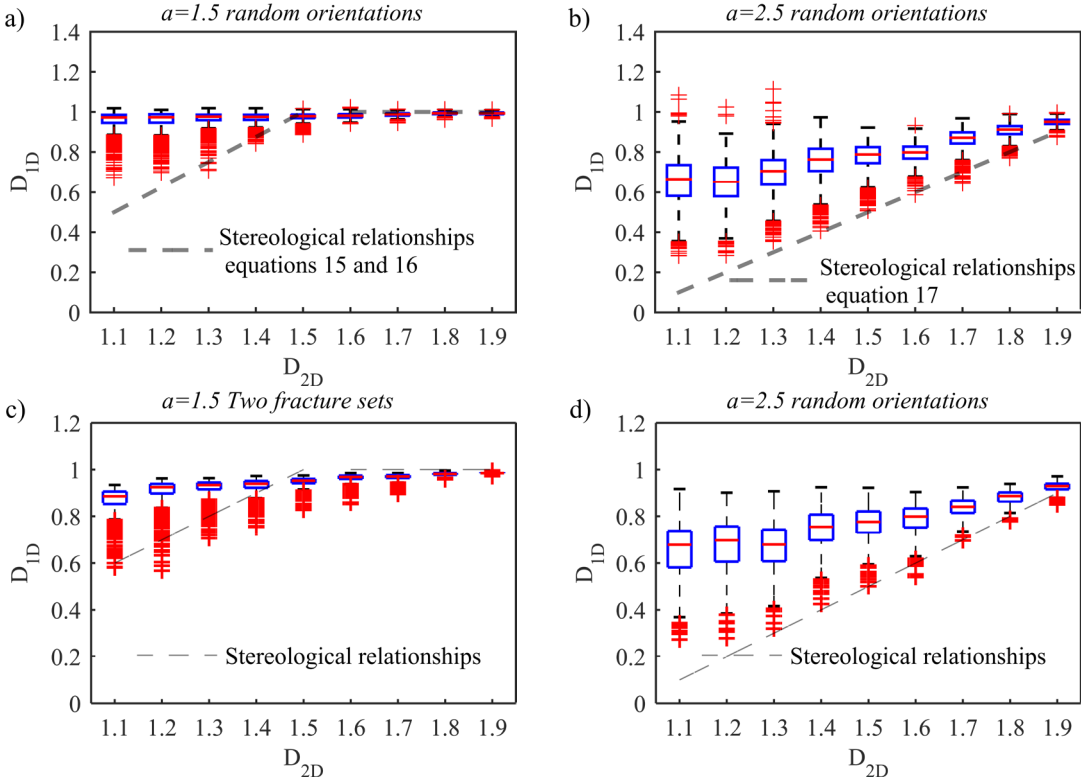


Figure 2-6. Stereology plot of 1D lines sampling a 2D fractal fracture network. (a) Values of  $D_{1D}$  obtained from DFN realizations with random fracture orientations generated with  $a = 1.5$  as a function of  $D_{2D}$ . For a given  $D_{2D}$  value, the red line in the box denotes the median value of  $D_{1D}$  taken over the realizations, and the lower and upper edges of the box denote the 25 and 75 percentile values respectively whose difference denotes the inter quartile range (IQR). The horizontal short black lines lie 1.5IQRs from the upper and lower edges of the 25 and 75 percentiles. Red crosses are realization falling outside this range. (b) Same as (a) but with  $a_{2D} = 2.5$  with random fracture orientations. (c) Same as (a) but with  $a_{2D} = 1.5$  and two perpendicular sets. (d) Same as (a) but with  $a_{2D} = 2.5$  and two orthogonal sets.

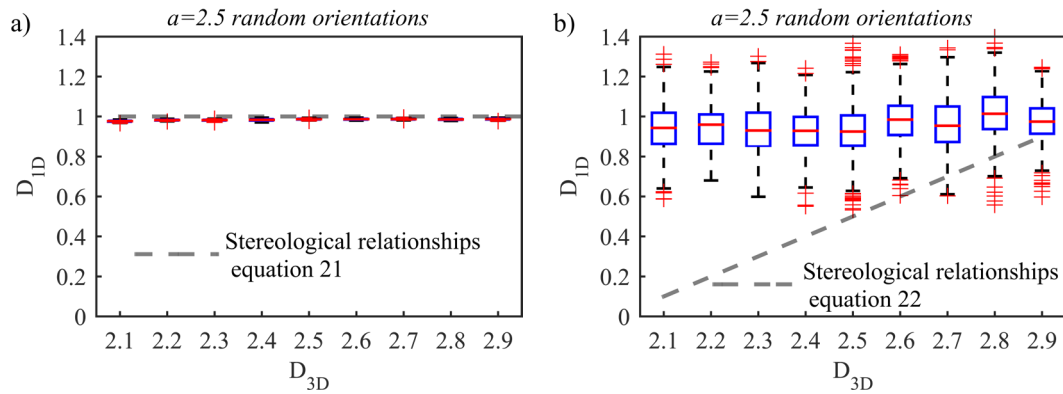


Figure 2-7. Stereology plot of 1D lines sampling a 3D fractal fracture network. (a) Values of  $D_{1D}$  obtained from DFN realizations with random fracture orientations generated with a length exponent  $a_{2D} = 1.5$  as a function of  $D_{3D}$  with random orientations. (b) Same as (a) but for a length exponent  $a_{2D} = 2.5$  with random orientations.

### 2.3.1.1 Two-point correlation function

Two-point correlation function computes the correlation dimension similar to 2D networks using equation 2. Figure 2-8b displays the application of two-point correlation function to compute the correlation dimension ( $D$ ) of the synthetic fracture patterns of Figure 2-8a. The computed correlation dimension is reasonably stable and close to the initial fractal dimension ( $D = 0.75$ ) for almost two orders of magnitude.

### 2.3.1.2 Box-counting technique

The box counting technique consists of dividing the data space (here the scanline) in rulers of equal sizes  $t$  and determining how many rulers contain data  $N_b(t)$ , i.e. the rulers covering the entire fracture dataset. This approach has been also referred as Cantor's dust method for 1D fracture datasets (Velde et al. 1991). The division of the data space is repeated sequentially, generating smaller rulers at each iteration. If the distribution of fracture intersections follows a fractal behavior, then the following relation is valid  $N_b(t) \sim t^{-D_b}$ . The box-dimension is then evaluated by measuring the local slope of the  $N_b(t)$  data vs.  $t$  in a log-log plot. This slope will not be constant over the entire range and different regimes develop. When there is a small number of large rulers, all rulers will contain data and the local slope will essentially be  $-1$ . On the other hand, when rulers have size smaller the minimum data spacing, the number of rulers containing data will become a constant equal to the number of data point and the slope on the log-log plot will tend to zero. In between these two extreme cases, a regime with a constant slope should develop if the data set is truly fractal, and this constant slope is an estimator of the fractal dimension of the data set. Figure 2-8c displays the application of box-counting techniques to compute the box dimension of the synthetic patterns on Figure 2-8a. The local

slope of  $N_b(t)$  does not show fractal regime in which the local slope is constant for a considerable range.

### 2.3.1.3 *Power-law distribution of spacing*

Power-law exponent of spacing distributions is extracted from the intersection of fractures with a borehole. *ID* scanlines generate a dataset of fracture spacing that is defined as the depth difference between two consecutive intersections. An approach to estimate the fractal dimension of the intersection of fractures with the borehole is to evaluate the cumulative spacing distributions Gillespie et al. (1993). The cumulative spacing distribution is the plot of the number of spacing  $N_s$  greater or equal, to specific spacing ( $s$ ). When displayed in a log-log space, one can estimate the fractal dimension by fitting a line in the linear section with a power-law exponent (i.e.  $N_s(t) \sim s^{-D_s}$ ). Figure 2-8d displays cumulative distribution of fracture spacing applied to synthetic patterns on Figure 2-8a. Similar to box-counting technique, the local slope of  $N_s(s)$  does not show any constant value for a considerable range. Here we tried to fit a constant slope for one order of magnitude and found out a  $D_s = 0.75$ .

The comparison of these three techniques to estimate a fractal dimension to the fracture spacing reveals that correlation function delivers a stable and reliable estimates. Although the statistical distribution of fracture spacings provides a similar fractal dimension, it has a smaller range of validity. On the other hand, the estimates of fractal dimension from box-counting technique is biased and shows no constant slope for any ranges. Bour et al. (2002) applied box-counting technique directly, to characterize the 2D outcrops from Hornelen basin and found almost no fractal dimension. However, they assigned a correlation dimension to the fracture centers, which appears to be the true fractal dimension.

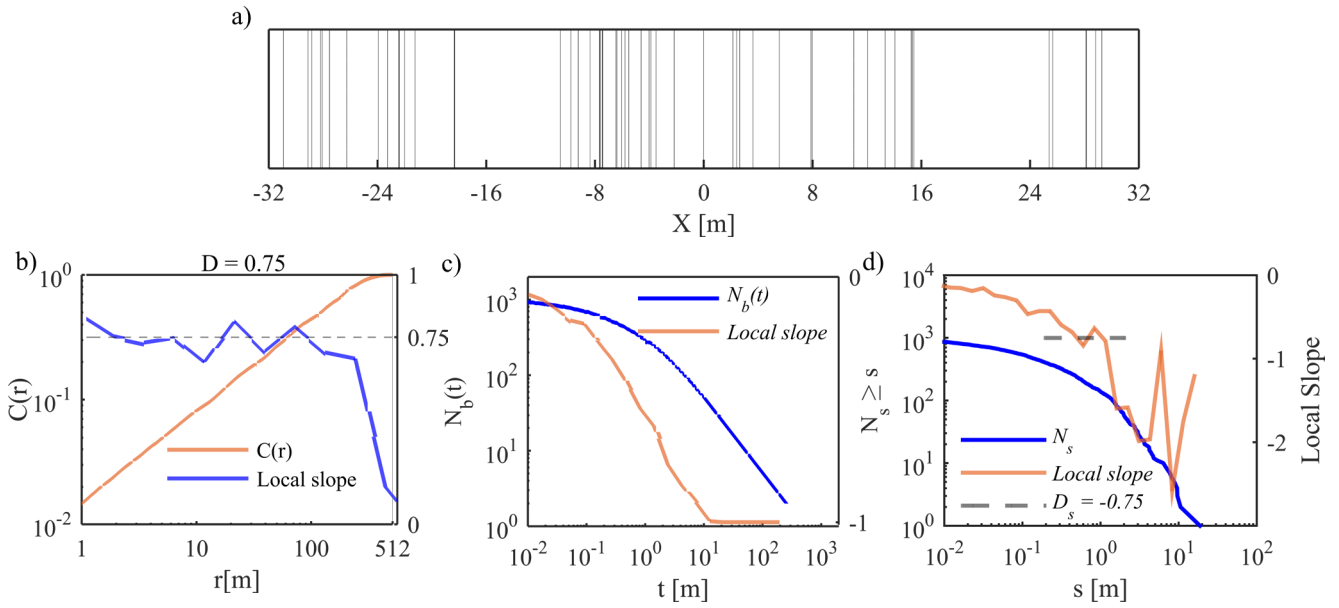


Figure 2-8. (a) A schematic view of a synthetic fracture pattern on a 1D scanline, generated using 1D multiplicative cascade process with a  $D_{1D} = 0.75$ ,  $L = 512$  m and  $n = 16$ . For the sake of visibility, only 64 m of the entire domain is plotted. The number of fractures in the entire domain is 1,000. (b) Two-point correlation function and its local slope of the synthetic 1D scanline generated in a. (c) Box-counting analysis and its corresponding local slope of the synthetic 1D scanline generated in a. (d) Complementary cumulative distribution of spacing and its local slope of the synthetic 1D scanline generated in (a).

### 2.3.2 Natural fractures in deep boreholes

The primary source of natural fracturing systems in deep wells stems from borehole wall image logs such as the acoustic televiewer. Fractures are identified and their orientation obtained by fitting sinusoids to their traces on unwrapped images. Although the resolution of acoustic televiewer logs does not permit the identification of very thin discontinuities (Genter et al., 1997), the resulting fracturing dataset usually provides a reasonably complete sampling of the fracture families present in a rock mass. Our data-set involves the fracture data from a 5 km deep geothermal well, Basel-1, located near Basel in Switzerland, and two 5 km deep wells, GPK3 and GPK4, at the Soultz Geothermal Project at Soultz-sous-Forêts in France. The depth of fractures in the borehole logs has been converted from measured depth (MD) to true vertical depth (TVD) below ground.

In earlier studies, the fractures in each borehole were picked and assigned to fracture sets based to their orientation. The sets and their mean orientations are listed in Tables 1 and 2, and are ranked in terms of the number of fractures they contain. Six fracture sets were recognized in Basel-1 (Ziegler et al., 2015) and seven sets in GPK3 and GPK4 (Valley and Genter 2007; Ziegler et al. 2015), although some fractures could not be assigned to any of the fracture sets.

Table 2-1. Number of fractures in sets and corresponding mean orientations in Basel-1(Ziegler et al., 2015)

Fracture Set	Number of fractures	Mean dip direction °	Mean dip angle °
1	348	250	66
2	297	68	62
3	173	195	61
4	152	307	68
5	53	37	68
6	12	133	76
Total number of fractures = 1164			

Table 2-2. Number of fractures in recognized sets and corresponding mean orientations in boreholes GPK3 and GPK4 at the Soultz-sous-Forêts site

Fracture Set	Number of fractures		Mean dip direction °		Mean dip angle °	
	GPK3	GPK4	GPK3	GPK4	GPK3	GPK4
1	625	749	269	272	68	70
2	584	708	85	85	66	64
3	324	411	136	122	72	74
4	297	231	280	271	74	77
5	27	40	177	200	33	24
6	63	55	185	203	76	80
7	6	21	189	170	54	46
Total number of fractures in GPK3 = 1926						
Total number of fractures in GPK4 = 2115						

#### 2.3.2.1 *Application of different techniques to characterize 1D for natural fractures*

Here, we applied correlation function technique, box-counting method and statistical distribution of spacing to compute the fractal dimension of fracture patterns in Basel-1 well. For this analysis, the entire fracture dataset is selected regardless of the orientations. Figure 2-9a shows that the fractal dimension computed from correlation dimension is reasonably constant for two orders of magnitude. On the other hand, box-counting technique does not show a plateau in the entire range (Figure 2-9b) and statistical analysis of spacing distribution shows a constant slope for less than one order of magnitude with a fractal dimension of 0.21 (Figure 2-9c). According to the analysis of synthetic data, the correlation dimension seems to be the true fractal dimension of fracture patterns in deep boreholes.

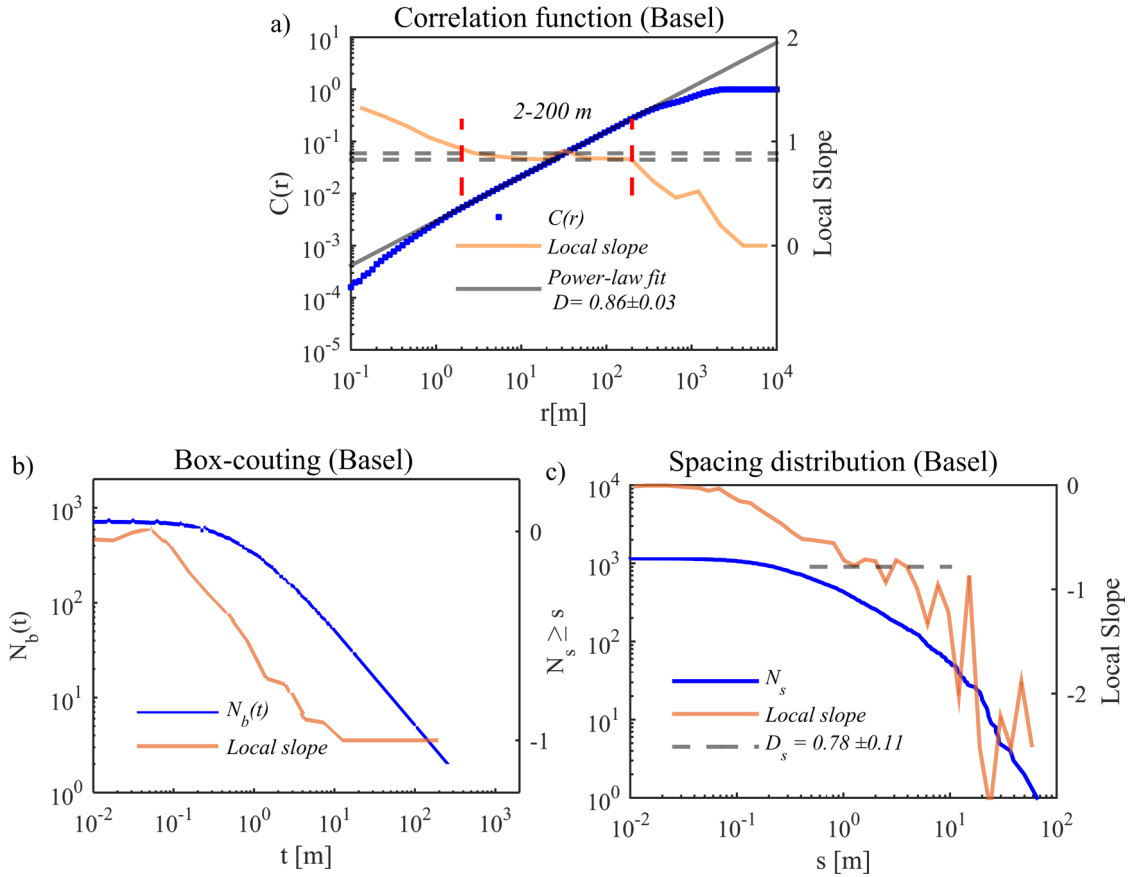


Figure 2-9. Application of three different techniques to compute the fractal dimension of fracture patterns in Basel-1 borehole, a) two-point correlation function, b) box-counting technique and c) statistical distribution of spacing.

### 2.3.2.2 1D Spatial distribution of fracture sets

In this study we included all fractures in the sets regardless of the uncertainty in their identification. We consider only first four sets (1–4) of the three boreholes which are the most populous. The number of fractures in other sets is too small to perform a fractal analysis. For each of the four sets, two-point correlation functions of fracture intersection depths (in TVD) along the boreholes were computed for 500 points logarithmically distributed uniformly in the range 0.1–10,000 *m* (i.e. 100 for every order of magnitude). The local slopes of the log-log plots of the  $C(r)$  function were calculated for 25-point wide windows that were progressively moved across the  $C(r)$  curves without overlap, thereby giving four slope values per decade.

The  $C(r)$  and log-log slope functions obtained from the analysis of the Basel-1 fracture sets are shown as functions of  $r$  in Figure 2-10. In all cases, the log-log slope appears reasonably flat save for local fluctuations for a range of  $r$ -values that span at least 2 – 200 *m*, demonstrating that the spacing of the fracture intersection points is fractal over scales of at least 2 – 200 *m*. The best-fitting horizontal lines to the slope functions over this range gave the  $D_{1D}$  estimates of

between 0.65 and 0.75, which are listed in Table 3 together with their standard deviations and corresponding ranges of validity.

Table 2-3. 1D Fractal dimension of fracture patterns in three deep boreholes and the corresponding range. Correlation dimension obtained from the analyses of fracture intersection spacing in the three wells

Fracture Set	$D_{1D}$ (Basel-1) range	$D_{1D}$ (GPK3) Range	$D_{1D}$ (GPK4) range
1	$0.75 \pm 0.08$ 1.3-400 m	$0.74 \pm 0.05$ 2-1000 m	$0.75 \pm 0.11$ 1-2000 m
2	$0.69 \pm 0.07$ 2-200 m	$0.72 \pm 0.05$ 3-1000 m	$0.74 \pm 0.1$ 2-2000 m
3	$0.65 \pm 0.16$ 2-200 m	$0.71 \pm 0.08$ 2-1000 m	$0.68 \pm 0.12$ 1-1000 m
4	$0.67 \pm 0.08$ 2-400 m	$0.72 \pm 0.09$ 06-200 m	$0.66 \pm 0.09$ 1-200 m
Entire Dataset	$0.86 \pm 0.03$ 2-200 m	$0.88 \pm 0.02$ 2-1000 m	$0.87 \pm 0.06$ 2-1000 m

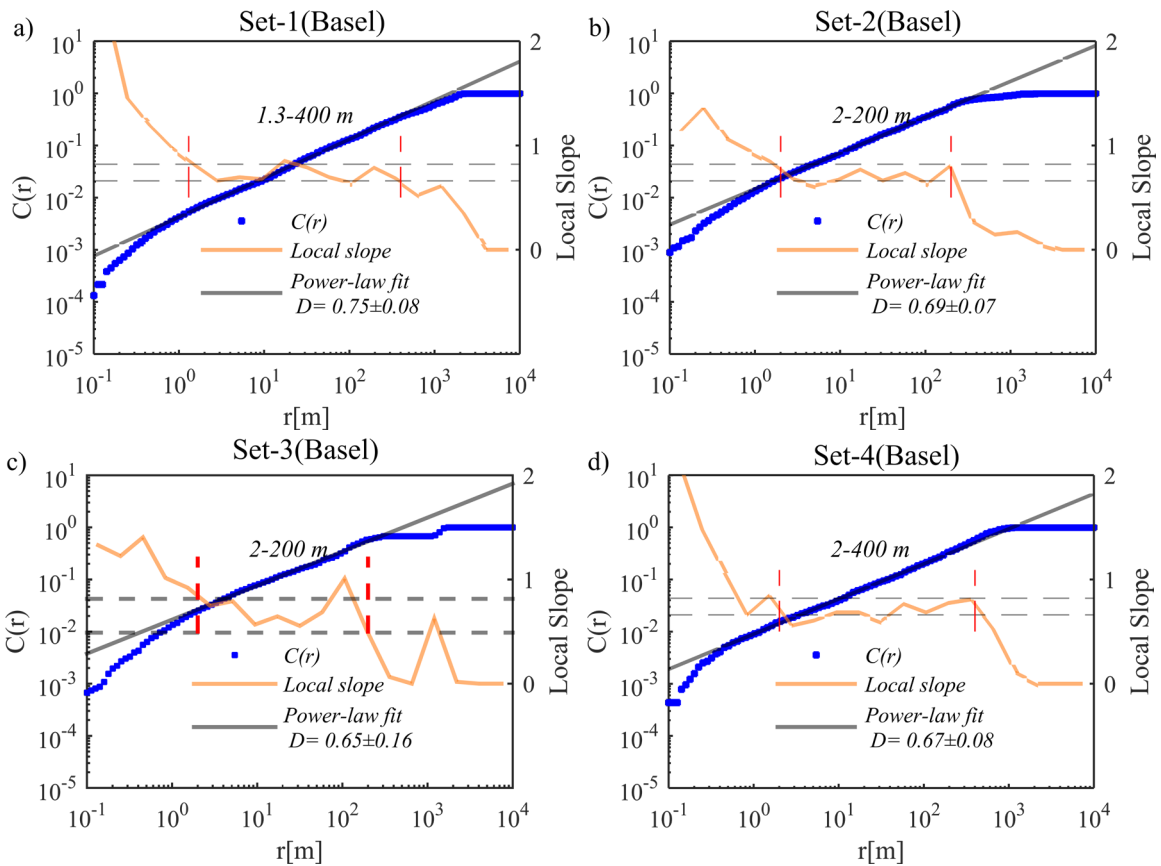


Figure 2-10. Correlation and log-log slope functions of fracture sets in the Basel-1 well. The best-fit horizontal line to the log-log slope function over the  $r$  range of 2-200 m which gives the value of  $D_{1D}$  is shown together with the standard deviation. The range of  $r$  over which fractal scaling is seen is indicated between the vertical lines drawn at the 1 sigma variation of  $D_{1D}$ . (a) set 1, (b) set 2, (c) set 3, (d) set 4.

Identical analyses were performed on the natural fracture sets imaged in GPK3 and GPK4 of the Soultz-sous-Forêts geothermal reservoir, and the correlation and log-log slope functions are shown in Figure 2-11 and Figure 2-12, respectively. In all cases, the log-log slope has a reasonably constant value over two and in some cases, three orders of magnitude. The correlation dimension ( $D_{ID}$ ) estimates for GPK3, obtained from the best-fit horizontal line over range 1-200 m, varying between 0.71 and 0.75 (Table 3), whereas those for GPK4 range between 0.66 and 0.75.

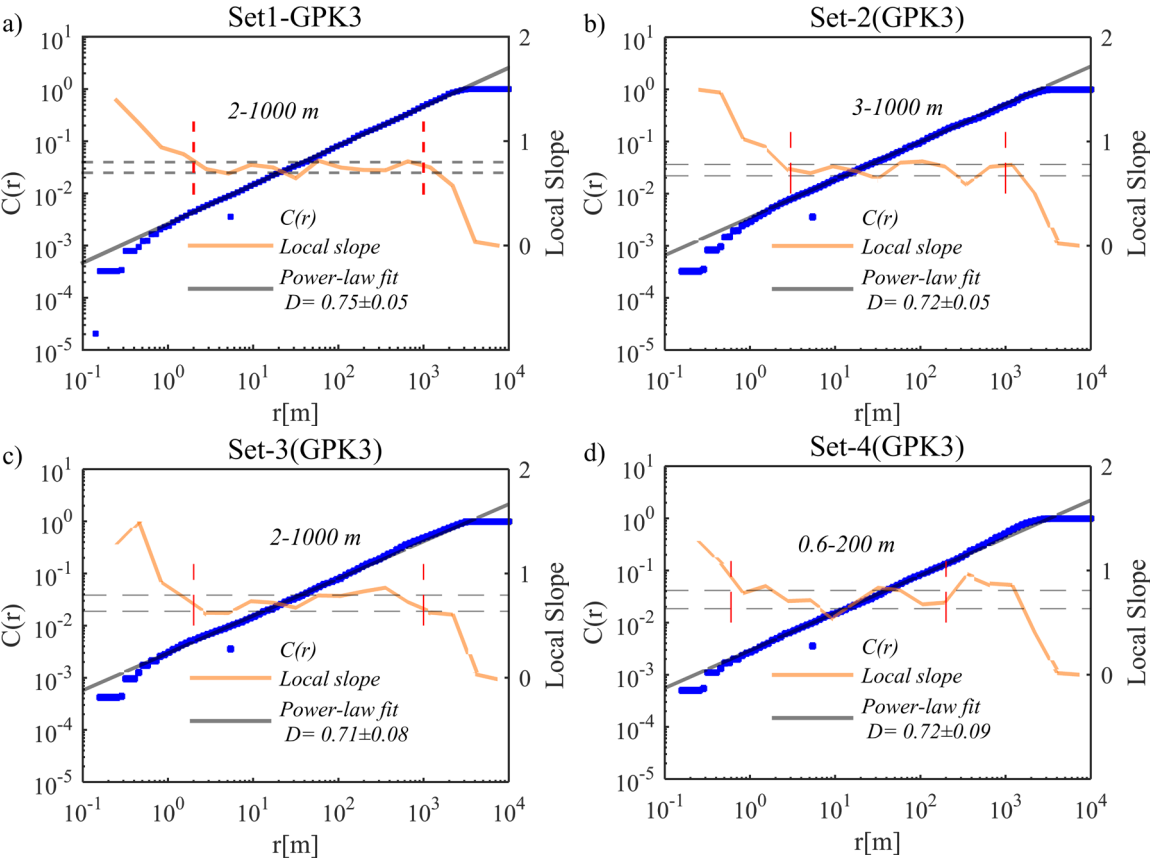


Figure 2-11. Same as Figure 2.10 but for the four fracture sets identified in the GPK3 well at the Soultz geothermal site: (a) set 1, (b) set 2, (c) set 3, (d) set 4.



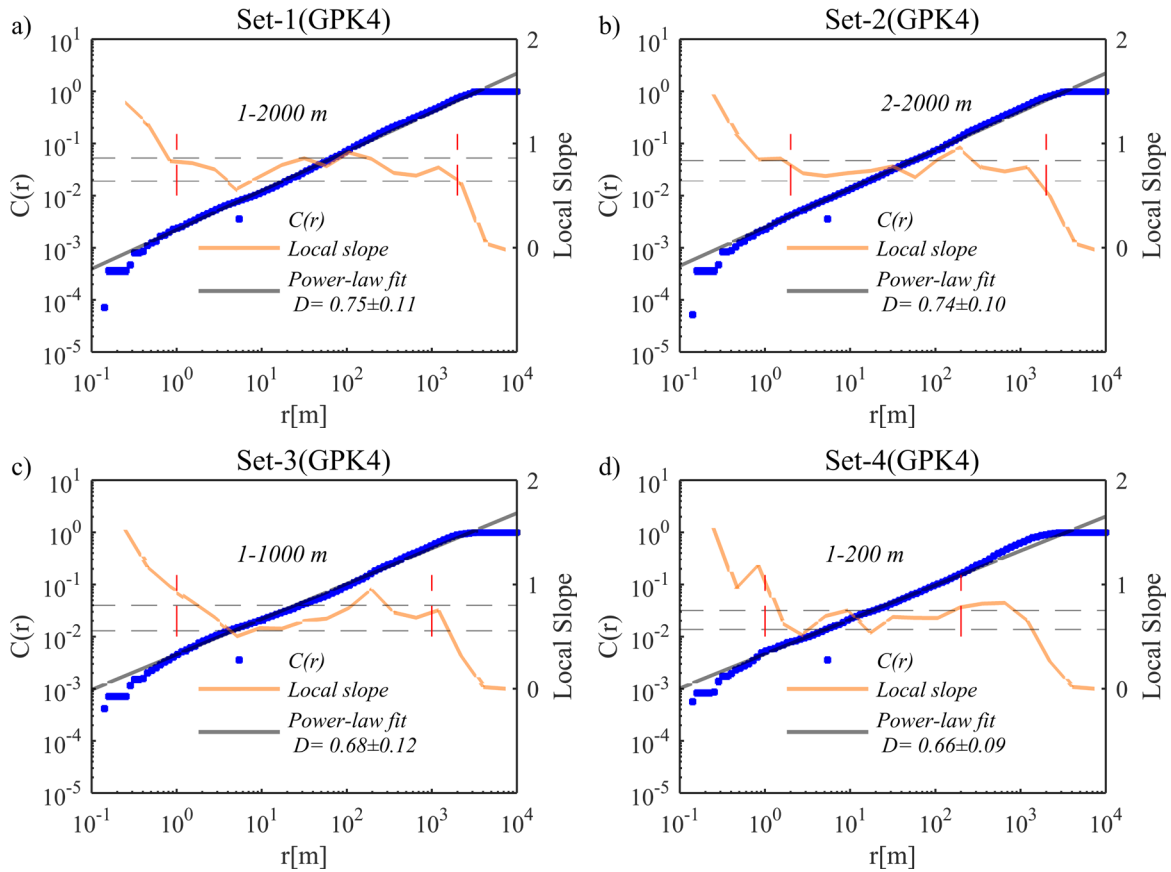


Figure 2-12. Same as Figure 2.10 but for the four fracture sets identified in the GPK4 well at the Soultz geothermal site: (a) set 1, (b) set 2, (c) set 3, (d) set 4.

### 2.3.2.3 1D spatial distribution of the entire fracture dataset

The correlation and slope functions of all fractures in the Basel-1, GPK3 and GPK4 datasets are shown in Figure 2-13a-c respectively. No consideration is given to the orientation of the fractures. For Basel-1, the log-log slope shows a constant value for two orders of magnitude, and for GPK3 and GPK4 for three orders of magnitude. The estimated fractal dimensions for the three holes are very close to each other, being 0.86, 0.88 and 0.87 for Basel-1, GPK3 and GPK4 respectively, and the associated errors (i.e. standard deviation of the local slope within the fractal range) over the fitting range 2-500 m is less than 0.06 in all cases.

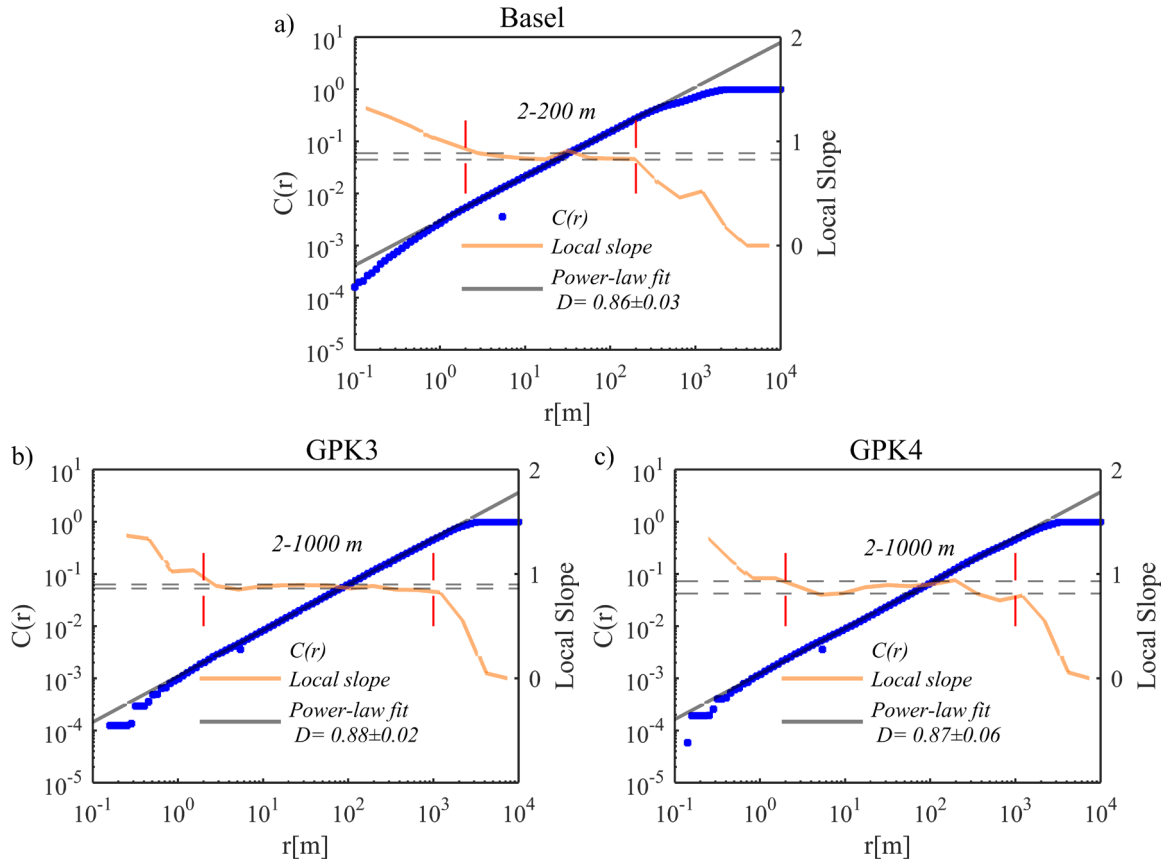


Figure 2-13. Correlation and log-log slope functions derived from all fractures (grouped into one dataset regardless of their orientation) intersecting (a) the Basel-1 well, (b) the GPK3 well (c) the GPK4 well.

#### 2.4 Minimum number of fractures required for a robust estimation of $D_{1D}$

Before applying our methodology to derive the depth profile of the fractal dimension ( $D_{1D}$ ) of fracture distributions in deep boreholes, we need to clarify the conditions under which  $D_{1D}$ , can be estimated robustly. Pursuant to this, we perform a sensitivity study to clarify the effect of the number of fractures on the computation of the correlation dimension of 1D scanlines in synthetic networks. We consider here two aspects of the uncertainty in the estimation of the correlation dimension: 1) the stability of the local slope of the two point correlation function that we estimate with the standard deviation of the local slope within the fractal range and 2) the representativity of the mean local slope of the two point correlation function obtained from a sample with a limited number of fractures. To perform this sensitivity study, we first generated a 2D fracture network with the parameters  $a_{2D} = 1.5$ ,  $D_{2D} = 1.5$ ,  $L = 500$  m and  $l_{min} = 1$ , and placed a scan line parallel to the y-axis at  $X = -178$  m. We chose these parameters, because the relatively low fractal dimension generates clustered fractured data that are less favorable for the estimation of the correlation dimension. Using this “worst case”, we ensure that the results

of our sensitivity study are of general applicability. In addition, the application of the two-point correlation function of equation 2 to all pairs of fracture intersection points along the scanline (328 fracture in total intersect the scanline) gave a correlation dimension  $D_{1D}$  of  $0.87 \pm 0.1$ , a value similar to the ones measured in Basel and Soultz and thus this example is representative of our specific application. The  $\pm 0.1$  is the standard deviation of the local slope within the fractal range and captures the stability of the local slope of the two point correlation function. Then, a variable-length window containing a prescribed number of fractures was progressively moved along the scanline with a 10-fracture offset, and the value of  $D_{1D}$  computed for each window by performing linear regression to the log-log plot of the correlation function between 5 and 50 m. The procedure was applied to windows containing upwards of 5 fractures until the total number of 328 fractures intersected was reached. The resulting values of  $D_{1D}$  are plotted as a function of the number of fractures in each window in the scatter plot of Figure 2-14a. Evidently, the scatter in the values decreases at the number of fractures in the window increases. The red lines denote the median and upper and lower quartiles of the statistical distribution of  $D_{1D}$  values obtained for each fracture number window size. Interquartile interval reasonably centered on the expected value of 0.87 is already well defined for a number of fracture as low as 30. However, the range is large ( $\pm 0.09$ ) for such low number of fractures. This range diminishes with increasing number of fractures and is down to  $\pm 0.03$  for 200 fractures, but is not perfectly centered on the expected value of 0.87 which indicates a tendency to overestimate the correlation dimension.

The stability of the local slope of the correlation function is evaluated by computing the standard deviation of the local slope over the fractal range for a subset of the test case with variable amount of fractures. This results are presented on Figure 2-14b. The standard deviation is high for small fracture and reaches a slowly decreasing value of  $\pm 0.1$  for 100 fractures or more.

Although the minimum number of fractures required to obtain a robust estimate of the fractal dimension of fracture patterns varies on different scanlines, a reasonably stable estimate is obtained for 200 or more fractures. With this number of fractures, the uncertainty comes primarily from the variability of the local slope. Thus, we adopt 200 as the minimum number fractures needed to estimate  $D_{1D}$  in the line sampling and we will use the standard deviation of the local slope over the fractal range as an indicator of the uncertainty of the estimate.

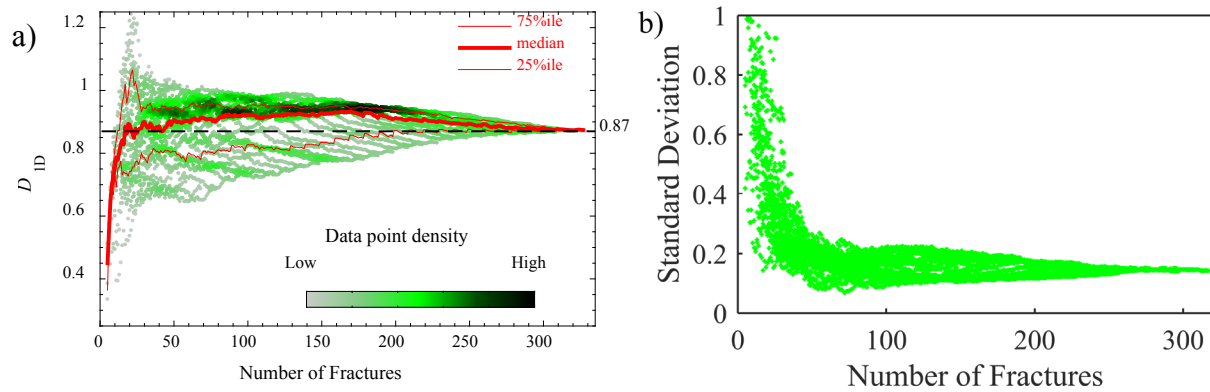


Figure 2-14. (a) Scatter plot of  $D_{ID}$  values obtained by stepping (variable-length) windows that contain a given numbers of fractures with an offset of 10 fracture along a scanline at  $X = -178$ . The given number of fractures ranged from 5 to the total fracture number in steps of 1. The red lines denote the median and upper and lower quartiles of the statistical distribution of  $D_{ID}$  values obtained for each fracture number. (b) Standard deviation of the local slope over the fractal range associated with the estimation of the  $D_{ID}$  values for variable number of fracture included in the sample.

## 2.5 Fractal profile of spatial distribution versus depth

The geometrical characteristics of fracture networks—influences the hydraulic response of the system (Bonneau et al. 2016; Darcel et al. 2003c). Knowledge of the spatial distribution of the fractures along deep boreholes helps us to understand the structure of discontinuities in the crust. Ledésert et al. (1993) analyzed the fracture profiles in core from EPS1 and logs from GPK1 for the shallow (i.e. 1400-2200 m) reservoir at the Soultz-sous-Forêts site. They applied Cantor’s Dust method (box-counting) to compute the fractal dimension of fracture spacing in windows taken along the boreholes and found evidence that fractal dimension increased with depth, which they proposed was related to the lithostatic pressure gradient. In contrast to Ledésert et al. (1993), here we apply the two-point correlation function method to successive depth intervals taken along the Basel and Soultz boreholes to assess whether any systematic variation in fractal dimension of fracture spacing is resolved. In each interval, two-point correlation functions were computed for 200 points uniformly spread logarithmically between 0.1 and 1000 m (i.e. 50 points per decade). The local slopes of the correlation functions were calculated by performing a linear fit over a 10-point wide window moved along the data with 75% overlap so as to give 20 slope values for every order of magnitude. Each log-log slope function was inspected to identify the range over which its value was reasonably constant, and a linear regression with a horizontal line performed to identify the correlation dimension and

the standard deviation. In all cases, the plateau was seen to span at least 1.5 orders of magnitude in  $r$ .

Based upon the previous section, the intervals over which  $D_{1D}$  estimates were chosen to include at least 200 fractures. For the Basel-1 dataset, 300 fractures were included in each window, and the latter moved along the profile in steps of 100 fractures, giving a 200 fracture overlap on successive windows so as to increase the number of  $D_{1D}$  determinations. A complication of the Basel-1 dataset is posed by the higher fracture density seen at the top of the profile between 2600 and 3100 m, as shown in Figure 2-15a, which contains 600 out of the total of 1164 fractures intersected by the well. This interval has been assumed to be the paleo-weathered surface and be exhumed close to the Earth's surface before the deposition of sedimentary rocks. Because of the large number of fractures with shorter spacing, the plateau of the log-log slope function that denotes fractal scaling began for  $r$  as small as  $0.1m$  for intervals above 3100 m, whereas the start point was  $\sim 1m$  for intervals below. The profile of  $D_{1D}$  estimates are shown in Figure 2-15b together with the standard error from the linear regression. Evidently, no systematic change in  $D_{1D}$  values is resolved, although the standard deviation estimates are large.

Similar analyses were performed on the GPK3 and GPK4 fracture datasets from Soultz-sous-Forêts using moving windows containing 500 fractures in steps of 100 fractures (i.e. 400 overlaps), and the resulting profiles of  $D_{1D}$  are shown in Figure 2-16b and Figure 2-16d respectively. The fracture density profiles of the wells shown in Figure 2-16a and Figure 2-16c, are more uniform than the Basel-1 case, and the plateau denoting the start of fractal scaling begins at a  $r$  value of  $\sim 1m$ . As in Basel-1, the lack of systematic depth variation in  $D_{1D}$  is evident at the 1 sigma level, although the uncertainties are large.

## 2.6 Discussion

The generation of discrete fracture network models conditioned by available observations from boreholes or outcrop is required in practically all subsurface rock mass characterization programs (e.g. Watanabe and Takahashi 1993). The approach investigated here makes the assumption that fracture networks can be considered as fractal objects. Fractal fracture networks require the values of scaling parameters that control the position and length of the fractures that form the network to be specified. The dual power law mathematical model proposed by Davy et al. (1990a) is a convenient way of describing the fracture network. The model contains two scaling parameters: the correlation dimension  $D$ , which controls the position of fracture centers, and the length exponent  $a$ , which controls the fracture length distribution. One-dimensional,

two-dimensional and three-dimensional synthetic fracture dataset honoring this model can be generated using the multiplicative cascade process. This model forms the basis of our analyses.

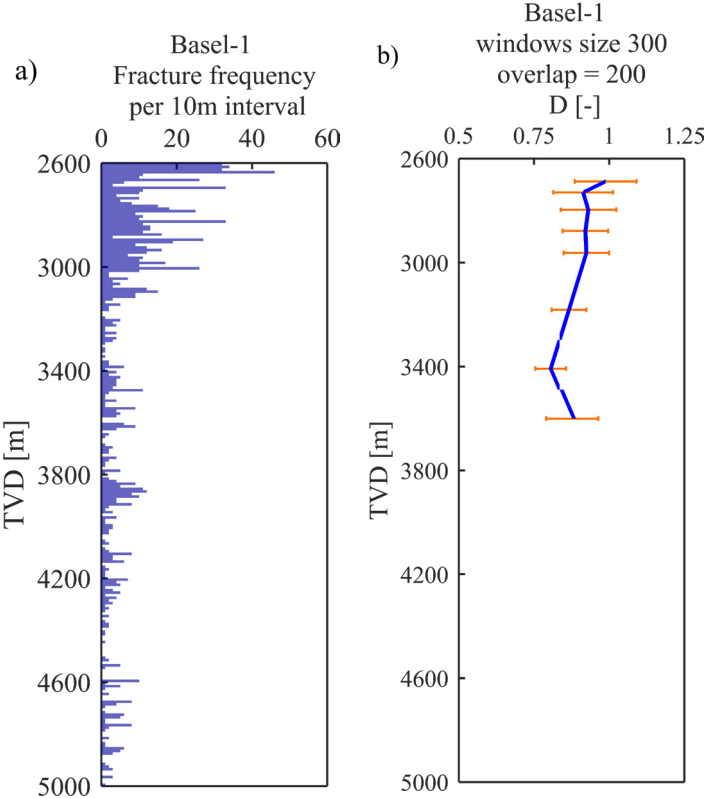


Figure 2-15. (a) Profile of the density of fractures in the Basel-1 well per 10m interval. (b) Variation of correlation dimension in moving windows containing 300 fractures with 200 overlaps in Basel-1. The error bars represent the standard deviation of the local slope within the fractal range.

The scaling inherent in fractal fracture networks is quantified by scaling of fractures in deep boreholes is largely dependent on the technique applied to obtain the scaling exponents (i.e. fractal dimensions). Many studies reported different values as the fractal dimension of fracture patterns on deep boreholes single scanlines without an agreement on the true fractal dimension value. For 2D and 3D fracture networks, the fractal dimensions obtained from applying different measurement methods represent the scaling properties of different attributes of the fracture networks. For example, box-dimension is a measure of the space filling characteristics of the fractures (which inherently accounts for the length and center-to-center separation of the fractures) and correlation dimension reveals the clustering of fracture centers. (Bour et al. 2002) applied the box-counting technique to an outcrop in Norway and fractal behavior over a limited range of scales, whereas the two-point correlation function method indicated fractal behavior over a much larger range of scales. The fractal dimensions obtained from the two methods were different. In contrast to 2D and 3D fracture networks, the distribution of fractures along 1D

scanlines or boreholes depends only on the separation of fracture intersection points. For this simple case of points along a line, it might be thought that if the distribution is indeed fractal, then the same fractal dimension would be obtained regardless of the technique used to estimate it. However, our experiments with synthetic 1D fracture-spacing data of known fractal dimension showed that the two-point correlation method was the only technique that yielded stable and correct estimates for the fractal dimension of the series, as given by the correlation dimension. The experiments showed that when including 200 or more fracture in an analysis, the correlation dimension can be evaluated accurately. The box-counting technique and power-law distribution of spacing methods did not deliver reliable estimates of the fractal dimension.

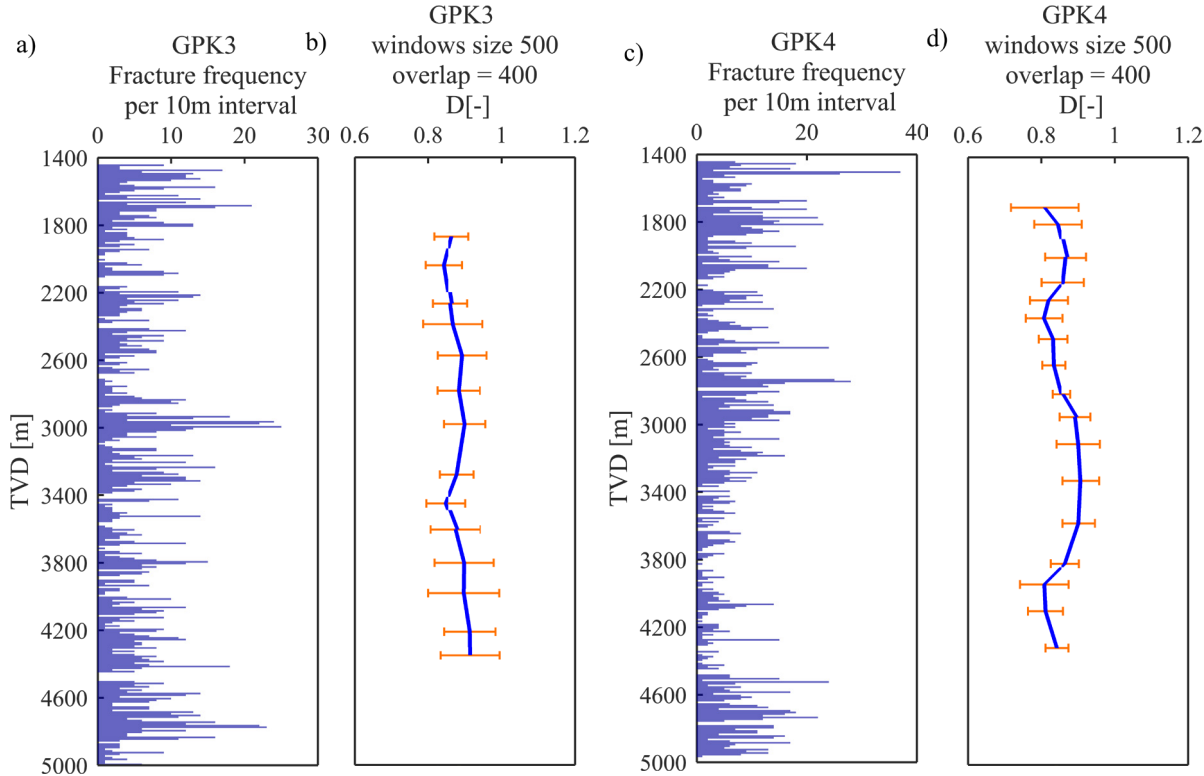


Figure 2-16. (a) Profile of the density of fracture in the GPK3 well per 10m interval. (b) Variation of correlation dimension in moving windows containing 500 fractures with 400 overlaps in GPK3. (c) Profile of the density of fractures in the GPK4 well per 10m interval. (d) Variation of correlation dimension in moving windows containing 500 fractures with 400 overlaps in GPK4. The error bars represent the standard deviation of the local slope within the fractal range.

The computation of one dimensional correlation dimension for the fracture data set of one deep borehole in Basel-1 and two deep boreholes in Soultz-sous-Forêts (GPK3 and GPK4) leads to very similar correlation dimension from 0.86 to 0.88 when considering all fracture orientation together. This scaling parameter is valid over more than two order of magnitudes, i.e. typically in the range 2 to 1000 m. This covers the entire range that one can reasonably expect from

borehole data in the basement along length of 2.5 km (Basel) to 3.5km (Soultz) before finite size effects kicks in. This is a strong evidence that the fracture networks investigated follow a fractal organization. When sorting fractures in sets with similar orientations, the correlation dimension slightly diminishes to values ranging from 0.65 to 0.75 and the range of validity of the scaling relation span more than two orders of magnitude similarly with the analyses performed on all fractures.

No clear trend with depth of correlation dimension are visible in our data. In that regard the data from the south boreholes GPK3 and GPK4 are of particular interest since in the upper kilometer of the granite section the distance between the boreholes is less than 30 m and they sample essentially the same rock mass. The inter-well distance increases up to 700 m toward the bottom of the holes. Thus, the constancy in correlation dimension in these borehole indicate not only a depth homogeneity of the fracturing fractal characteristics, but although a lateral homogeneity.

The data from Basel-1 allow exploring a different aspect since a strong change of fracturing intensity is present in this data set above and below 3km. This change in fracturing intensity is interpreted as reflecting fracturing overprinting due to stress relaxation prior to Triassic times when the top of the crystalline basement was at the surface. The correlation dimension is higher than 0.9 above 3km and less than 0.9 below 3 km, although the one standard deviation confidence range overlaps over the entire depth range and this difference may not be significant. Thus, fracturing intensity has in this case, if any, a very limited impact on correlation dimension.

The physical interpretation of the correlation dimension  $D_{1D}$  in terms of the organization of the fracture network is not trivial (Davy et al. 2010). Uniformly spaced fracture or spacing following a uniform random distributions (Poisson's process) will have a correlation dimension of 1.0. Smaller values of  $D_{1D}$  will imply some clustering of the fractures. Our values for  $D_{1D}$  suggest some clustering of the fractures, but, not a very strong one. Power law fit of cumulative spacing distribution for various fracture sets in GPK3 and GPK4 indicate fractal dimensions of 0.63 to 1.0 (Valley 2007). This is similar to our findings, but the stability of the local slope is not satisfying. The degree of clustering and the fractal dimension is also interpreted by some authors as an indication of the “saturation” of the fracture network, i.e. if fractures location is dense enough to force fracture interactions during the growth process (Davy et al. 2010; Scholz 2002). More saturated system will develop more uniform fracturing leading to higher fractal dimensions. This would indicate that our fracture network in Soultz and Basel are close to be



saturated. This would also explain why adding fractures due to decompression in the upper 400 m of the Basel data does not lead to significant increase in fractal dimension since the fracture network to start with is already saturated.

An important question concerns the constraints that an observed distribution of fracture intersection points in a borehole places on the scaling of the fracture network within the rock mass penetrated by the borehole. Clearly, the 1D spacing distribution reflects to some degree the characteristics of the 3D network (i.e. the parameters controlling fracture location ( $D_{3D}$ ) and fracture length ( $a_{3D}$ ) in the dual power law model), and commonly shows a 1D fractal nature characterized by a fractal dimension,  $D_{1D}$ . Darcel et al. (2003b) derived stereological relationships for fractal DFNs which relate  $D_{1D}$  for a scanline through the DFN to the scaling parameters of fracture patterns on 2D surfaces within the DFN (the correlation dimension of fracture centers,  $D_{2D}$ , and the length exponent  $a_{2D}$ ), and also to the 3D scaling parameters ( $D_{3D}$  and  $a_{3D}$ ). Applying the relations to synthetic data, they found that the 3D spatial distribution of fractures could not be constrained from the lower-dimension scaling parameters, except when the length exponent was known. However, our stereological analysis shows that even when the fracture length exponent is known, it is not possible to deduce 3D scaling parameters from 1D data. The problem is strongly underdetermined and leads to non-unique solutions. Additional information must be included in order to circumvent these limitations. This can be done in the case of geothermal reservoir development by integrating the spatial distribution of induced seismicity (Afshari Moein et al. 2018), although this information becomes available only after that reservoir stimulation has been performed. Another potential source of information stems from the scaling of stress orientation variations that are revealed by extensive wellbore failure that is commonly observed in deep boreholes (Moein et al., in prep.).

## 2.7 Conclusions

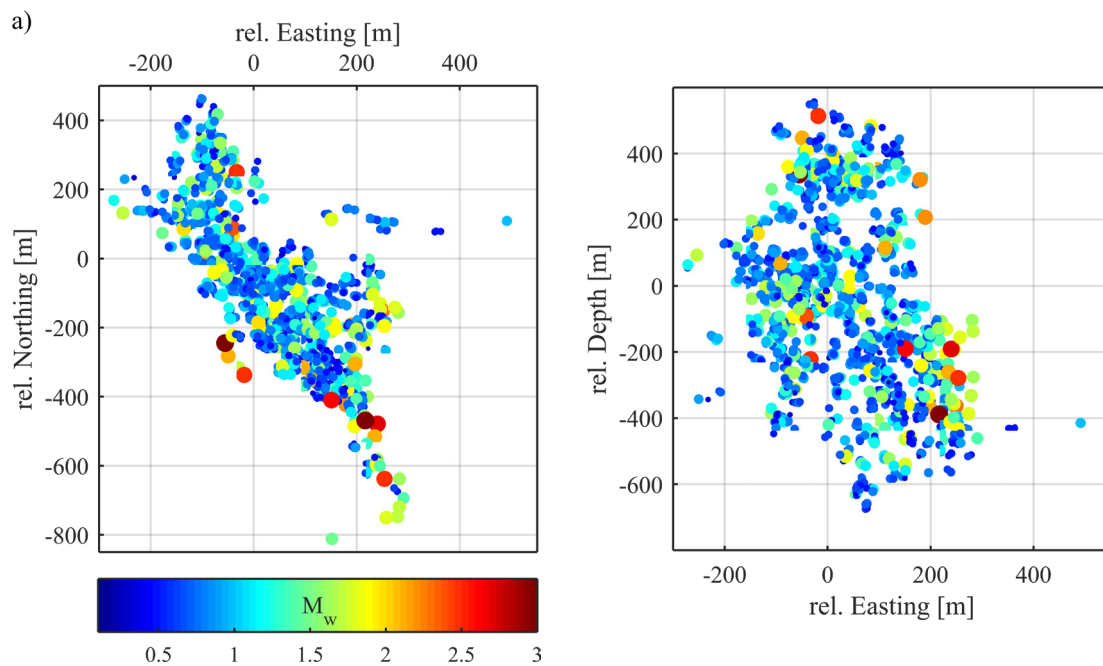
Fractal fracture networks that respected the dual power law model of Davy et al. (1990b) were generated using a multiplicative cascade process. Two independent scaling parameters inherent in the model relate to the distribution of distances between fracture centers (correlation dimension,  $D$ ), and the distribution of fracture lengths (length exponent,  $a$ ). Analyses of 1D synthetic fracture distributions along lines generated with the model show that correlation dimension obtained from the 2-point correlation method provides the most stable and reliable estimate of the fractal dimension of fractures on 1D scanlines or boreholes. The spatial distributions of fractures along three deep boreholes in crystalline rock at Basel and Soultz-sous-Forêts was found to be fractal over more than two orders of magnitude in scale, and in all

cases the fractal dimensions lay in the range 0.86-0.88. Fracture sets of common orientation within the wells were also fractal over more than two orders of magnitude, although the fractal dimension ranged between 0.65-0.75. This constitutes strong evidence that fracturing in rock masses penetrated by the wells follows a fractal organization. No systematic variation of fractal dimension with depth was resolved in any of the boreholes at the one standard deviation level of uncertainty.

Analyses performed on synthetic fractal fracture networks show that it is not possible to estimate the 2D and 3D fractal scaling parameters of correlation dimension or length exponent from the 1D correlation dimension of fracturing spacing from scanlines through the network. This was found to be true even if the length exponent of the fracture distribution was known a-priori. The stereological problem of constraining scaling in 2D and 3D from 1D observations is too underdetermined and requires information in addition to the length exponent.

### 3 Maximum magnitude forecast in hydraulic stimulation based on clustering and size distribution of early microseismicity

---



Reproduced from: Afshari Moein, M.J., Tormann T., Valley B., Wiemer S., *Maximum magnitude forecast in hydraulic stimulation based on clustering and size distribution of early microseismicity*, Geophysical Research Letters, 45. <https://doi.org/10.1029/2018GL077609>.



## **Abstract**

We interpreted the spatial clustering and size distribution of induced microseismicity observed during the stimulation of an Enhanced Geothermal System beneath Basel by comparison with scale invariant synthetic data derived from discrete fracture network models. We evaluated microseismic specific influential factors including the effect of hypocentral location uncertainties, existence of a fractured zone and repeating events on the observed spatial organization. Using a dual power-law model originally developed in the context of discrete fracture network modeling, we developed theoretically the relationships amongst spatial clustering and magnitude distributions. We applied this model to the Basel data set and showed that the spatial clustering characteristics presented stationary properties during the hydraulic stimulation. Based on this observation, we proposed a statistical seismicity model calibrated on the scaling of early stimulation spatial patterns which is capable of forecasting the maximum magnitude of induced events with increasing injection time and stimulated volume.

### **3.1 Introduction**

Developing Enhanced Geothermal Systems (EGS) requires massive fluid injections (hydraulic stimulation) to enhance the permeability in order to achieve higher flow rates and exploit the stored heat from elevated temperatures in the earth's crust. Since the stress conditions of corresponding depths can be critical (Townend and Zoback 2000), the pressurized fluid injections induce microseismic activity. The associated microseismicity can be large enough to be felt by public and may lead to suspension of EGS developments such as Saint-Gallen and Basel geothermal projects in Switzerland (Edwards et al. 2015; Häring et al. 2008). The underlying mechanisms of permeability creation during a hydraulic stimulation experiment is not fully understood and still debated. Nevertheless, shearing on rough surfaces due to the increase of pore pressure is expected to enhance the hydraulic conductivity (Evans et al. 2005a). Induced microseismicity is a result of the interaction between pre-existing fracture network and fluid pressure induced changes (Evans et al. 2005b). To reliably assess the rock mass response to fluid injection, the permeability creation potential and the seismic hazard and risk of any development scenarios, the 3D structure of the underlying fracture network should be characterized. Borehole image logs provide the location and orientation of fractures on borehole wall, which are not sufficient to create a 3D structural model of a reservoir in a depth of 2-5 km (Valley and Evans 2015a). The major unknown parameter of the existing network is fracture length distribution, which has a large impact on the fracture network connectivity and hydraulic characteristics of rock mass. Induced microseismicity provides valuable information about the

possible failure planes in the reservoir volume and this information can be possibly used to guide the stochastic realizations known as discrete fracture networks (DFN).

Induced microearthquakes reveal scale invariant spatial patterns (Sahimi et al. 1993; Tafti et al. 2013) and the magnitude frequency exhibits power-law distributions (Bachmann et al. 2012; Gutenberg and Richter 1954). We adopt the working hypothesis that the scaling of induced events is reflecting some aspects of the geometry of underlying fracture network. On the other hand, the fracture networks also reveal scale invariant characteristics (Bour et al. 2002; Davy et al. 1990a; de Dreuzy et al. 2001; de Dreuzy et al. 2002; Lei et al. 2015; Odling et al. 1999). Self-similar fracture patterns may originate from complex self-organized critical dynamics, which relate the large scale statistics to smaller ones (Allegre et al. 1982; Bak et al. 1988; Sornette 2006; Sornette et al. 1990). Furthermore, the stress interactions in fractures growth process may also result in power-law length distributions (Davy et al. 2010; Spyropoulos et al. 2002).

The interaction between fluid pressure, in-situ stress conditions and fracture network results in microseismicity, which is not completely understood. Potential similarities between the scaling properties of fracture networks and induced microseismicity may improve the statistical seismicity models. Current statistical models, typically neglect the scaling properties of microseismic patterns and potential correlations between location and magnitude of induced events. Moreover, these statistical models are mostly unable to explain the effect of geological features such as damage zones and geophysical features such as location uncertainties and repeating events on the scaling properties of induced patterns. Proper understanding of the scaling characteristics of microseismicity patterns may introduce new features into the statistical models and improve the maximum magnitude forecast during hydraulic stimulation operations.

We implement fractal geometry to characterize the spatial distribution of microseismicity in the Basel geothermal site and analyze the scaling properties by simulating the previously mentioned microseismic specific feature. Such analyses leads to propose a statistical model that presents the spatial clustering and rupture size distribution of induced events. The parameters of this model are calibrated by early time patterns (learning phase) and forecast the seismic risk during the continued injection and shut-in phase. We test this model in the Basel geothermal site and conclude with an outlook for future applications.

## 3.2 Microseismicity in Basel geothermal site

Injecting water at high pressure into the open hole section below 4629m of Basel geothermal system induced 14,578 recorded seismic events between December 2, 2006 and March 31, 2007, 3460 of them were located (Dyer et al. 2010; Häring et al. 2008). Kraft and Deichmann (2014) performed a waveform similarity analysis and relocated the initial catalogue to 1980 events and reduced the uncertainty of hypocentral locations. We use this catalogue in this study. Figure 3-1a displays the spatial scattering of microearthquake hypocenters from top and side view and Figure 3-1b shows the corresponding cumulative frequency size distribution with the estimate of b-value using the maximum likelihood fit (Aki 1965).

### 3.2.1 Spatial distribution

Two-point correlation function has been widely used to characterize the spatial clustering of fractures and earthquake hypocenters (Bour et al. 2002; Hirata et al. 1987). A fractal dimension ( $D$ ) is computed by fitting a power-law to correlation function according to equation 3.1,

$$C(r) = \frac{2}{N(N-1)} N_p(r) \sim r^D \quad (3.1)$$

where  $N$  is the total number of events and  $N_p$  is the number of pairs of events whose hypocentral distance is less than  $r$  (Hentschel and Procaccia 1983b). Figure 3-1c represents the correlation function of the relocated induced events. The corresponding local slope is close to two between 50–100m distance, then decreases between 2–50m and larger than 100m. Therefore, such a deviation from pure scaling law should be explained.

### 3.2.2 Rupture radius distribution

Most seismic events in hydraulic stimulation represent failures on existing fracture planes and the reported magnitude depends on the radius of the rupture plane and the stress drop. If we assume every event represents a rupture plane, a rupture radius can be assigned by equation 3.2. The radius of a circular failure plane ( $R$ ) in space is related to stress drop ( $\Delta\sigma$ ) and seismic moment ( $M_0$ ) through equation 3.2 (Eshelby 1957),

$$R^3 = \frac{7M_0}{16\Delta\sigma} \quad (3.2)$$

Goertz-Allmann et al. (2011) determined the stress drops from P-wave signals of 1000 microearthquakes in Basel and a large portion of the events showed a constant stress drop of 2.26 MPa (the average value) with a variation between 0.1-10 MPa. If we simply assume a

constant stress drop on every seismic event, the rupture radius scaling exponent  $a_r$  may be computed. Figure 3-1d shows the rupture size distribution of induced events for three different stress drop assumptions (0.1, 2.26 and 10 MPa) follows a power-law, whose slope  $a_r$  is independent from the average stress drop on each event and is related to b-value through equation 3.3 (Shapiro et al. 2013).

$$a_r = 2b + 1 \quad (3.3)$$

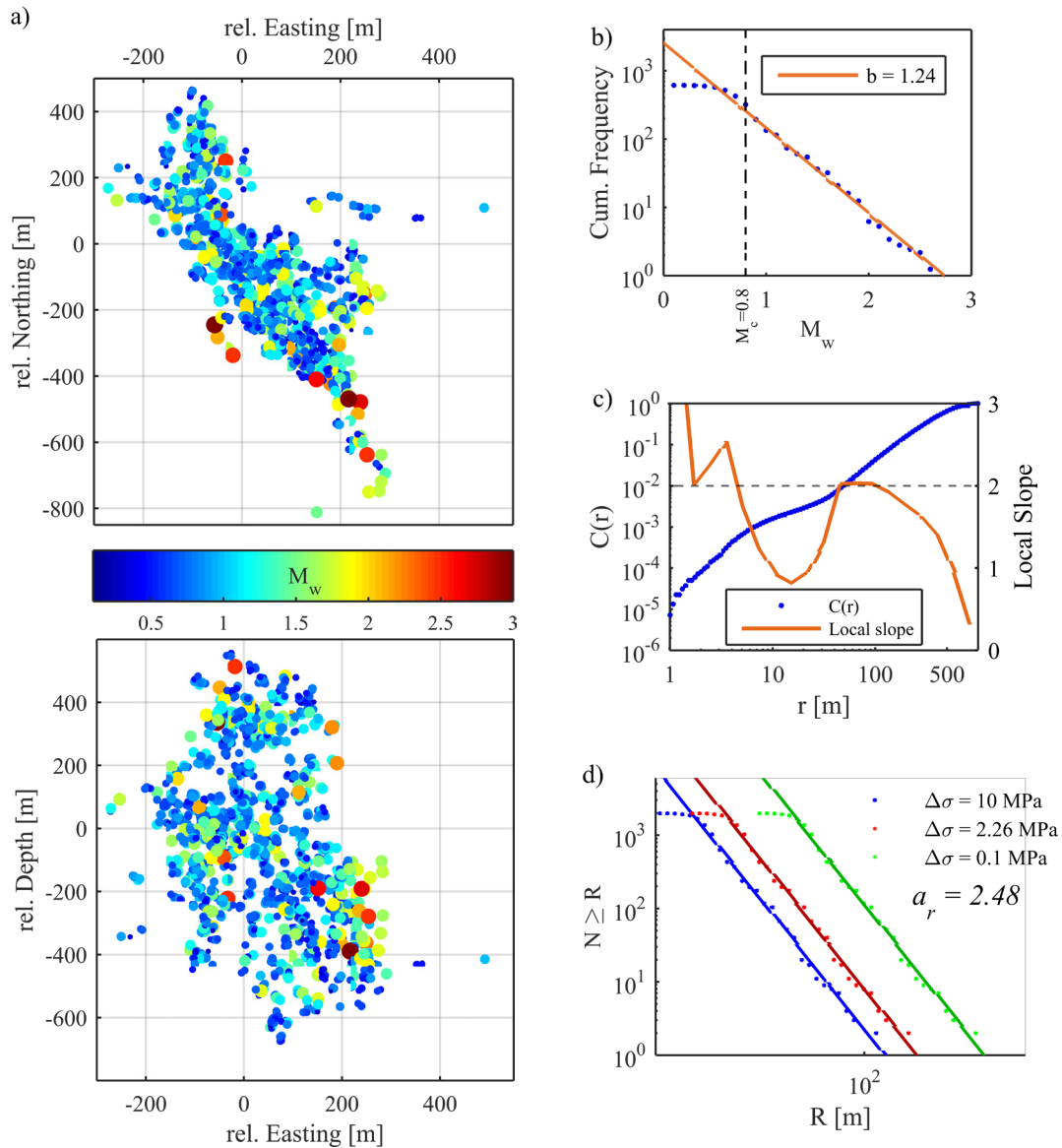


Figure 3-1. (a) Top and side view of the spatial scattering of microearthquake hypocenters relative to the casing shoe in Basel geothermal system (Kraft and Deichmann 2014). (b) Frequency size distribution of microearthquakes and estimates of b-value using maximum likelihood estimates. (c) Correlation function and its local slope. (d) Complementary cumulative rupture radius distribution ( $R$ ) for different stress drops.



### 3.3 Synthetic fracture network model

The evidence on clustering and power-law size distribution of rupture patterns motivates generating synthetic rupture patterns with the same statistical characteristics. Thus, we utilized the concepts developed in the framework of discrete fracture network modeling and adopted the following statistical model to generate fractal fracture patterns from Davy et al. (1990a),

$$n(l, L)dl = \alpha L^D l^{-a_f} dl \quad (3.4)$$

where,  $n(l, L)dl$  is the number of fractures whose length is in the range  $[l, l + dl]$  and whose center belongs to a volume in three dimensions of size  $L^3$  [m]<sup>3</sup>,  $\alpha$  [m] <sup>$a_f - D - 1$</sup>  is a normalization constant and affects the fracture density,  $D$  is the correlation dimension of fracture centers and  $a_f$  is the fracture length exponent. This model, also known as dual-power law model, has been widely used to study different aspects of fractured media (Darcel et al. 2003c; Harthong et al. 2012; Kim 2007; Verscheure et al. 2012). Here, the size of a fracture plane is defined as the radius of a circular disk. The motivation to choose such a fracture model is that natural fractures exhibit self-similar spatial patterns in different scales (Chilès 1988; Davy 1993). In addition, power-law distribution is the only scale-invariant statistical distribution and has been used to describe the fracture attributes in different scales. Different fracture attributes such as trace length, spacing, RQD (Rock Quality Designation, Deere and Deere (1988)), aperture, surface roughness etc. show also self-similar patterns (Barton and Zoback 1992; Boadu and Long 1994; Bonnet et al. 2001; Power and Tullis 1991). Dual power-law model enables to generate fractal spatial organization as well as power-law length distribution of fractures in two and three dimensions. We developed this model to generate random network realizations in MATLAB and verified the power-law spatial and size distribution of fractal DFNs, which is presented in the Appendix B. In addition, the relation between position and size distribution of fractures is verified in synthetic fracture networks. The details of the generation methodology are available in the above-mentioned references.

The fractal analysis of microseismicity patterns do not present a clear scaling (Figure 3-1c) and requires further analysis. Here, we analyze the influence of three factors that complicate the extraction of geometrical characteristics of fracture network from seismicity data. The factors that we include in this analysis are: 1) uncertainty associated with location of microearthquake hypocenters, 2) existence of a fractured zone and 3) repeating events on same structures. For this analysis, we generated a 3D DFN with the following input parameters  $D=2.7$ ,  $a=3.5$ ,  $\alpha=0.1$ ,

$l_{\min}=10$  m in a cubic domain with side length of  $L=500$  m. We need to mention that no boundary treatment is done i.e. some fractures might extend outside of the generation domain.

### 3.3.1 Uncertainty of hypocentral locations

Earthquake locations are estimated by travel time inversion of the recorded P-wave and S-wave arrivals. The computed hypocenters are associated with uncertainties because of unknown velocity structure of the earth and arrival time observation errors. The confidence region of earthquake hypocenters are ellipsoidal and normally distributed (Husen 2010). The variance of the normally distributed earthquake hypocenters can be determined by a principal component analysis of the scatter clouds obtained from random realizations of hypocenters locations considering uncertainties on the seismic data and velocity model. The 68% confidence level of principal axes of ellipsoids in Basel geothermal system have a mean length of 74 m, 48 m and 32 m which, are taken from a principal component analysis of the scatter clouds (Kraft and Deichmann 2014).

To study the influence of such an uncertainty, we insert a random noise on fracture center coordinates (XYZ) from a normal distribution in the 3D fracture network of Figure 3-2a. If the principal axes of ellipsoids are aligned with XYZ coordinates, the variance of the noise are 74 m, 48 m and 32 m in the direction of each coordinate (the maximum uncertainty in 3D is 93m). Figure 3-2b shows the correlation function and its local slope of a random realization with predefined noise on fracture center locations compared to initial network. The correlation dimension tends to increase (approach to 3), if the hypocentral location uncertainty is included in the rupture models. A sensitivity analysis on the effect of uncertainty in 3D is presented in Appendix B.

### 3.3.2 Existence of a fractured zone

Borehole observations and induced microseismicity in deep crystalline rocks confirm the existence of fractured zones, which provide the main fluid path into the reservoir (Deichmann et al. 2014; Evans et al. 2005a). Fractured zones are intervals of very high-density fractures, where the spatial distribution of fractures can be assumed to be random in a limited width. From the geological perspective, fractured zones are equivalent to damage zones flanking a fault core with a very high permeability and introducing a preferential fluid flow path (Bense et al. 2013). To simulate a fractured zone, we generate a simple synthetic horizontal fractured zone by populating uniformly distributed fracture centers with a uniform radius between 0 and 50 m in a slice of 40 m width (Figure 3-2c). Since the focus is on the spatial distribution of fracture

centers, the radius distribution does not change the analysis. A fractured zone with 1000 fracture centers is generated in the domain similar to network of Figure 3-2a and the corresponding correlation function of the 3D spatial distribution is displayed in Figure 3-2d. The correlation dimension of such a fractured zone equals to 2.

The fractured zones may be embedded in a 3D network. Therefore, if we add a fractured zone into the network of Figure 3-2a, the spatial distribution of the network may be altered. Figure 3-2e shows the correlation function of the resulting network and its local slope, which is slightly less than 2.7. A sensitivity analysis on the width of fractured zone and its influence on the resulting spatial organization is presented in Appendix B.

The fractured zones may be embedded in a 3D network. Therefore, if we add a fractured zone into the network of Figure 3-2a, the spatial distribution of the network may be altered. Figure 3-2e shows the correlation function of the resulting network and its local slope, which is slightly less than 2.7.

### **3.3.3 Repeating events**

The source of every recorded micro-seismic event might not be unique and the rupture might occur on different points of a discontinuity plane. Repeating events are characterized by almost identical waveforms, which reflect very similar re-ruptures of the same structure but may have different magnitudes. Here, we analyze the influence of repeating events on the spatial organization of a synthetic fracture network. Therefore, we add random fracture centers representing the repeating events to the network of Figure 3-2a. We choose 10 random fractures from the initial network and add 10 fracture centers very close to them (entirely 100 random fracture centers represent the repeaters). The repeaters are selected randomly from a sphere with a radius of 4.3m, perturbed the randomly chosen fractures (i.e. the maximum offset of repeater coordinates from the chosen fracture center is 2.5m). The correlation function of the initial network with repeaters is displayed in Figure 3-2f and a sensitivity analysis on the number of repeating events is presented Appendix B). Introducing the repeaters into the rupture model results in a drop of the correlation dimension in distances between 2-100 m.

Here, we analyzed the impact of three main factors that may substantially deviate the scaling of microearthquake patterns from a pure power-law. However, other factors may influence the scaling properties of induced patterns. For instance, the orientation of discontinuities relative to the in-situ stress conditions may affect the spatial organization of slipping patches. Analyzing the impact of this factor requires physical modeling of the induced seismicity using thermo-hydromechanical simulations, which is beyond the scope of this paper.

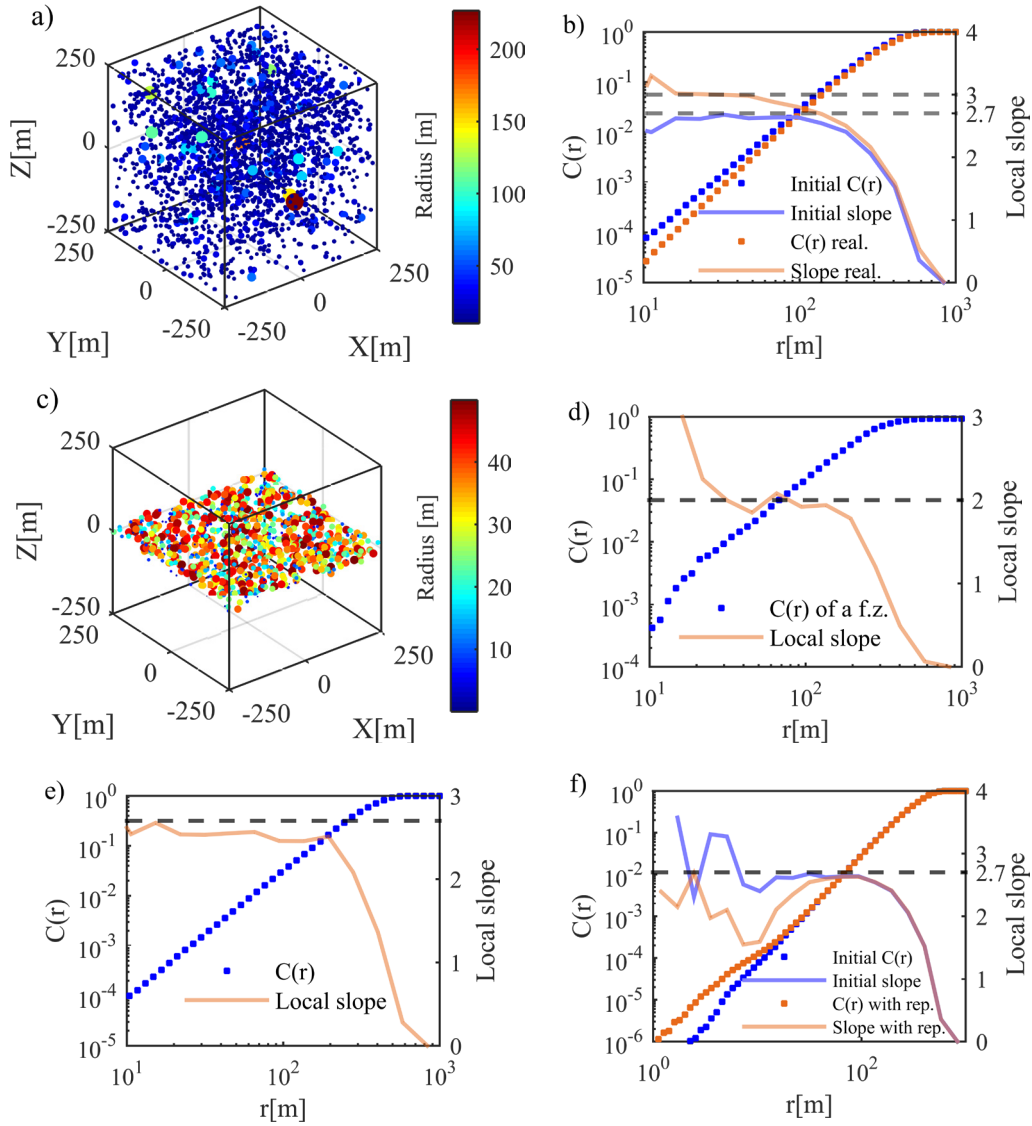


Figure 3-2. (a) A 3D random DFN with  $D = 2.7$ ,  $a = 3.5$  and  $\alpha = 0.1$ . (b) Effect of 93 m uncertainty in fracture center locations on the resulting spatial distribution of a random realization of the initial network. (c) 3D view of a 40 m width fractured zone. (d) Spatial organization of a fractured zone. (e) Spatial organization of the network merging two networks in a and c. (f) Effect of 100 repeaters in a maximum 5 m distance from 10 randomly selected fractures (10 repeaters belong to each fracture).

### 3.4 Geometrical forecast approach

In previous sections, we applied synthetic fracture networks to explain the spatial organization of induced events in Basel and described the impact of influential factors. In general, extracting the statistical properties of network geometry from induced microseismicity is difficult, because of the previously discussed factors. Nevertheless, similarities between the induced microseismicity and scale invariant fractal networks motivated us to propose a statistical model for geometry of rupture patterns. This model represents the clustering and size distribution of

induced seismicity by a dual power-law model, which is initially developed for fracture networks. This forecast approach is different from other statistical approaches such as the seismicity models presented by Shapiro et al. (2013) and McGarr (2014). The major progress in this model stems from the physical nature that originates from the scaling characteristics of fracture networks. These characteristics enable the model to clarify the effect of features that deviate the microseismicity patterns from pure scaling laws such as repeating events, hypocentral uncertainty and fractured zones. In a specific comparison to the model proposed by Shapiro et al. (2013), which deals with planar preferential path for the seismicity cloud, dual-power law is a universal model that can include any fractal dimensions between 2 and 3 (2 is a planar structure and 3 is uniformly distributed in space). For instance, the Geyser field (Tafti et al. 2013), in which the spatial distribution of induced events shows a fractal dimension of 2.57.

### 3.4.1 Methodology

This approach sets a dual-power law model for rupture patterns based on very early stimulation phase (learning period) and performs a predictive real-time seismic hazard analysis, so that future development of microseismicity can be anticipated. It computes the maximum rupture radius and the corresponding seismic magnitude (assuming a constant and conservative stress drop) with an increase in the perturbed reservoir volume. We define the *perturbed reservoir volume* as the smallest cubic volume which encompasses all the microearthquake hypocenters. This methodology is based on scale-invariant spatial distribution of seismic events and the power-law rupture radius distribution. In general, a simple dual power-law model can represent the rupture geometry patterns similar to equation 3.5;

$$n(R, L)dl = \alpha L^{D_r} R^{-a_r} dl \quad (3.5)$$

where, the seismic patterns are located in a cube of side length  $L$  with a correlation dimension of  $D_r$  and rupture size exponent of  $a_r$ . The initial parameters ( $a_r$ ,  $D_r$ ,  $\alpha$  and  $L$ ) of this equation are estimated from the learning phase patterns. We take the maximum offset of seismic events from the casing shoe plus the corresponding location uncertainty as the initial side length of the perturbed volume ( $L$ ) and set the approximate minimum rupture radius ( $R_{min}$ ) in the perturbed volume of the learning phase. Magnitude of completeness ( $M_c$ ) delivers  $R_{min}$  using equation 3.2. For a detailed analysis on how to compute the magnitude of completeness ( $M_c$ ), we refer to Mignan and Woessner (2012). Finally, the parameter  $\alpha$  may be estimated from equation 3.6.

$$N = \int_{R_{min}}^{\infty} n(R, L)dl = \frac{\alpha}{a_r - 1} L^{D_r} R_{min}^{-(a_r-1)} \quad (3.6)$$

If the injection continues to sweep a larger volume and increase the perturbed volume with a side length of  $L'$  ( $L' > L$ ), this model can compute the rupture radius distribution and the corresponding size magnitude by equation 3.7.

$$n(R, L)dl = \alpha(L')^{D_r} R^{-a_r} dl \quad (3.7)$$

The estimated rupture radius exponent ( $a_r$ ) is independent from the average stress drop on rupture planes, whereas the minimum and maximum rupture radius depends on the assumed stress drop (Figure 3-1d). The maximum expected ( $M_w$ ) should be computed based on the most conservative case, where the stress drop is the largest (e.g. 10MPa).

### 3.4.2 Time dependency of clustering and size distribution of seismicity in Basel

Before the application of this methodology to Basel data, we need to study the dependence of clustering and rupture radius distribution on the number of events (increasing time windows). The exponents of  $D_r$  and  $a_r$  are computed by a linear fit through the linear section of the resulting  $C(r)$  and  $N$ , starting from the estimated minimum radius. Figure 3-3a shows that  $a_r$  exhibits very little variation during the injection phase and slightly decreases in the post-injection phase ( $a_r$  varies between 3.7 and 4.1 in whole seismic activity). This implies that the statistics of larger events (that mostly happen in later stages) may differ from smaller events (early stages). A sensitivity analysis is required to evaluate the applicability of early events to estimate the maximum magnitude as function of perturbed volume. In addition,  $D_r$  is very close to 2 with no clear deviations, reflecting a fractured zone (Figure 3-3b).

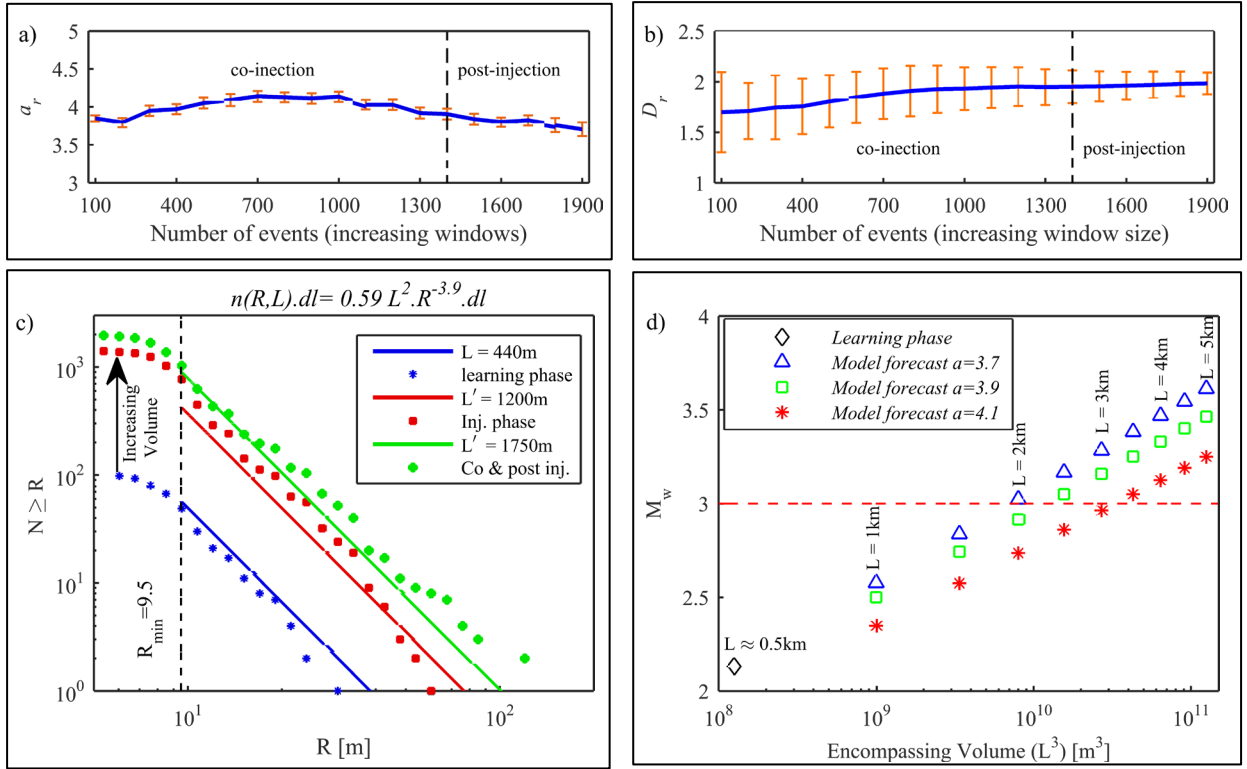


Figure 3-3. (a) Dependence of rupture radius exponent on the number of events in Basel geothermal site. (b) Dependence of rupture clustering on the number events in Basel. (c) Calibration of the seismicity model to the first 100 events (learning phase) during the injection phase and simulation of rupture radius distribution with increasing the encompassing volume in Basel geothermal reservoir. (d) Prediction of maximum moment magnitude  $M_w$  of Basel geothermal reservoir as a function of encompassing volume with an assumption of  $\Delta\sigma = 10$  MPa.

### 3.4.3 Application to Basel

If we choose the first 100 events as the learning phase and compute the completeness magnitude of  $M_c = 0.8$ , the corresponding minimum rupture radius for  $\Delta\sigma = 10$  MPa equals to  $R_{\min} = 9.5$  m. If the events less than  $M_c$  are excluded, remaining events are encompassed by a cube, centred in the casing shoe with a side length of  $L = 500$  m. To ensure all the ruptures do not extend outside of the seismic volume, we compute  $\frac{L}{2}$  by adding the maximum rupture radius and maximum location uncertainty to the maximum distance from the casing shoe. If the average stress drop on every event is 10 MPa, the rupture radius exponent is equal to  $a_r = 3.9$ . If all the parameters of the rupture model is inserted in equation 3.5, the resulting  $\alpha$  is 0.47 and the seismicity model corresponds to equation 3.8.

$$n(R, L)dl = 0.47 L^2 R^{-3.9} dl \quad (3.8)$$

Figure 3-3c represents the calibration of rupture model to the learning phase (blue line). If the injection continues to sweep a larger reservoir volume, the rupture size distribution continues to move upwards (Figure 3-3c). During the injection phase, the perturbed volume is a cube of side length  $L'=1310$  m. If the new  $L'$  is replaced in the model and the resulting rupture radius distribution corresponds to Figure 3-3 (red line). Although the injection has stopped in this step, the fluid is still sweeping a larger reservoir volume, which is verified by the corresponding microseismicity patterns which are growing, and the corresponding perturbed volume of  $L'=2000$  m (green line).

For a seismic hazard assessment, the maximum expected magnitude can be estimated based on a conservative stress drop of 10 MPa. Figure 3-3d represents maximum  $M_w$  as a function of perturbed volume for three different rupture exponents of 3.7, 3.9 and 4.1. The sensitivity analysis shows that the maximum magnitude forecast based on the learning phase (green squares) is not significantly different from to magnitude corresponding to the exponent of 3.7 (blue triangles) for a perturbed volume of approximately  $10^{10}$  m<sup>3</sup>. We choose a random realization in which the large events do not extend outside of the seismic volume. However, this does not affect the maximum magnitude forecast.

### **3.5 Discussions and conclusion**

Two-point correlation function of microearthquake hypocenters in the Basel EGS reservoir showed a complicated behavior, which is not completely linear in a logarithmic scale. Furthermore, the estimated rupture radius of every seismic event follows a power-law, whose slope is independent from the average stress drop on each event. When assuming a constant stress drop on all fracture planes, the resulting ruptures most probably exhibit the statistics of the fracture network. One explanation may be the power-law fracture nature of length distribution in geological formations. Although the scaling exponent does not vary with a change in the average stress drop, but the power-law range varies (particularly the minimum rupture radius). Higher stress drops correspond to smaller rupture sizes and vice versa. Furthermore, the spatial clustering and magnitude of events are correlated through a new scaling law, which relates rupture size exponent and correlation dimension through the exponent of a power-law including the average distance from a seismic event to the closest event of larger magnitude. These observation supported the hypothesis that scaling properties of fracture networks are similar to the scaling of microseismicity patterns.

To interpret the clustering and size distribution of induced events, we generated synthetic fracture networks as a representative of rupture planes. We simulated the factors that complicate



the potential relations between the induced microseismicity and fracture network. Hypocentral locations are quantified by a principal component analysis of the scatter clouds. If the uncertainty of the earthquake hypocenter is included in a synthetic fractal DFN by imposing the statistical distribution of error estimates (normal distributed inside the uncertainty ellipsoids), the resulting correlation dimension increases and approaches to a randomly distributed pattern ( $D=3$ ). However, the increase of randomness depends on the variance of hypocentral coordinates in each direction. In addition, a hydraulic stimulation in a fractured zone might change the 3D spatial distribution from the ideal pattern fracture network pattern. In this case, the correlation dimension of the microearthquakes is very close to 2 (similar to the relocated microseismicity patterns in Basel). Furthermore, adding a fractured zone into a 3D fractal pattern, results in decreasing the correlation dimensions. The third factor in our study was repeating events, which change the spatial distribution and create a sudden drop in the computed correlation dimension. Since the magnitude of repeating events are not necessarily the same, the effect of repeating events on the rupture radius distribution is not clear. To summarize, hypocentral uncertainty, presence of a fractured zone and repeating events complicate the interpretation of spatial patterns of induced seismicity and the correspondence to the underlying fracture network.

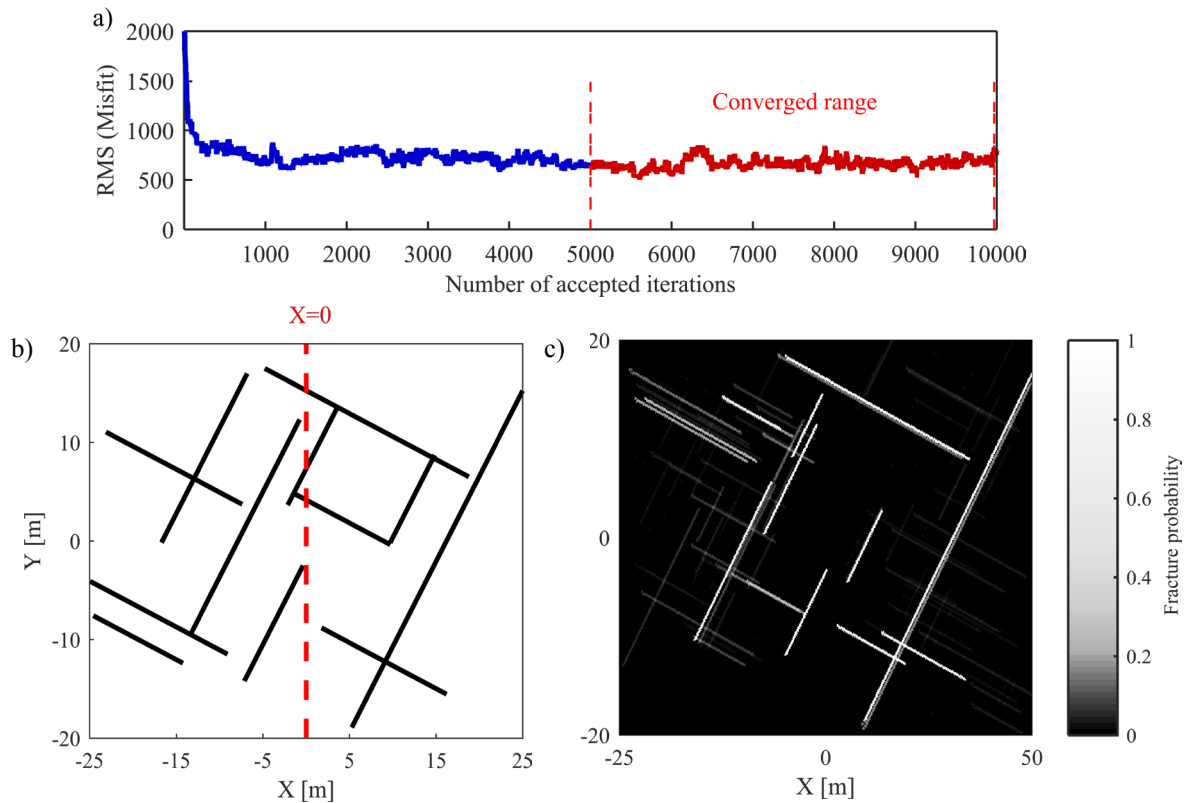
Synthetic networks reveal the restrictions associated with extracting the fracture network geometry from microseismic data. Despite these complexities, the scaling properties of induced seismicity and synthetic fracture networks are very similar. A dual power-law model representing the rupture clustering and size distribution can be applied for modeling the induced microseismicity. This model adds physical representation to the rupture planes as pre-existing fractures, explains the effect of geological and geophysical factors on the scaling properties of induced patterns. Finally, it introduces a universal model that is capable to model clusters with fractal dimension between 2 and 3.

The model parameters must be calibrated on the scaling properties of learning phase. We applied this model to forecast the induced seismicity in Basel geothermal reservoir to assess the seismic hazard of hydraulic stimulation. A reanalysis of Basel microseismicity patterns confirms the independence of clustering from the cumulative number of events. Thus, early stimulation events can exhibit the scaling characteristics of rupture patterns in perturbed reservoir volume. In this case, a learning phase of early first 100 events were applied to set up the model. The seismic hazard assessment is based on the highest reported stress drop in Basel ( $\Delta\sigma=10\text{MPa}$ ). If the injection continues to sweep a larger volume, the associated rupture size distribution, the seismicity model could forecasts the highest rupture radius and the

corresponding seismic magnitude ( $M_w$ ). This model could predict the statistics of seismicity during the co-injection phase as a function of the perturbed volume. The post-injection phase shows slightly different statistics, which may be due to the different stress conditions prevailing in the co-injection and post-injection phases (shut-in and bleed-off phase). Despite the differences, this model was able to reproduce a similar rupture distribution for the co and post-injection phases. Ultimately, the maximum expected magnitude showed a power-law relation with the perturbed reservoir volume in the Basel site. A sensitivity analysis on the rupture exponents revealed the maximum magnitude estimation is not significantly different from the upper bound, which confirms the applicability of this approach for the typical hydraulic stimulations. This difference increases if the perturbed volume is increasing. However, the real-time update of rupture exponent during the hydraulic stimulations and expansion of the learning phase would improve the forecasts.

# 4 Fracture network characterization using stress-based tomography

---



*Reproduced from: Afshari Moein M.J., Somogyvari M., Valley B., Jalali M.R., Loew S., Bayer P., Fracture network characterization using stress-based tomography, Journal of geophysical research, Solid-earth, (Under Review).*



## **Abstract**

Information on structural features of a fracture network at early stages of Enhanced Geothermal System (EGS) development is mostly restricted to borehole images and, if available, outcrop data. However, using this information to image discontinuities in deep reservoirs is difficult. Wellbore failure data provides only some information on components of the in-situ stress state and its heterogeneity. Our working hypothesis is that slip on natural fractures primarily controls these stress heterogeneities. Based on this, we introduce stress-based tomography in a Bayesian framework to characterize the fracture network and its heterogeneity in potential EGS reservoirs. In this procedure, first a random initial discrete fracture network (DFN) realization is generated based on prior information about the network. The observations needed to calibrate the DFN are based on local variations of the orientation and magnitude of at least one principal stress component along boreholes. A Markov Chain Monte Carlo (MCMC) sequence is employed to update the DFN iteratively by a fracture translation within the domain. The Markov sequence compares the simulated stress profile with the observed stress profiles in the borehole, evaluates each iteration with Metropolis-Hastings acceptance criteria and stores acceptable DFN realizations in an ensemble. Finally, this obtained ensemble is used to visualize the potential occurrence of fractures in a probability map, indicating possible fracture locations and lengths. We test this methodology to reconstruct simple synthetic and more complex outcrop-based fracture networks and successfully image the significant fractures in the domain.

## **4.1 Introduction**

Although the amount of thermal energy in the earth's crust is enormous and could substantially contribute to the world's energy supply (Tester et al. 2006), the current geothermal energy production is limited to particular geological locations where water is circulated at sufficient flow rates through hot rock masses. In a standard geological setting, the minimum temperatures, ( $> 120^{\circ}\text{C}$ ) for producing electricity from geothermal fluids, are mostly found in crystalline basements between 4-6 km depth (Evans 2015), where the permeability is typically low (Achtziger-Zupančič et al. 2017). These systems, usually known as Enhanced Geothermal Systems (EGS), require hydraulic stimulation (i.e. massive fluid injections) to increase the natural flow rates. Permeability creation is expected to improve the heat-exchange capacity and thus permit sustainable heat extraction. Flow in EGS systems develops primarily in the fracture network (Davatzes and Hickman 2010; Genter et al. 2010) and injecting high-pressure fluid reduces the effective stress on fracture planes, which results in rock mass deformation due to poroelastic interactions. Since these systems are for the most part critically stressed (i.e. close

to failure), fluid injections may induce slip on pre-existing discontinuity planes (Evans 2005). However, the mechanisms of permeability enhancement in hydraulic stimulation are not entirely understood (Amann et al. 2017; Evans et al. 2005a). Such failures are mostly associated with seismic activity that represents a common problem in EGS developments (Davies et al. 2013; Ellsworth 2013; Evans et al. 2012; Giardini 2009). For example, high level of seismic activity led to the suspension of Basel (2006) and Saint-Gallen (2013) geothermal projects in Switzerland (Edwards et al. 2015; Häring et al. 2008; Moeck et al. 2015). Hydraulic stimulation scenarios should increase the permeability while keeping the seismicity on a safe and non-damaging level (Evans 2015). Induced seismicity is a complex interaction between the natural fractures and in-situ stress change caused by fluid pressure (Evans et al. 2005d; Gaucher et al. 2015).

A geological model with a reliable representation of lithological domains and characterization of the fracture network is key to the design of reservoir creation strategies. Furthermore, it is fundamental to quantitatively analyze the possible relations among the spatial, temporal or magnitude distribution of induced seismicity and thermo-hydraulic-mechanical characteristics of a fractured rock mass, which is not yet fully understood (Amann et al. 2017). Such a geological model is also crucial for real-time monitoring and seismic risk assessments of a hydraulic stimulation. A geological model requires a complete reservoir characterization, with information on important fracture attributes like density, orientation, type, aperture and length distributions.

The primary information on the natural fractures in deep reservoirs stems from borehole image logs (e.g. optical televiewer or ultrasonic logs). These images provide limited information on the location and orientation of fractures if they cut through the borehole. Statistical analysis of fractures on boreholes or analogs permits the definition of fracture sets (Ziegler et al. 2015) and also provides the spacing distribution within each fracture set (Moein et al. 2016). However, a deterministic reconstruction of three-dimensional (3-D) fracture networks from even a few boreholes is difficult. Borehole data captures local deterministic elements of a fracture network. However, other items in the surrounding network can only be approximated or described in a probabilistic way (e.g. Illman et al. 2009; Karra et al. 2018; Tezuka and Watanabe 2000). Thus, stochastic realizations often referred as discrete fracture networks (DFN), are generated based on a statistical characterization of fracture network attributes (e.g. Berrone et al. 2017; Dreuzy et al. 2012).

One possible approach is to limit the 3-D spatial distribution of fractures using stereological relationships, as proposed by Darcel et al. (2003b). However, the application of these relationships to borehole data still includes a significant uncertainty, even if the fracture length distribution is known (Afshari Moein et al. 2018a). Induced microseismicity is another source of information that may reflect some geometrical aspects of fracture network (Afshari Moein et al. 2018b; Evans et al. 2005d; Moriya et al. 2003; Williams-Stroud et al. 2010). However, this information becomes available only after the execution of hydraulic stimulation and thus is not available in time for stimulation design purposes.

A fundamental point for our work is that natural forces largely influence the in-situ stress state in geological settings (e.g. Barton and Zoback 1994; McNamara et al. 2015; Pierdominici et al. 2011; Rajabi et al. 2017; Sahara et al. 2014; Valley 2007; Yale 2003). Stress fluctuations on boreholes often show strong heterogeneities (e.g. Schoenball and Davatzes 2017; Shamir and Zoback 1992; Valley and Evans 2007b) that may also be characterized by scaling relationships (e.g. Blake and Davatzes 2011; Day-Lewis et al. 2010; Valley and Evans 2014a). These observations also suggest that the characteristics of the fracture network affect the stress variability within the rock mass. If only a single fracture is present in the rock mass, the size of stress perturbation depends primarily on the size of the fracture (Pollard and Segall 1987). Nevertheless, in the situation where multiple fractures interact, the relation between the in-situ stress fluctuations and critical characteristics of a fracture network is complex and not completely understood (Rutqvist 2015; Tsang et al. 2018; Valley et al. 2014).

In the present study, we propose constraining the critical characteristics of the fracture network using in-situ stress heterogeneities inferred from borehole images. Valley et al. (2014) suggested an inversion approach to extract the geometrical characteristics of a fracture network by minimizing the difference between computed and observed horizontal stress orientation variability in a single borehole. This approach successfully reconstructed the geometry of a single fracture intersecting the borehole. On the other hand, the plan failed to determine the geometry of complex fracture networks, in which all of the fractures do not necessarily intersect the borehole. The inversion technique that we present, also referred to as stress-based tomography, reconstructs the fracture network geometry using the vertical stress profiles through a Bayesian approach. We apply a quasi-static geomechanical simulator to model the stress variability within a fracture network efficiently and to extract the associated borehole stress profiles. During the inversion process, we also use prior knowledge on mechanical properties of the rock mass and the statistical properties of fracture attributes (length, orientation and density). The inversion delivers a probability map that illuminates the probable fracture

locations and their lengths. We test this approach through the use of a simple synthetic DFN, and a more complex outcrop mapped DFN. Finally, we discuss the applications and limitations of the inversion technique for deep boreholes and present an outlook for future developments.

## 4.2 In-situ stress characterization

Information on the in-situ stress state is fundamental to any seismo-thermo-hydro-mechanical characterization of fractured reservoirs (Amann et al. 2017; Ghassemi 2012; Preisig et al. 2015; Zoback 2010). Complete characterization of a stress tensor requires six parameters at any point. The assumption that one principal stress,  $S_v$ , is vertical and equal to the weight of the overburden, reduces stress characterization to the determination of the magnitude and orientation of the maximum and minimum principal horizontal stresses,  $S_{hmax}$  and  $S_{hmin}$ , respectively (Amadei and Stephansson 1997), along with the determination of their trend with depth. Depending on the relative magnitudes of  $S_{hmin}$ ,  $S_{hmax}$  and  $S_v$ , different faulting regimes may be present such as normal, strike-slip and thrust faulting (Anderson 1951).

The vertical stress  $S_v$  is typically computed by integrating over the density log from the surface to a predetermined depth. The minimum horizontal stress,  $S_{hmin}$  is estimated from pressure monitoring during hydraulic fracturing tests (if they propagate perpendicular to  $S_{hmin}$ ) performed in isolated intervals (Fairhurst 2003; Lin et al. 2008; Ljunggren et al. 2003; Schmitt et al. 2012). However, estimation of the maximum principal stress  $S_{hmax}$  is somewhat challenging and associated with a significant amount of uncertainty. One approach is to assume that the rock is critically stressed and the rock strength behavior follows Mohr-Coulomb failure criteria with a friction coefficient between 0.6 – 1, and to compute the possible values for  $S_{hmax}$  (Hickman and Davatzes 2010; Zoback et al. 2003). This approach estimates a wide range of possible values for  $S_{hmax}$ . An alternative solution is to apply the width of borehole breakouts (Barton et al. 1988), which also relies on some assumptions and application of failure criteria. This approach results in  $S_{hmax}$  estimates, which are primarily dependent on the used failure criterion (Valley and Evans 2015b). Typically, these estimates are applied to derive a first-order characterization by fitting a linear depth trend to the principal stress magnitudes (Cornet and Bérard 2003; Valley and Evans 2015b).

Despite the magnitude estimations, the orientation of principal horizontal stresses may be estimated robustly from the borehole failures observed in image logs. In vertical boreholes, breakouts are aligned with the direction of minimum principal horizontal stress,  $S_{hmin}$ , and drilling-induced tensile fractures are formed in the direction of maximum principal horizontal stress,  $S_{hmax}$  (Zoback et al. 2003). Figure 4-1a represents an example of a 360° view of an image



log along the borehole GPK4 drilled at the Soultz-sous-Forêts EGS site in France, in which the natural fractures are regular sinusoids. Stress-induced features form as axial drilling-induced tension fractures (ADITFs) and en-echelon drilling-induced tension fractures (EDITFs). Figure 4-1b and Figure 4-1c display the reflectivity image and borehole radius of a typical interval from the borehole drilled into Basel EGS, in which continuous borehole breakouts accompany a natural fracture.

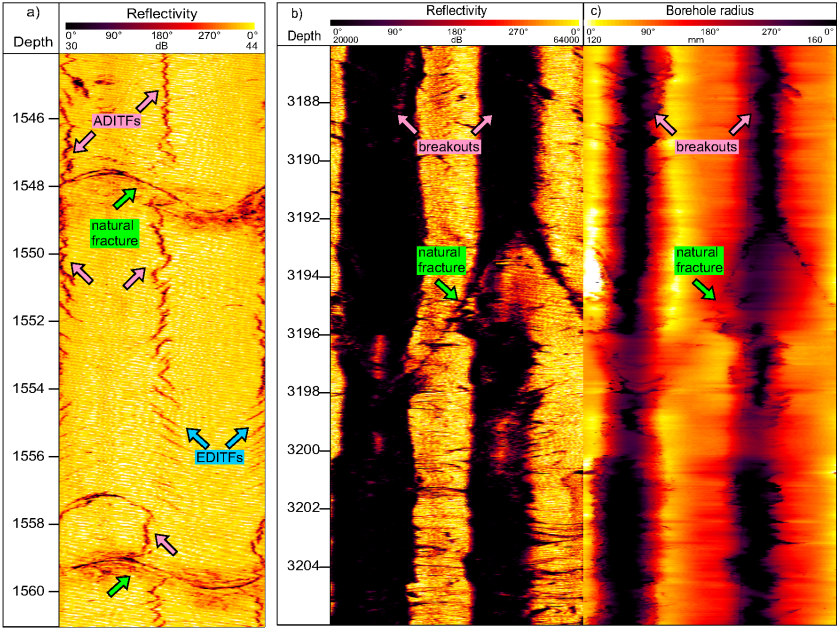


Figure 4-1. (a) A typical image log of GPK4 borehole drilled into Soultz-sous-Forêts EGS including the natural fractures and stress induced fractures (ADITFs and EDITFs). (b) and (c) depict an example of reflectivity and borehole radius from Basel-1 well, including borehole breakouts along with a natural fracture (Valley et al. 2014).

Figure 4-2a. shows the estimated profiles of  $S_{hmin}$ ,  $S_{hmax}$  and  $S_v$  based on hydraulic tests, borehole breakouts and density logs in the borehole drilled into Basel EGS. The detailed methodology to compute such profiles has been explained by Valley et al. (2014). Figure 4-2b displays the orientation of maximum horizontal principal stress orientation,  $S_{hmax}$ , inferred from the azimuth of borehole failure over successive 0.4 m windows on Basel borehole images. The deviation from the average  $S_{hmax}$  orientation along the entire well (N144°, Valley and Evans (2009)) is presented in Figure 4-2b.

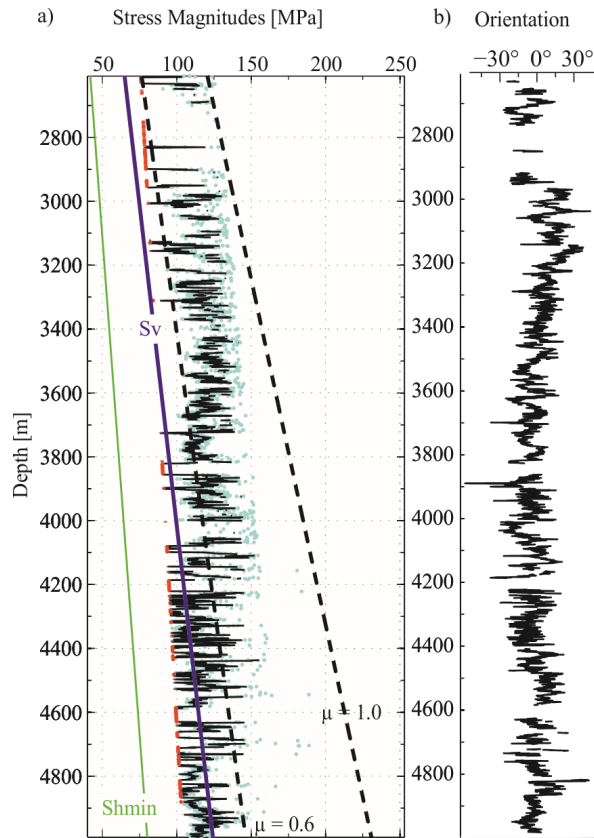


Figure 4-2. (a) Estimates of principal stress magnitudes in Basel EGS (Valley and Evans 2015b). (b) Orientation of minimum principal horizontal stress inferred from borehole breakouts in the borehole drilled into Basel EGS (Valley and Evans 2009).

### 4.3 Methodology

#### 4.3.1 Forward simulation of stress variability in a fractured domain

In this chapter, we present the assumptions, the numerical code and necessary information for simulating the geomechanical response and observed stress conditions in a fractured rock mass. For the sake of simplicity, we treat the problem as a 2-D plane strain case, i.e. we expect a vertical planar section for the model containing a vertical borehole and cut by fractures with an infinite out-of-plane dimension. The rock mass is assumed to be isotropic, homogenous, and fractures are elasto-plastic Mohr-Coulomb frictional interfaces that may slip in the applied far-field stresses.

The inversion process requires efficient and fast modeling of the stress variability induced by fractures within the rock mass. Conventional finite element codes are typically computationally demanding for modelling the mechanical response of a fractured rock mass under given stress conditions. Since the inversion process requires simulation of many realizations, we used a fast two-dimensional (2-D) simulator based on the displacement discontinuity method (DDM)

developed by Jalali (2013). The DDM is an indirect boundary element method, which was developed by Crouch et al. (1983) based on an analytical solution to solve the finite line segment in an infinite body presented by Salamon (1963). This method was initially developed to model the mechanical behavior of thin underground excavations and then expanded for geomechanical modeling of fracture networks. Later on, the geomechanical simulator was coupled with a finite difference hydraulic simulator for hydromechanical modeling of fluid injection into fractured reservoirs (Jalali 2013; Jalali and Valley 2015).

In the model, a fracture is discretized into multiple fracture segments, and any segment has two degrees of freedom: 1) normal, and 2) shear displacement discontinuities. Induced displacement and stress at any point in the medium (including the fracture segments) can be estimated as a linear combination of all fracture segments' discontinuities. One must know the values of the discontinuities before the estimation of displacement and stress in the medium. The stress and displacement at each fracture segment (combination of in-situ and induced) are written as a linear combination of all the fracture segment discontinuities. Fracture mechanics laws (here: Barton-Bandis model) are used then to derive the fracture segments' stress and displacement as a function of displacement discontinuities. The peak shear stress is estimated using a Mohr-Coulomb (MC) criterion and pre-shear elastic behavior. Beyond the peak shear stress, the fracture shear stiffness is taken as zero (sliding-fracture). Dilation angle is considered as a constant that is dependent upon effective normal stress level during sliding and otherwise is zero. Further details about the implementation of the DDM approach in the mechanical modeling of fractured rocks is provided by Jalali (2013).

Here, we apply far-field stresses on the fractured domains and allow the fractures to slip to redistribute the stress within the entire domain. The simulator also returns the normal and shear displacements on each fracture planes. Then, we extract the stress fluctuations on a borehole in the center of the domain, which will be applied for DFN inversion.

Constraining far-field stresses from the current stress state inferred from borehole data is not straightforward. We assume the far-field stress can be approximated by averaging the stress variation observed along the borehole. The current stress field can result from the superposition of successive tectonic phases. However, to keep the problem tractable, we assume that the current stress field has developed under a single loading event. In this study, for illustrating the inversion procedure, we assume far-field stress of 20 MPa horizontal, 38 MPa vertical stress on the 2-D DFNs with zero shear stress. As a relatively short vertical extent is considered in the model, we neglect the gravity-driven stress magnitude increasing with depth.

The simulator requires the definition of rock and fracture properties based on available information from geophysical logging and laboratory tests on cores. The required information on these properties is assumed constant in the inversion process (listed in Table 1). The fracture stiffness is difficult to constrain (both shear and normal). However, its impact is limited if plastic slip occurs. Thus, stiffness is considered constant during the inversion.

To ensure the slip-on fracture planes in every case, a low friction angle of  $\phi = 10^\circ$  is selected. The geomechanical simulator delivers the stress redistribution within the network at every point (horizontal, vertical and shear stresses). Here, we define a parameter  $\beta$ , which indicates the orientation of maximum principal stresses from the vertical borehole (positive clockwise). This parameter is computed using the following equation:

$$\tan(2\beta) = \frac{2\tau}{\sigma_{yy} - \sigma_{xx}} \quad (4.1)$$

where  $\tau$  represents the shear stress,  $\sigma_{yy}$  is vertical stress and  $\sigma_{xx}$  denotes the horizontal stress at any point along the borehole.

Table 4-1. List of input parameters for geomechanical modeling of fractured rocks using DDM simulator

Far-field principal stresses	minimum principal stress horizontal	$\sigma_3 = -20$ MPa
	maximum principal stress vertical	$\sigma_1 = -38$ MPa
Rock properties	Young's Modulus	$E = 60$ GPa
	Poisson's ratio	$\nu = 0.25$ MPa
Fracture properties	normal stiffness	$K_n = 10^{11}$ Pa/m
	shear stiffness	$K_s = 10^{10}$ Pa/m
	cohesion	$c = 0$ MPa
	friction angle	$\phi = 10^\circ$

#### 4.3.2 Principles of Bayesian inversion

A Bayesian inversion framework is used to fit the DFN models to the observed stress measurements. In general, Bayesian inference aims to provide a probabilistic model to a set of unknown parameters and deliver a probabilistic characterization of unknown model parameters. The posterior probability distribution is computed based on an available prior collection of information and the likelihood of observations (Gelman et al. 2014). Bayesian inversion has been applied to related geological problems such as for reconstruction of the stress field (Lecampion and Lei 2010) and characterization of flow and transport in heterogeneous media

(Lee and Kitanidis 2013; Mondal et al. 2010). The Markov Chain Monte Carlo (MCMC) method is one of the most common techniques of Bayesian inference in geosciences. MCMC has been applied to solve inverse problems using various sources of information such as seismic tomography (Bodin et al. 2012), tracer tomography (Jiménez et al. 2016) and fracture network intersections with boreholes (Mardia et al. 2007). The transdimensional reversible jump Markov Chain Monte Carlo (rjMCMC) is a unique variant of MCMC, in which the number of parameters can vary among subsequent iterations during the inversion process. Somogyvári et al. (2017) introduced this inversion approach for calibrating orientation, lengths and numbers of fractures in DFNs using cross-well tracer tomography experiments. That work is also the basis for the presented stress-based inversion procedure, but we keep the number of fractures during the inversion fixed.

### **4.3.3 Inversion methodology**

The stress-based tomography requires at least two components of in-situ stress (one magnitude and one orientation). Preliminary analysis shows that one single stress orientation is not sufficient to reconstruct simple DFNs with a very small number of fractures (presented in supporting information, Appendix C). Two stress components, for example, the orientation of minimum principal stress (observation 1) and one magnitude amongst  $S_{hmin}$ ,  $S_{hmax}$  and  $S_v$  (observation 2) is sufficient for solving the inverse problem. However, estimates of all three quantities are still required for defining the far-field stress in this analysis (as discussed in Chapter 3.1).

#### **4.3.3.1 Prior information on fracture network**

The inversion procedure requires prior knowledge of the statistical distribution of fracture attributes within the study domain. The fundamental understanding of the fracture length distribution is a pre-requisite to populate the initial DFN in the inversion process (Figure 4-3). Fracture length ( $l$ ) distribution in geological formations has been reported to follow power-law distributions on different scales like  $n(l) dl = c l^{-a} dl$ , where  $a$  is the length exponent and  $c$  is a constant of normalization. The power-law exponent of the fracture length distribution in 2-D outcrops is typically between 1.5 and 3.5 (Bonnet et al. 2001; Torabi and Berg 2011). Also, the fracture positions on the specified borehole may be inferred from image logs. The fractures cutting the borehole compute the minimum fracture spacing in each set. However, the location of fractures along the borehole is not fixed in this study. Moreover, the orientation of fractures in deep boreholes mostly belong to two dominant fracture sets (Valley and Genter 2007; Ziegler

et al. 2015), which may be considered as prior information and invariant in the inversion process..

#### 4.3.3.2 *Inversion procedure*

In Bayesian inference, data is handled as random variables with given probability density functions (PDF). Hence, the inverse problem can be expressed using Bayes' theorem as

$$P(\theta|\xi) = \frac{L(\xi|\theta)P(\theta)}{P(\xi)} \quad (4.2)$$

where  $P(\theta|\xi)$  denotes the posterior probability of the inverse problem (the target distribution, i.e. the probability of a model parameter  $\theta$  given the observation data of  $\xi$ ).  $L(\xi|\theta)$  is the likelihood function (the probability of an observation vector  $\xi$  given the model parameter vector  $\theta$ ),  $P(\xi)$  is the observation probability, and  $P(\theta)$  is the prior information.

If we consider that stress observations (orientation and magnitude at a given borehole) follow a normal distribution, the likelihood function can be written as

$$L(\xi|\theta) = \frac{1}{\sqrt{4\pi\sigma^2}} \exp\left(-\frac{(\xi - f(\theta))^2}{4\sigma^2}\right) \quad (4.3)$$

where  $\sigma^2$  is the variance of the normal distribution, and  $\xi(\theta)$  is the forward model for the simulation of the stresses. This function is equivalent to computing a root mean squared (RMS) misfit (Aster et al. 2011). In this work, we use multiple types of observations together, and thus the used likelihood function is the product of numerous normal distributions. The sensitivity of the inversion towards the different observations can be tuned by the variance values.

In equation 4.2,  $P(\theta)$  represents the prior, that is, the information known about the model parameters before the inversion. The prior information here is mainly used to generate the initial solution of the inversion.  $P(\xi)$  is the probability of observations, which could be written as the following marginal distribution over the complete model space:

$$P(\xi) = \int L(\xi|\theta)P(\theta)d\theta \quad (4.4)$$

This marginal distribution is not a function of the models, and thus it can be considered constant throughout the inversion. The posterior probability function cannot be expressed in an analytical form, but it can be calculated for specific models. MCMC uses this property, as it calculates the target distribution as particular models. The main idea behind MCMC is to create

a Markov chain with a stationary distribution that matches the target distribution, the posterior. This is obtained by specifying a transition kernel, which is a set of rules to create the next chain element from the previous one ( $\theta_i \rightarrow \theta'$ ). A random update to propose a new model parameter vector ( $\theta'$ ) with the probability  $q(\theta_i \rightarrow \theta')$  is chosen here. We use the Metropolis-Hastings algorithm, where this update step has to be reversible, and thus the update  $q(\theta' \rightarrow \theta_i)$  must be realized by a probability value, too. Reversibility ensures the stationarity of the Markov chain. The workflow and implementation of the algorithm are presented in Figure 4-3.

The initial fracture network is generated randomly using a known power-law length distribution with a given minimum fracture spacing (Somogyvári et al. 2017). This initial solution is then entered in the iterative MCMC algorithm. During each subsequent iteration, one fracture is randomly selected, then a new fracture center is drawn from a uniform distribution over the area of investigation. Subsequently, the forward model is simulated with the updated DFN realization. The acceptance probability of a proposed model realization is calculated as

$$\alpha(\theta', \theta_i) = \min \left\{ \frac{L(\xi|\theta') p(\theta') q(\theta' \rightarrow \theta_i)}{L(\xi|\theta_i) p(\theta_i) q(\theta_i \rightarrow \theta')}, 1 \right\} \quad (4.5)$$

This expression is known as the Metropolis-Hastings acceptance criterion (Geyer 2011). It depends on the ratio of the likelihoods and the priors, as well as the ratio of the probability of the reverse and the forward proposal step. The calculation of this ratio is more straightforward than calculating the individual posteriors as there is no need to estimate the marginal distribution of the observations anymore. Because the fracture movement update uses the same uniform distribution, the probabilities  $q(\theta' \rightarrow \theta_i)$  and  $q(\theta_i \rightarrow \theta')$  are the same, and the acceptance criterion simplifies to

$$\alpha(\theta', \theta_i) = \min \left\{ \frac{L(\xi|\theta') p(\theta')}{L(\xi|\theta_i) p(\theta_i)}, 1 \right\} \quad (4.6)$$

This version of MCMC is known as the random-walk Metropolis-Hastings algorithm (Brooks et al. 2011). After the acceptance criterion is calculated, a random number from the interval  $[0,1]$  is drawn and compared to  $\alpha$ . If the drawn number is smaller, the proposed realization gets accepted. This is equivalent to the update being accepted with a probability  $\alpha$ . The accepted realization gets stored (otherwise the last accepted model is kept), and the next iteration starts with its random update. The stored set of model realizations is called the ensemble, which is the result of the MCMC simulation. The first half of the ensemble is discarded to remove the

bias of the initial model choice,  $t$ . The ensemble thus represents the investigated posterior probability distribution, and not only one calibrated model realization.

#### 4.4 Test cases

We test the methodology by reconstructing two synthetic fracture networks with known geometry (i.e. given position, orientation and length distribution of the fractures). The first case is a simple synthetic fracture network built up by a few fractures, and the second case presents a more complex and realistic fracture network mapped from outcrop field data. Table 2 represents the geometrical characteristics of both DFNs of the test cases. Both are described by two fracture sets.

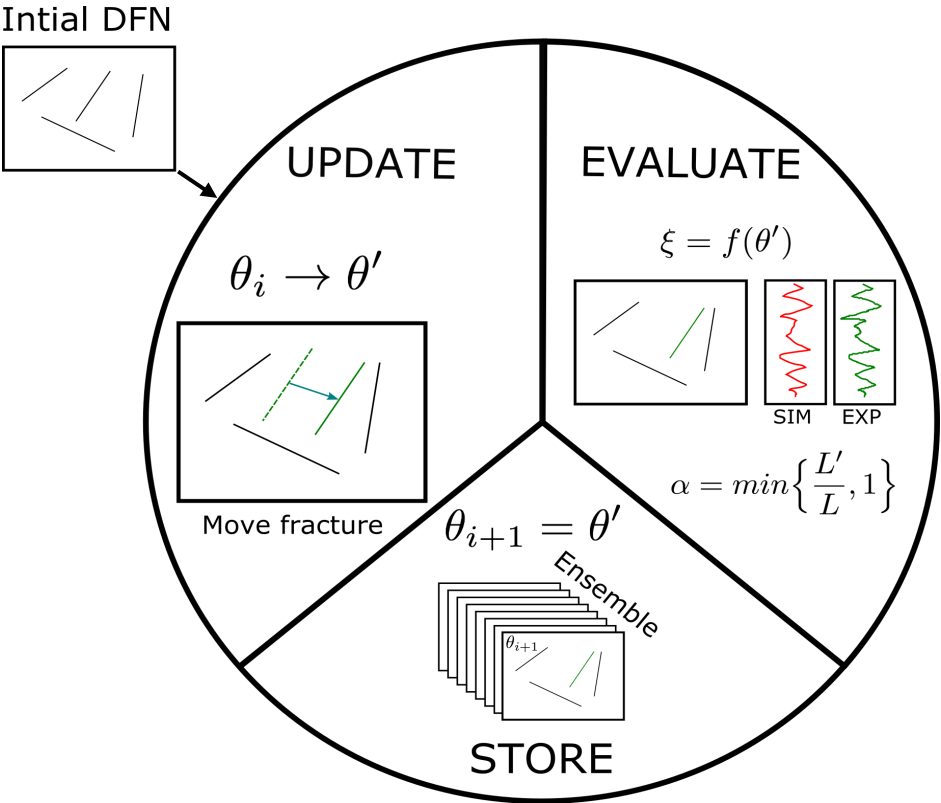


Figure 4-3. Overview of the MCMC algorithm:  $\theta$  denotes the model vector,  $\theta_i$  is the last accepted model,  $\theta'$  is the proposed model,  $\xi$  is the observation vector (the stress measurements),  $f(\theta)$  is the forward model,  $\alpha$  is the Metropolis-Hastings acceptance criteria, and  $L$  is the likelihood function. The initially generated DFN goes into the loop, and the DFN is updated by the movement of a randomly selected fracture. Each realization is evaluated using Metropolis-Hastings criteria (SIM is the simulated stress perturbation; EXP is the observed or expected stress perturbation), and any accepted realization is stored in the ensemble. The ensemble is finally converted to a probability map using the methodology described in Chapter 5.1.



Table 4-2. Geometrical characteristics of test cases

Cases	Simple synthetic network		Outcrop-based network	
	Set 1	Set 2	Set 1	Set 2
Fracture orientation from vertical borehole (positive clockwise)	45°	-45°	30°	-65°
Minimum spacing	10 m	10 m	2.55 m	2.5 m
Fracture length exponent ( $a$ )	1.5		2.6	
Minimum fracture length	40 m		8 m	
Total fracture length	250 m		220 m	
Domain size	100 x 100 m <sup>2</sup>		50 x 40 m <sup>2</sup>	

#### 4.4.1 Simple synthetic network

This case contains four large fractures from two orthogonal orientations within a domain of 100×100 m<sup>2</sup>. The minimum spacing between fractures of the same sets is 10 m, the minimum length of the fractures is 40 m, and the total length within the domain is 250 m. Before starting the inversion procedure, we need to simulate the stress variability within the domain and extract the stress profiles along the pre-defined borehole. Here, the borehole is placed in the center of the domain.

Figure 4-4a and Figure 4-4b present the  $\sigma_1$  and  $\beta$  variations within the synthetic network domain [-50, 50] due to fracture slip loaded by the far-field stresses defined above. The simulation parameters are listed in Table 1. The borehole is situated in the center of the domain ( $X = 0$ ) parallel to the Y-axis, and here the simulated stress profiles are extracted. These profiles, shown in Figure 4-4c and Figure 4-4d, are computed at 50 cm resolution along the borehole (i.e. based on 201 data points in the borehole). To summarize, we aim at reconstructing the DFN geometry in Figure 4-4a by using these two stress profiles and prior information listed in Tables 1 and 2.

#### 4.4.2 Outcrop-based network

This case represents a more complex fracture network, which is based on outcrop field data. This fracture network is mapped from Tschingelmad crystalline outcrop in upper Aar valley in Grimsel region of Central Alps, Switzerland (Ferrari et al. 2017; Ziegler et al. 2014; Ziegler et al. 2013). For a detailed description of the geological settings in the given area, we refer to the previous references. Figure 4-5a represents a schematic view of the geological model of the mapped area, and Figure 4-5b shows the mapped fracture network. We selected an area of 50 ×

40 m<sup>2</sup> for this analysis and mapped the fractures with a minimum length of 8 m. The fractures in this area belong to two primary fracture sets. Their orientations are approximately 30° and -65° from the vertical axis (positive clockwise).

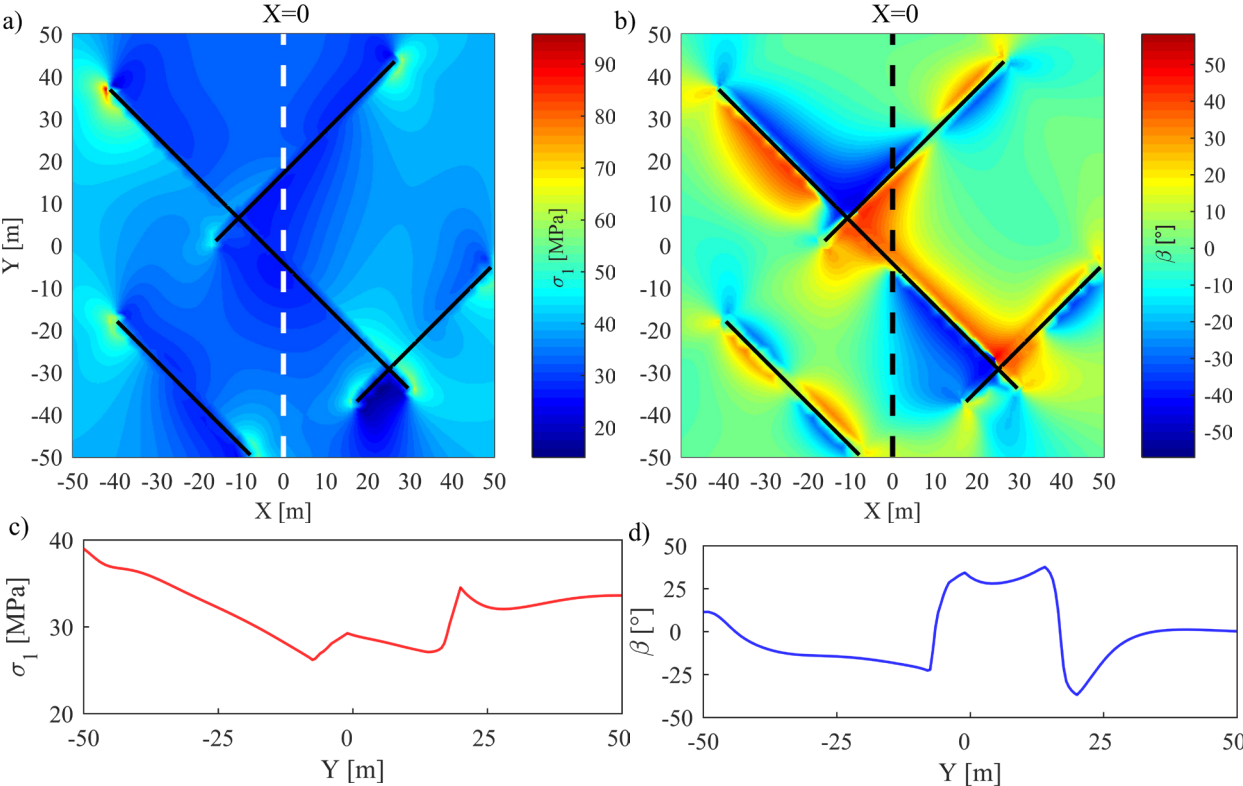


Figure 4-4. Forward simulation of stress variability within the simple synthetic network given the geometrical characteristics listed in Table 2, and using input parameters for the geomechanical model from Table 1. Figure (a) depicts the  $\sigma_1$ -field and (b) the  $\beta$ -field. Stress magnitude and orientation profiles representing the stress fluctuations along the borehole ( $X=0$ ) are shown in (c) and (d).

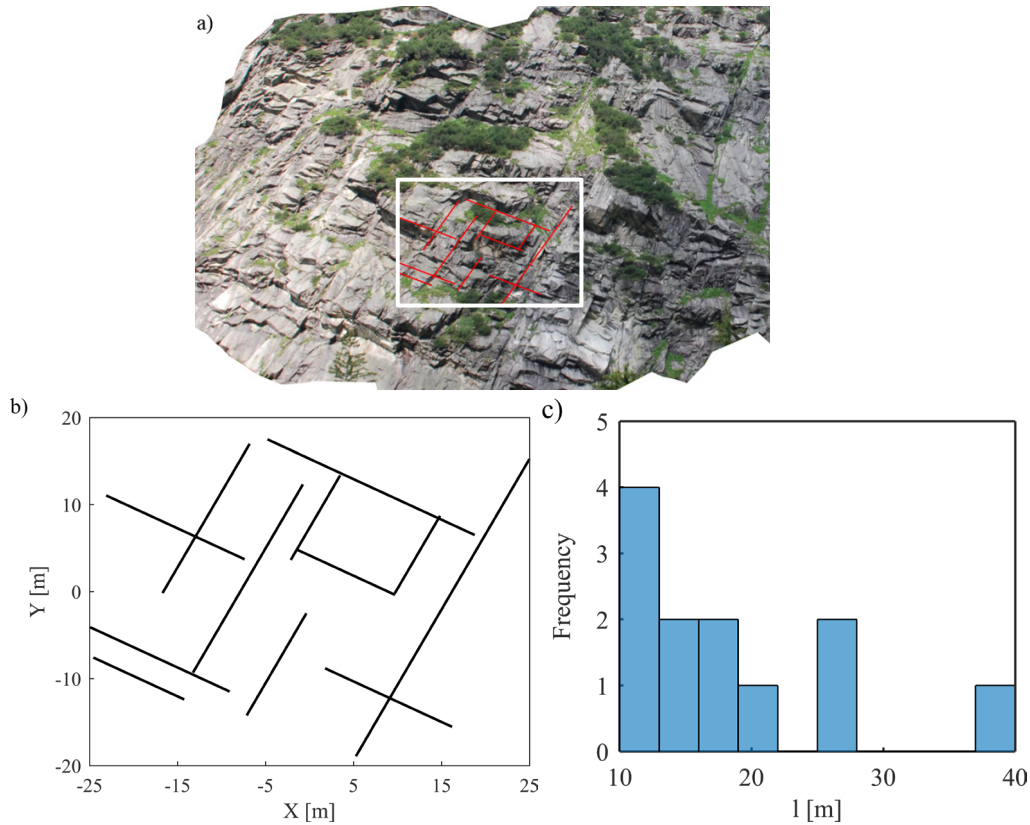


Figure 4-5. (a) Surface geological model of the Tschingelmad outcrop in Alps. (b) Fracture network mapped from the geological model. The fractures larger than the pre-defined cut-off (8 m) are mapped. (c) Histogram of fracture length distribution.

The network of Figure 4-5b follows a power-law length distribution with an exponent of 2.6 and a cut-off at a length of about 8 m. Since the large fractures are of highest importance to the hydro-mechanical response of fractured rocks

(Baghbanan and Jing 2007; Darcel et al. 2003c; de Dreuzy et al. 2001), we ignore the fractures smaller than the cut-off length. A power-law length exponent is derived by fitting a power-law distribution to the histogram of fractures within the domain as illustrated in Figure 4-5c. The corresponding probability density function of the mapped network thus reads as  $p(l)dl = 0.16 l^{-2.6}dl$ . A power-law is fit to the whole fracture network (without any cut-off) so that robust estimates of the constants in this equation are created. This probability density function is required to define the initial DFN realization.

Similar to the synthetic case, we first simulate the stress variability induced by fractures, when far-field stresses are applied. The simulation parameters are the same as for the simple synthetic case. Then, we place a borehole in the center of the domain at  $X=0$  (parallel to Y-axis) and extract the stress heterogeneities along it. Figure 4-6a and Figure 4-6b represent the resulting magnitude  $\sigma_1$  and orientation  $\beta$  fields within the entire domain, respectively. Figure 4-6c and

Figure 4-6d show the  $\sigma_1$  and  $\beta$  profiles computed at every 20 cm along the borehole (to have 201 data points in the borehole similar to the hypothetical case). The inversion procedure aims at reconstructing the DFN geometry in Figure 4-5b using these stress profiles and prior knowledge on the rock mass and fracture network presented in Tables 1 and 2.

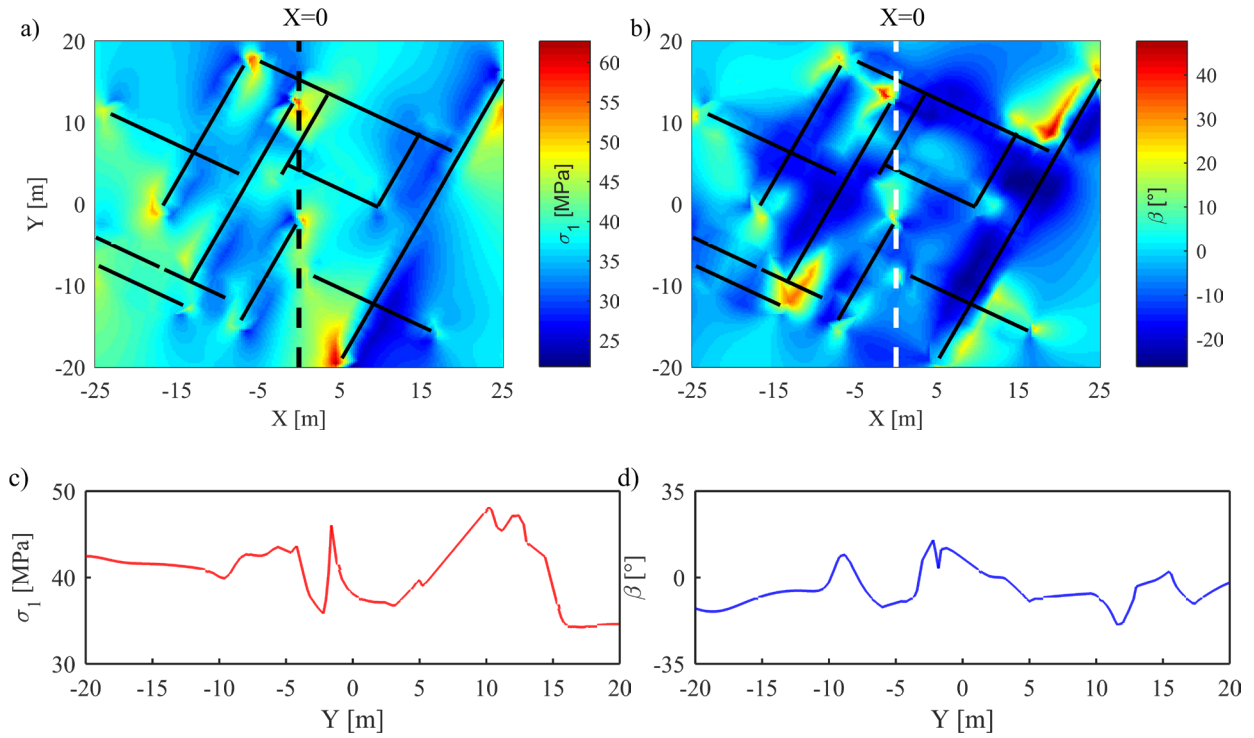


Figure 4-6. Forward simulation of stress variability within the outcrop-based fracture network with the characteristics listed in Table 2 and input parameters of the geomechanical model from Table 1, a)  $\sigma_1$  field and b)  $\beta$  field. Profiles representing the variability are depicted in c)  $\sigma_1$ , and d)  $\beta$  at  $X = 0$ .

## 4.5 Results

An essential question of MCMC methods is when to stop the sequential simulations or, in other words, when the sampling can be considered complete? Here, we followed the recommendations by Gelman et al. (2004) to check the convergence of individual parameters until they converge to a joint distribution. The inversion process provided a large number (more than 100 for the simple synthetic case and more than 1,000 for the outcrop-based case) of accepted DFN realizations. As a standard practice, the first half of the chain was considered as the burn-in period and discarded (Geyer 2011) to eliminate the effects of the initial model, and not considered for visualization of the ensemble.

Straightforward ways of visualizing features of a final ensemble are plotting exemplary DFN realizations or taking the mean of all geometric parameters, but these would significantly reduce

the real information content of the ensemble. The resulting ensemble is more than just a collection of plausible solutions, but it is the representation of the posterior probability function. Another approach is to extract higher-order statistical properties of the individual DFN parameters, which however may obscure spatial correlation of results. Instead, a fracture probability map as presented by Somogyvári et al. (2017) was derived for each case. Such a map is created by rasterizing the individual DFN realizations and then stacking these together. The local probabilities are calculated pixel by pixel, based on the frequency of fracture occurrence. The full map depicts the probabilistic location and length of fractures within the study domain, it can easily be analyzed visually and may be used for further analyses.

#### 4.5.1 Simple synthetic case

Here, we first explain the results for the synthetic case. First of all, a random DFN realization (known as initial DFN) with the geometrical properties listed in Table 1 was generated. The initial DFN for the inversion process of the simple synthetic case is presented in the supporting information (Appendix C). The MCMC algorithm applied the stress profiles in Figure 4-3c and Figure 4-3d as the observation profiles to reconstruct the initial fracture network geometry of Figure 4-4a. The Markov sequence kept moving the fractures inside the domain while respecting the minimum spacing of fractures in each set. It compared each realization-specific stress profile at  $X = 0$  with the “true” one of Figure 4-4 to assess the misfit. When the updated DFN met the Metropolis-Hastings acceptance criteria, the DFN was stored in the ensemble. We let the MCMC algorithm run 24 hours on an office PC (single thread, Intel® Core i7™-6700k 4 x 4.0 GHz).

Since the DFN is not complex, the MCMC algorithm converged to the initial DFN relatively fast. Figure 4-7a shows that there is a rapid misfit decrease after the first 50 accepted realizations and the computed misfit remains relatively constant after that. However, the ensemble size may be significant and include a large number of parameters. For the presentation of the posterior distribution, a subset of the converged range is selected as the final ensemble, and as outlined above the first half of realizations discarded.

Figure 4-7b and Figure 4-7c compare the hypothetical case with the probability map derived from the visualization of the obtained ensemble. The light colors in Figure 4-7c denote the most probable locations of the fractures, while the black color indicates that no fracture is present. Figure 4-7c reveals that the inversion recognizes well the location and length of the fractures within the network, although they are not intersecting the borehole in the middle. However, the fractures that do not cross the borehole are recognized with a lower probability (larger

uncertainty). Since the longer fractures have the highest influence on the stress heterogeneity (Valley et al. 2014), they are most accurately located within the domain. Now, we choose a random DFN from the selected range and compute the stress profiles ( $\sigma_1$  and  $\beta$ ) at the borehole along  $X = 0$ . Figure 4-8a and Figure 4-8b compare the stress profiles of this DFN with that of the original DFN. The close match between the two stress profiles is similar also for the other realizations of the ensemble, and it demonstrates successful inversion.

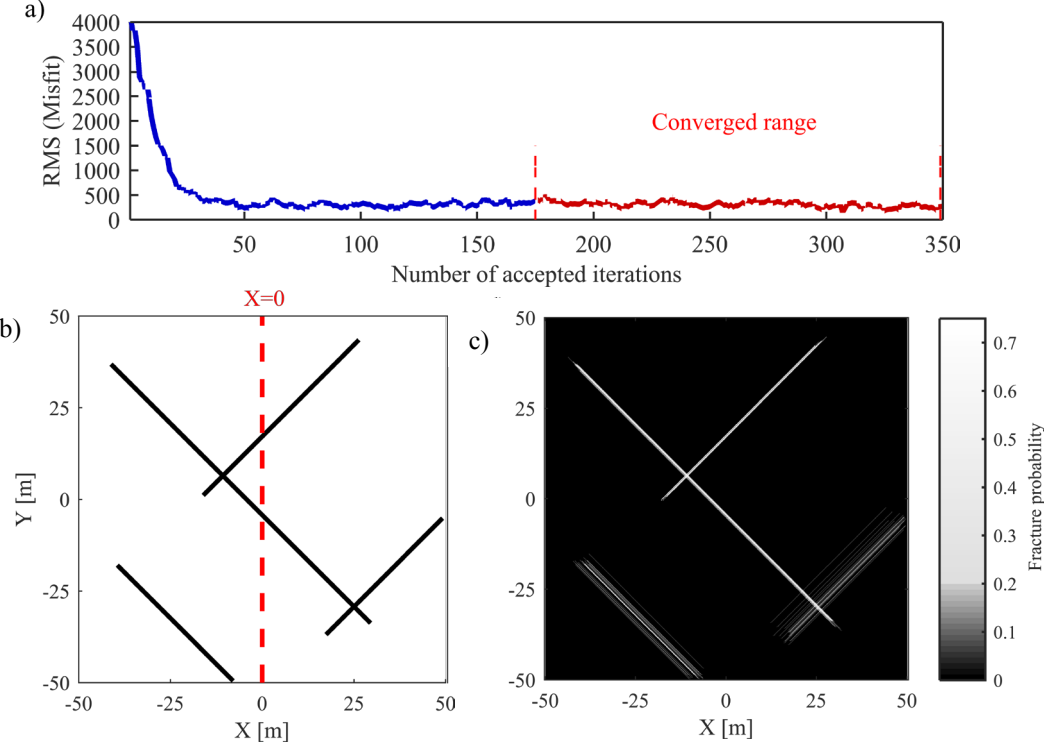


Figure 4-7. (a) Misfit evolution of all accepted realizations during the MCMC sampling. The converged range is chosen to be between the 175th and 350th iteration. (b) The initial simple synthetic network; (c) The fracture probability map of the 50 best fit realizations in the ensemble.

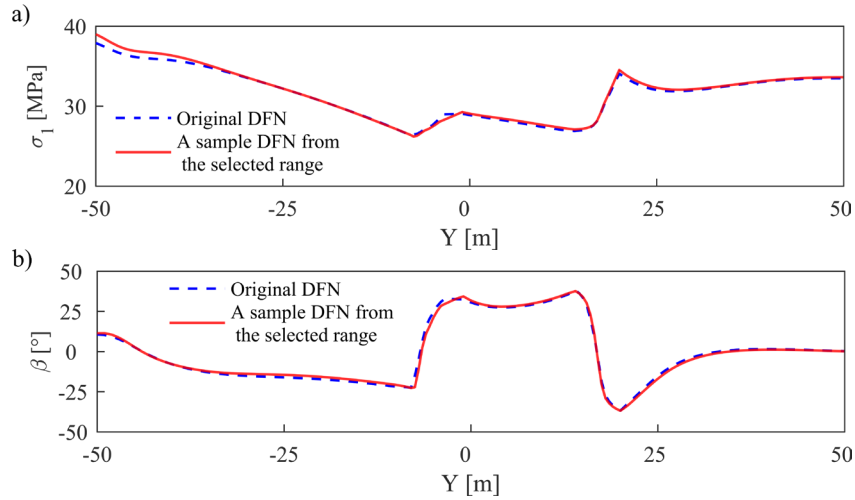


Figure 4-8. (a) Profiles of stress magnitude  $\sigma_1$  and (b) orientation  $\beta$  at the borehole for the simple synthetic case (Figure 4-4c, 4-4d) compared to profiles at the same location of a randomly chosen DFN from the selected range in Figure 4-7b.

#### 4.5.2 Out-crop based case

The inversion of the outcrop-based network (Figure 4-5b) was initiated by sampling from a power-law length distribution in a domain of  $50 \times 40 \text{ m}^2$ . We applied a probability density function of  $p(l) dl = 0.16 l^{-2.6} dl$  with a minimum length of 8 m. The initial DFN was generated using the key geometrical characteristics in Table 2. The locations of fractures were assumed to be distributed uniformly within the domain respecting the minimum spacing of each fracture set. The fractures belong to two main families with angles of  $-65^\circ$  and  $30^\circ$  from vertical (Table 2). Equivalent to the procedure for the synthetic case, the MCMC inversion procedure continuously moved the fractures in DFNs for 24 hours. The same inversion methodology was employed to reconstruct the DFN with the two stress profiles (i.e. observations) of Figure 4-6c and Figure 4-6d. The initial DFN for the inversion process of the simple synthetic case is presented in the supporting information (Appendix C).

Figure 4-9a depicts the evolution of misfit during the inversion process. The full MCMC sampling procedure accepted approximately 10,000 realizations. In comparison to the more straightforward synthetic case, the MCMC algorithm converged slower and required at least 1,000 iterations to achieve a relatively constant misfit. If half of the initial iterations are discarded, the converged range is between the 5,000<sup>th</sup> - 10,000<sup>th</sup> iterations. As the target DFN and the associated inversion problem became more complicated, the mean misfit of the converged range (684) became more than double that of the simple hypothetical case (311). Since the converged range consisted of many similar realizations and to accelerate visualization, the final ensemble was thinned.

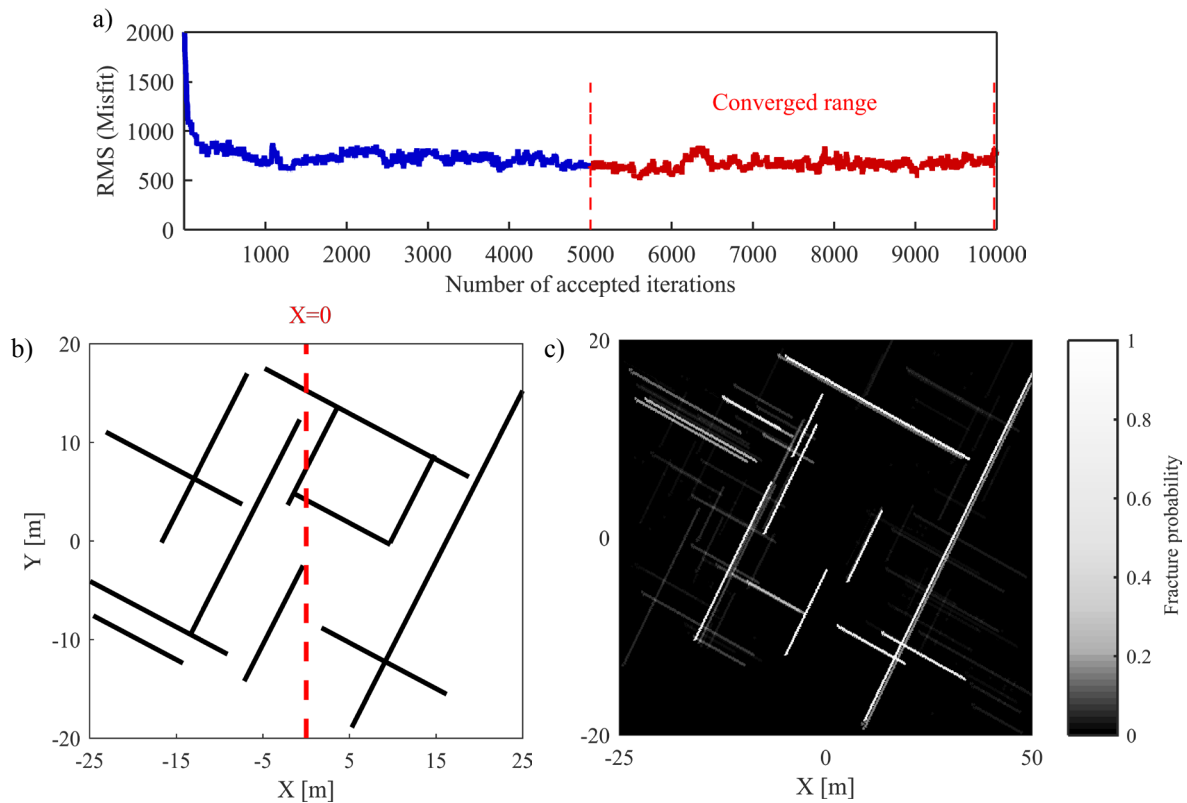


Figure 4-9. (a) MCMC convergence trend of accepted realizations for the outcrop-based fracture network; (b) original “true” network compared to (c) the corresponding fracture probability map obtained by inversion.

Figure 4-9b and Figure 4-9c compare the original DFN with the probability map. The probability map shows that the inversion again is sensitive to the most extended fractures. This is expected, because long fractures have a substantial impact on stress heterogeneities, even if they do not cut the borehole. Even though the probability map shows that also some smaller features are adequately imaged, some fractures are not well reconstructed or appear blurred in the map.

Figure 4-10a and Figure 4-10b compare the initial stress profiles of Figure 4-6c and Figure 4-6d with the profiles of an arbitrary realization of the final ensemble. There is a substantial similarity between the original and reproduced stress profile for both  $\sigma_1$  and  $\beta$ . However, because of the higher complexity, the match is not as excellent as for the synthetic case. The most considerable discrepancy is associated with the stress heterogeneity induced by a fracture tip at  $Y = -1.8$  m (black circle on the  $\sigma_1$  profile, Figure 4-9a). This is mainly due to the fracture tip, which is very close to the borehole and which affects more the profile of  $\sigma_1$  than of  $\beta$ . Although the location of this fracture has been identified in the probability map, its reconstructed length is not sufficient to generate a peak in the stress profile.



To reproduce stress variabilities comparable to the stress profiles in deep boreholes, we assumed a relatively low friction angle in both synthetic and outcrop-based fracture networks. Since the friction angle of crystalline rocks lies typically between 30-45°, we tested the inversion approach with a friction angle of 35° with the same inversion parameters (presented in Appendix C). The inversion results revealed that although the higher friction angles may result in less variability on the stress profiles, the corresponding stress variability still could reconstruct the significant features of the fracture network.

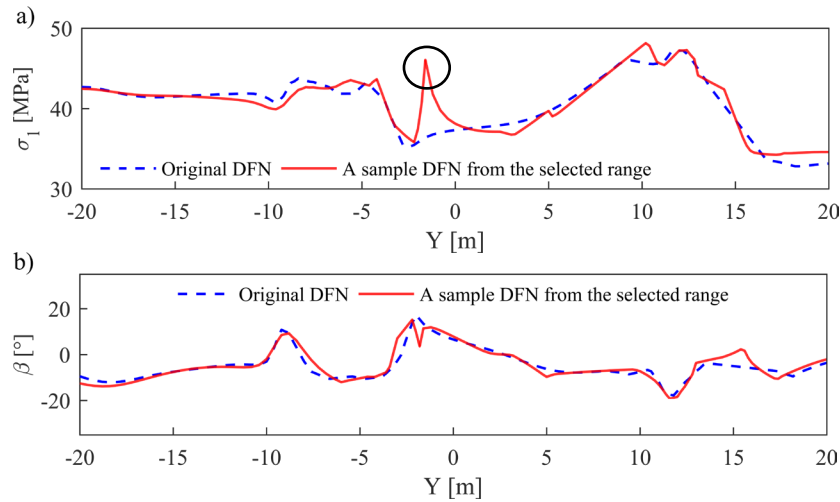


Figure 4-10. Stress profiles of initial outcrop-based model compared to those a randomly sampled DFN of the final ensemble: (a) variation of  $\beta$ , (b) a variation of  $\sigma_1$ . The black circle indicate the part of the stress profile highly affected by a fracture tip and which is not well reproduced.

#### 4.6 Discussion and conclusions

Fracture network characterization has been a challenge in many different engineering applications such as EGS developments. A robust recipe for extracting the fracture network geometry from available data including geological, geophysical and hydrogeological investigations is still lacking. However, stochastically generated fracture networks may be constrained by measured information. Borehole image logs provide valuable information on the fluctuations of in-situ stress components (e.g. maximum principal stress and its orientation) along the wellbore, if borehole breakouts or drilling induced tensile fractures are present. Since in-situ stress fluctuations are strongly influenced by the slip on natural fractures in the past, they also carry information on geometrical aspects of fracture networks. This is exploited in the presented example application based on a new Bayesian approach, also referred to as stress-based tomography, which flexibly adjusts fracture networks to match single borehole stress profiles.

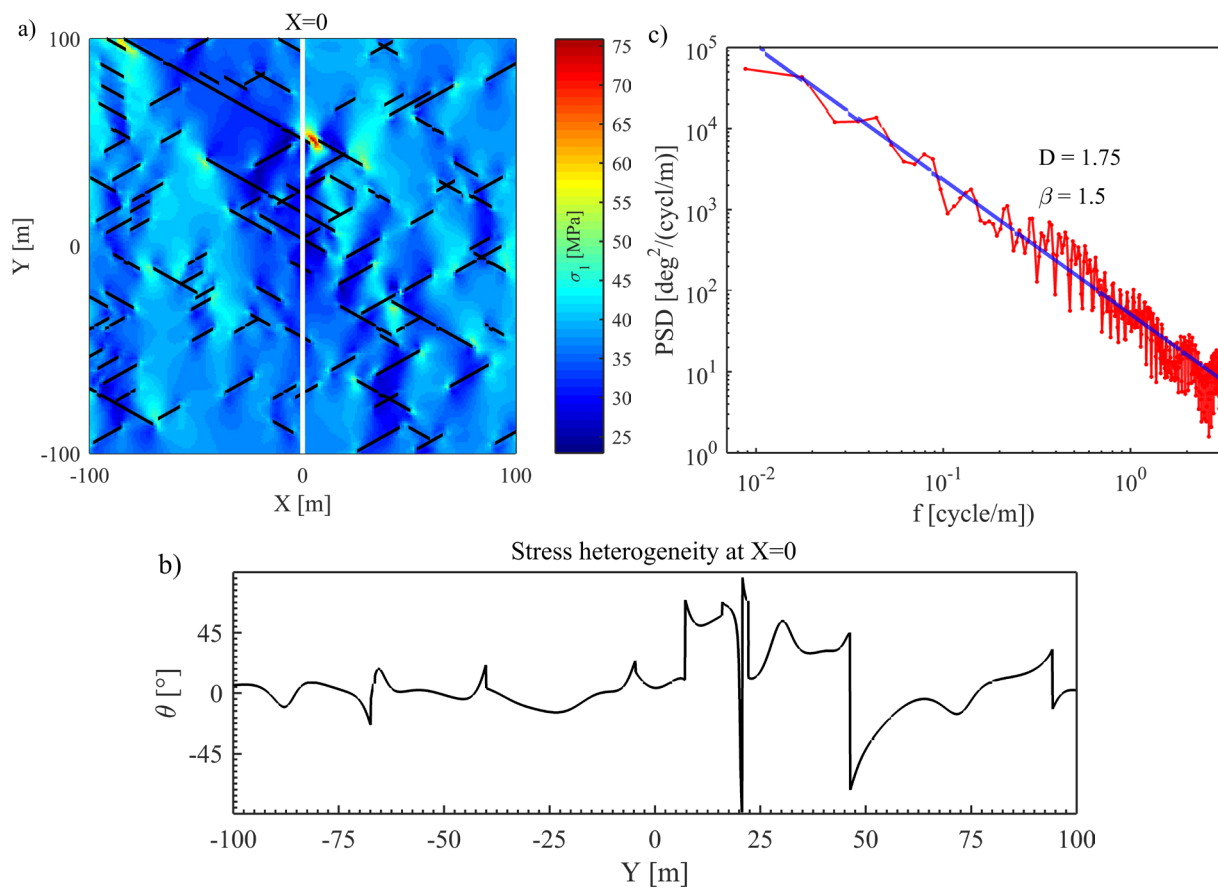
Comparing for the two examples the initial DFNs and the obtained probability maps reveals that significant features are accurately determined. Even if some fractures do not intersect the borehole, their impact may be significant on the observed stress heterogeneities. This effect is sufficient for imaging such relatively long “hidden” fractures in the vicinity of a borehole. This may not be enough for reconstructing smaller fractures if they are far from the borehole. Furthermore, in some instances, the probability map may not well resolve regions of higher local fracture intensity although roughly indicating the presence of such areas. Thus, this inversion methodology is more sensitive to longer fractures than to smaller ones. Note that, since larger fractures often represent the major pathways for fluid flow and yield higher seismic magnitudes, they are also more critical for case-specific performance, hazard and risk assessments.

One limitation of this approach originates from the difficulty to constrain the fracture strength properties such as normal and shear stiffness. Therefore, it is suggested to test different strength parameters before the inversion process and choose a reliable estimate based on the observation profiles. Analyzing the effect of these parameters on the inversion will be subject to future development of this approach.

One possible additional development of the presented stress-based tomography is to include further complementary field information such as tomographic information from geophysical measurements, tracer or hydraulic tomography (Brauchler et al. 2013; Dorn et al. 2011; Zha et al. 2015). Joint inversion of different data in the MCMC procedure could impose extra constraints on the generation of the probability maps. This could yield improved capabilities for reconstruction of more complex DFNs and of three-dimensional (3-D) features. In the presented approach, the prior knowledge of 2-D fracture length distribution is an input for the inversion process. However, this information may not be available. Since fracture length exponents in geological media are typically between 1.5 and 3.5, one option is to initialize (i.e. generate initial DFNs of) the MCMC algorithm with some length of exponents within this range. The length exponent associated with the lowest misfit would be most suitable for creating the probability map. Also, in the present implementation, the fracture intensity (i.e. fracture numbers) is assumed to be known a priori (by defining a constant  $c$  for the length distribution and a minimum length). Thus one further development of the presented approach is to implement a transdimensional inversion (Somogyvári et al. (2017)), in which the number of fractures is treated as a decision variable.

# 5 Preliminary analysis of the linkage between scaling of stress heterogeneities and fracture network

---



Afshari Moein M.J., Valley B., *Linkage between scaling of fracture network, stress heterogeneities and microearthquakes* (In Prep).



## **Abstract**

We analyzed the scaling characteristics of stress perturbations inferred from the image log runs in the borehole drilled into Basel geothermal reservoir, using Power spectral Density (PSD) methods and observed a linear PSD curve for wavelengths more than two orders of magnitude. Adopting the hypothesis that the stress perturbations are largely controlled by the slip on fracture surfaces, we studied the effect of fracture network characteristics on the scaling of stress heterogeneities in deep boreholes. Synthetic fracture networks following power-law length distributions were embedded in a geomechanical simulator and the stress heterogeneities were extracted on a vertical borehole in the study domain. Fracture network characteristics were calibrated to deliver fractal stress heterogeneities that are comparable to observations in deep boreholes such as Basel-1. Detailed analyses showed that if the fracture intensity is constant, the fractal dimension of stress profiles belong to a relatively large range between 1 and 2 with no significant correlation with fracture length exponent.

## **5.1 Introduction**

An increased interest to exploit the geothermal resources has raised the importance of developing Enhance Geothermal Systems (EGS) as a CO<sub>2</sub> emission-free source of energy. Circulation of a fluid (e.g. water) between the injection and production wells permit the heat exchange between the high temperature host rock and the fluid. Desirable temperatures of EGS developments (ideally higher than 150°) are typically found between 2 to 5 km depth below the ground level, where the permeability of the host rock is typically low. The major fraction of the permeability is provided by pre-existing natural fractures and faults (Davatzes and Hickman 2010; Dezayes et al. 2010; Genter et al. 2010), which is mostly not sufficient for commercial EGS developments (Saar 2011). Hydraulic stimulation (massive fluid injections) is a common technique to enhance or create the permeability within the target reservoir. This operation increases the permeability by shear dilation of rough surfaces or generating new fractures as probable fluid paths. However, this operation is not risk-free as it can in some situation generate felt earthquakes. This major challenge has been the obstacle in the development of EGS projects such as Basel and Saint-Gallen sites in Switzerland. Hence, the main objective of research in EGS developments is to optimize the stimulation parameters to enhance the permeability without inducing excessive seismic events.

In order to study the sensitivity of the different operational parameters on hydraulic stimulation, thermo-hydro-mechanical (THM) models are applied. The numerical models require a geological model (as an input), which include a realistic representation of geological features

such as fractures and faults. Although some deterministic elements of the fracture network may be defined by borehole data, there is not sufficient information on the entire 3D structures in the reservoir. Thus, stochastic representation of fracture networks known as Discrete Fracture Networks (DFN) are generated based on the statistical distribution of different fracture attributes. Power-law scaling has been widely applied to characterize different fracture properties such as spacing, clustering, length distribution, roughness (e.g. Moein et al. 2018; Barton and Zoback 1992; Bonnet et al. 2001; Bour et al. 2002; Power and Tullis 1991). Power-law scaling allows definition of rock mass properties in different scales.

In-situ stress heterogeneities observed from analyses of borehole failure are often interpreted as due to slip on fracture and faults (e.g. Blake and Davatzes 2011; Davatzes and Hickman 2010; Evans et al. 2005c; Hickman and Zoback 2004; McNamara et al. 2015; Shamir and Zoback 1992; Valley and Evans 2007a; Yale 2003). Adopting this hypothesis, Moein et al. (in prep.) introduced a probabilistic stress-based tomography to reconstruct the fracture network using the stress profiles along deep boreholes. However, these heterogeneities may result from other sources such as lithology changes (Wileveau et al. 2007), stiffness variation associated with fault damage zone (Lockner et al. 2000) and magmatic intrusions (Vigneresse et al. 1999). Stress heterogeneity largely impacts the earthquake dynamics (e.g. Hsu et al. 2010) and aftershock behavior (e.g. Hardebeck 2010). Stress variability along deep boreholes show self-affine scaling, which also may be characterized by power-laws (Blake and Davatzes 2012; Day-Lewis et al. 2010; Valley and Evans 2014b). Currently, the direct relations amongst power-law scaling of stress heterogeneities at borehole scale, fracture networks and potential links to the induced seismicity are not understood. Clarification of these potential relations may apply to constrain the DFN realizations with the information on stress heterogeneities along the borehole and possibly forecast the seismogenic parameters of the reservoir.

In the current research, we aim to gain a fundamental understanding of the stress heterogeneities within a complex DFN and relate the scaling of stress and earthquakes to key characteristics of the network. Adopting the hypothesis that simple slip on fractures controls the stress variability, we utilize a geomechanical code to model the stress heterogeneity in synthetic networks. We evaluate the self-affinity of the resulting stress and evaluate the characteristic fractal parameters of generated stress profile by computing power spectrum. We perform a sensitivity analyses on the scaling of stress with different DFN characteristics such as power-law length exponent, fracture intensity (i.e. the length of fractures per unit sampling area) and minimum fracture length. Finally, we propose a simple methodology to estimate the magnitude of the associated

earthquakes and study the effects of fracture network characteristics and scaling of stress heterogeneities on the estimates of b-value.

## **5.2 Power-law scaling**

Power-law scaling is commonly observed in natural systems, including in the distribution of key characteristics of rock masses (e.g. Afshari Moein et al. 2018; Mittag 2003; Sahimi et al. 1993; Scholz 1982). The reason of such a power-law nature is not completely understood, whereas the statistical scaling of complex self-organized critical dynamics has been proposed to be a possible explanation. Fractal statistics has been widely applied to characterize fracture network attributes, stress variability and earthquakes. Here, we review the scaling phenomena in these three closely related geological disciplines.

### **5.2.1 Fracture network**

Before reviewing the evidence of the scaling of fracture networks, we mention the possible sources of information on the fracture network in geological formations. For deep projects, the initial source of information stems from borehole data. Borehole image logs or cores provide information on the location and orientation of fractures that allow the definition of fracture sets (i.e. fractures belonging to same orientation families) as well as 1D spacing or spatial distribution of fractures (Moein et al. 2016; Ziegler et al. 2015). However, extracting the 3D statistical distribution of fracture attributes from these resources is not possible without additional and independent constraints and is commonly associated with large uncertainties. Particularly, fracture length distribution is one of the major sources of uncertainty, which has a relatively large impact on the connectivity of fractured rock (Darcel et al. 2003c) and possibly controls the frequency size distribution of induced events during hydraulic stimulations (Evans 2005). Additional information can be gained if the target formations are outcropping. Indeed, in such situations, 2D fracture network maps (Bour et al. 2002), or even in some exceptional cases, 3D maps (Srivastava 2006) can be generated allowing for exploring the characteristics of the fracture networks. Even if practically not available in the cases of deep geothermal projects, such 2D or 3D fracture maps have been central in the development of conceptual and mathematical models capturing the key characteristics of fracture networks.

Power-laws as the only scale invariant statistical distribution have been largely applied to characterize fracture length distributions (Bour et al. 2002; Davy et al. 1990a; de Dreuzy et al. 2002; Lei et al. 2015; Odling et al. 1999). In general, the fracture length of fractures from different observations follow a power-law length distribution such as equation 5.1,

$$n(l) = \alpha l^{-a} dl \quad (5.1)$$

where,  $n(l)$  is the number of fracture lengths between  $l$  and  $l + dl$  with a length exponent of  $a$  and a normalization constant of density  $\alpha$  (Bonnet et al. 2001). The values of fracture length exponent for 2D fracture outcrops typically vary between 1.5 and 3.5 (Bonnet et al. 2001).

### 5.2.2 Stress heterogeneities

Measuring stresses in deep borehole is challenging, and no single method exists to characterize all stress components from one set of data. Moreover, stress measurements are typically point measurements – or more precisely involve a limited rock mass volume over which an average stress state is estimated – and thus are not well suited to evaluate stress variability. However, if wellbore failure is sufficiently pervasive, it can provide almost continuous profiles of the principal stress orientation in the plane perpendicular to the wellbore. Such profiles allow characterizing the heterogeneities of stress orientation. These stress heterogeneities may follow self-affine scaling relationships (Turcotte and Huang 1995; Valley and Evans 2014a). Langenbruch and Shapiro (2014) has related this self-affinity to the elastic heterogeneity observed in Earth's crust. However, power-law fracture length distribution may also be the origin of the fractal nature of stress heterogeneities.

An evaluation of different techniques to estimate the scaling relationships of stress orientation variation series have been performed by Valley and Evans (2014a). They suggest that the most reliable estimate of the fractal dimension of such series is obtained by the computation of the power spectrum density (PSD) using Fast Fourier transform (FFT). If the series is fractal, the PSD represented in a log-log scale will be linear over multiple order of magnitudes and thus is proportional to  $(\frac{1}{f})^\beta$ , where  $f$  is the frequency,  $\beta$  is the power spectral slope that is related to the fractal dimension ( $D$ ) through equation 5.2. In this chapter,  $D$  represents the scaling exponent of stress heterogeneities.

$$D = \frac{5 - \beta}{2} \quad (5.2)$$

For one-dimensional fractal signals, the slope  $\beta$  lies between 1 and 3 and the fractal dimension range from 1 to 2. We computed the PSD by first prefiltering the data with a Hamming window and then applying a matlab built-in standard Fast Fourier Transform (FFT). Gaps in the data series are simply filled by straight lines. Section averaging (also referred as Welch's method) is used to smooth the spectrum.



An example of this methodology extracted from the work of Valley and Evans (2014b) and Valley et al. (2016) is presented in Figure 5-1. Figure 5-1a shows the deviation from the mean orientation of the maximum principal stress  $S_{hmax}$  and its variability along the Basel borehole. A few gaps (less than 20%) are visible in this data and are filled by straight lines. The stress orientation sampled every 0.4 m.

Figure 5-1b represents the corresponding PSD analysis of the Basel stress orientation data, which shows a slope  $\beta$  of -1.5 with a fractal dimension  $D$  of 1.75, which is valid for wavelengths between 1 m and slightly larger than 100 m (frequencies between 1 and 0.01 cycle/m).

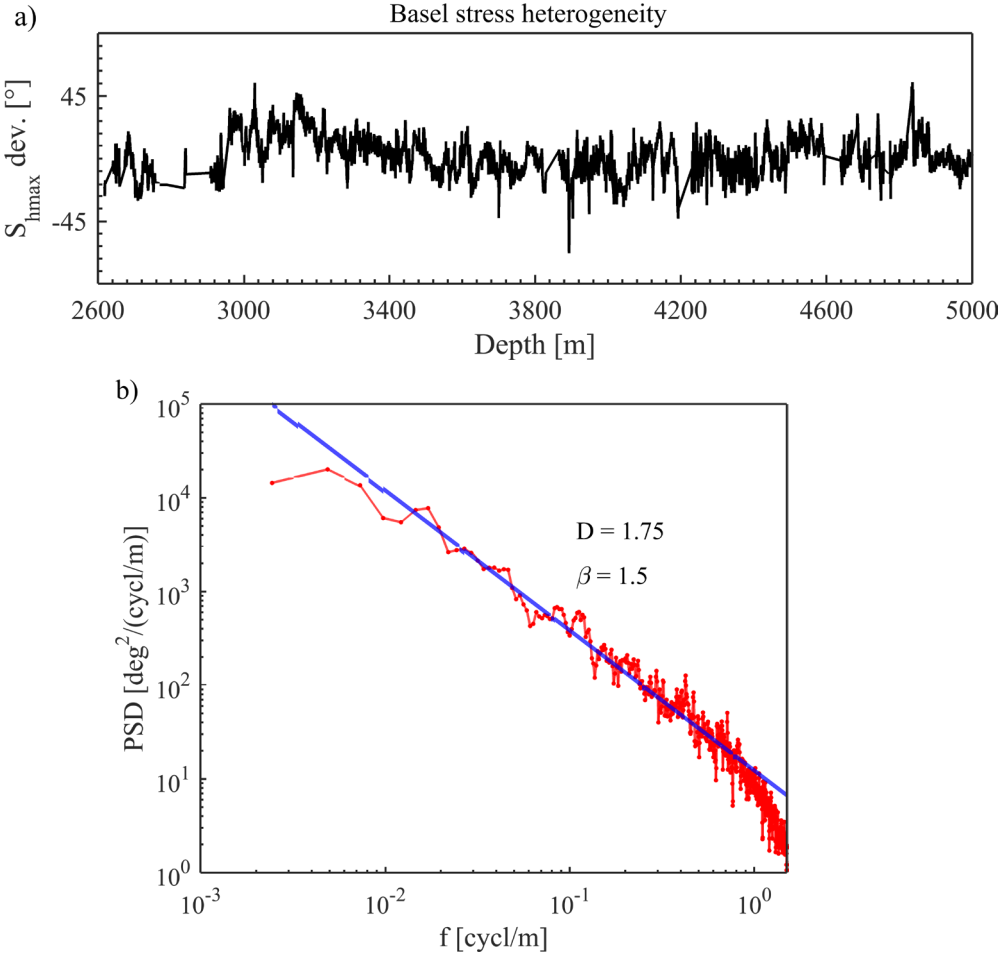


Figure 5-1. (a) Orientation of maximum principal horizontal stress  $S_{hmax}$  derived from borehole breakouts and axial drilling induced tension fractures observed in Basel-1 well. The orientation of each breakout leg is averaged for each sampling point (every 40 cm) and then subtracted from the average orientation along the borehole. The logged interval is between 2600-5000 m. (b) PSD function using FFT with a pre-filtering with Hanning window derived for the data provided in a. This figure defines a slope of -1.5 between 1 and 0.01 cycle/m (wavelengths of 1 and 100 m) implying a fractal dimension  $D = 1.75$ .

### 5.2.3 Microearthquakes

Microearthquakes also exhibit power-law frequency size distribution, following the famous Gutenberg Richter (Gutenberg and Richter 1954) relation as in equation 5.3,

$$\log N = a - bM \quad (5.3)$$

where,  $N$  is the total number of earthquakes with magnitude higher than  $M$ , while  $a$  and  $b$  serving as two constants. The slope  $b$ , often referred to b-value, shows the relative size distribution of earthquakes.

If the average displacement on a failure patch with an area of  $A$  is  $d$  and  $\mu$  is the shear strength of failure plane, the corresponding seismic moment  $M_0$  is defined using equation 5.4 and related to the moment magnitudes ( $M_w$ ) through equation 5.5 (Kanamori and Anderson 1975).

$$M_0 = \mu \cdot A \cdot d \quad (5.4)$$

$$M_w = \frac{2}{3} (\log(M_0) - 16.1) \quad (5.5)$$

## 5.3 Methodology

The general methodology developed here is to use a geomechanical simulator to generate a heterogeneous 2D stress field induced by slip on pre-existing fractures. Then, the key characteristics of the fracture networks and the resulting stress field can be compared. In addition, the average displacement and stress drop computed on fracture can be used to evaluate potential seismic local magnitude  $M_w$  associated with the slip on fractures (assuming that all slip are occurring in a seismic manner) using equations 5.4-5.5. This allow to compute the seismogenic parameters such as b-value and to compare it to scaling of stress and fracture network characteristics. However, the induced seismicity computation is not covered in this chapter.

Developing this approach without any constraints is not tractable because it includes many degrees of freedom (far field stress, fracture network geometry, mechanical properties of the medium and fractures,...). In order to develop our case on realistic and practical parameters, we generate our reference scenario using conditions and properties similar to those encountered in the Basel geothermal project.

Other constraints on our analyses are also imposed by the capabilities of available geomechanical simulators. One limitation is that robust and efficient modeling of 3D fracture networks is not available at the moment. This is a limitation that arises not only from

computational power requirements but also raises fundamental questions such as how to mechanically treat 3D fracture intersections. For these reasons, we develop our analyses using a 2D simulator ignoring the fracture intersection. Other constraints arise from the resolution of the model required to generate fractal signals that by definition must be valid over multiple order of magnitudes. We set ourselves the realistic objective of generating signals that hold fractal characteristics over two order of magnitudes going from 1 m to 100 m. Currently, computational restrictions hinder further extension to more than two orders of magnitude. With respect to these limitations, a study domain of  $200 \times 200 \text{ m}^2$  is chosen to generate synthetic fracture networks. Further details on the implementation of this methodology comes in the following sections.

### 5.3.1 Assumptions

We treat the problem as a 2D plane strain case with an isotropic, homogeneous and elastic rock mass penetrated by a fracture network. The fractures are Mohr-Coulomb elasto-plastic intersecting perpendicularly the model plane. The 1D profile (borehole) along which stress is sampled is contained in the model plane. According to the working hypothesis, in-situ stress variations along the borehole is a result of successive slips and deformations on the fracture planes over geological history. To keep the problem tractable, the stress variability will be assumed to occur due to the application of a single far-field stress state.

### 5.3.2 DFN generation

The geomechanical simulator imposes constraints on the length and spacing of fractures in order to avoid discretization problems and numerical instabilities. For this reason, we did not use the multiplicative cascade method presented in Chapter 2, but focused only on the fracture length distribution. The 2D synthetic fracture network realizations are generated by selecting random locations for fracture centers in the domain (i.e.  $200 \times 200 \text{ m}^2$ ). A length is attributed to each fracture center following a power-law length distribution as in equation 5.1. Fracture lengths are restricted to the range 10-50 m. Fracture orientations are chosen to reflect the conditions at the Basel geothermal project where there are two set of fractures forming a conjugate system. To generate mechanically consistent fracture networks, we also define a minimum spacing ( $s$ ) and minimum persistency ( $p$ ) for each fracture sets. When a fracture with a length of  $l$  is added, the DFN generator puts a rectangle as a stress shadow with the center corresponding to the fracture center, with side lengths of  $l + 2p$  and  $2s$ . The DFN generator is not allowed to subsequently populate any fractures from the same set that intersect this rectangle (other sets are permitted). The generator keeps populating new fractures until the cumulative

fracture length hits the input total fracture length. Due to the current computational limitations, the total length of fractures inside the domain may not exceed 800 m.

### 5.3.3 Modeling of stress variability

Here, we utilize a 2D geomechanical simulator with a displacement discontinuity method (DDM) developed by Jalali (2013). DDM approach is an indirect boundary element method, which is based on an analytical solution for the stress at a field point away from finite dislocation segment in an infinite body (Crouch et al. 1983; Salamon 1963). A detailed numerical implementation of this approach to mechanical modeling of fractured rocks has been presented by Jalali (2013).

The far-field stress imposed on the boundaries of the model and the fracture strength properties are selected in order to favor slip of fractures and thus to induce stress perturbations. For this reason, fractures are treated as cohesionless interfaces ( $c = 0$  MPa) with low friction angle of  $\phi = 10^\circ$ . Other parameters used in our model are listed in Table 5-1 and are based on the data collected at the Basel geothermal project.

### 5.3.4 Analyses of the generated stress field

The stress field is extracted along a vertical profile representing the borehole trajectory. The components of the stress tensor  $\sigma_{xx}$ ,  $\sigma_{yy}$  and  $\tau_{xy}$  are determined every 0.1 m along the profile. In order to be comparable with analyses that could be done on real data derived from borehole failure, we focus on the stress orientation variations. Here we are limited by our 2D plane strain configuration and can only analyze the deviation of the local principal stress direction from the far field principal stress direction. We define the parameter  $\theta$  that indicates the orientation of maximum principal stress from vertical borehole (positive clockwise) using equation;

$$\tan(2\theta) = \frac{2\tau_{xy}}{\sigma_{yy} - \sigma_{xx}} \quad (5.6)$$

where,  $\sigma_{yy}$  represents the local vertical normal stress,  $\tau_{xy}$  denotes the shear stress, and  $\sigma_{xx}$  is the horizontal normal stress along the borehole.

Table 5-1. Input parameters for modeling the stress variability using DDM approach. Tension positive convention is used for the stress magnitudes

Far-field principal stresses	minimum principal stress horizontal	$\sigma_3 = -20$ MPa
	maximum principal stress vertical	$\sigma_1 = -38$ MPa
Rock properties	Young's Modulus	$E = 60$ GPa
	Poisson's ratio	$\nu = 0.25$ MPa
Fracture network geometry	Fracture set orientation	$30^\circ, -30^\circ$
	Minimum spacing	5 m
	Minimum persistency	5 m
	Minimum length	10 m
	Total fracture length	500 m
Fracture properties	normal stiffness	$K_n = 10^{11}$ Pa/m
	shear stiffness	$K_s = 10^{10}$ Pa/m
	cohesion	$c = 0$ MPa
	friction angle	$\phi = 10^\circ$

Figure 5-2a represents the stress redistribution (e.g.  $\sigma_{yy}$ ) as a result of far-field stresses in a simple fracture network with a power-law length exponent of  $a = 3$ . All of the required information on the fracture network geometry, far-field stresses, rock and fracture physical properties are listed Table 5-1.

Figure 5-2b shows the stress orientation heterogeneity (variations of  $\theta$ ) on the borehole located at  $X = 0$  parallel to Y-axis. To ensure unbiased scaling analyses, the profile of  $\theta$  has been computed for approximately 2048 regularly spaced data points along this borehole. Due to computational limitations, the discretization of fractures is set to 2 m.

Figure 5-2c presents the PSD curve of the profile in Figure 5-2b, using the FFT with a pre-filtering of data using Hanning window. The resulting stress heterogeneity displays a linear PSD in wavelengths between 1-100 m with a local slope of  $\beta = 1.5$ , implying a fractal dimension of  $D = 1.75$ . The corresponding PSD curve is comparable to that of Basel-1 borehole presented in Figure 5-1b from which the model parameters were inspired for our reference scenario.

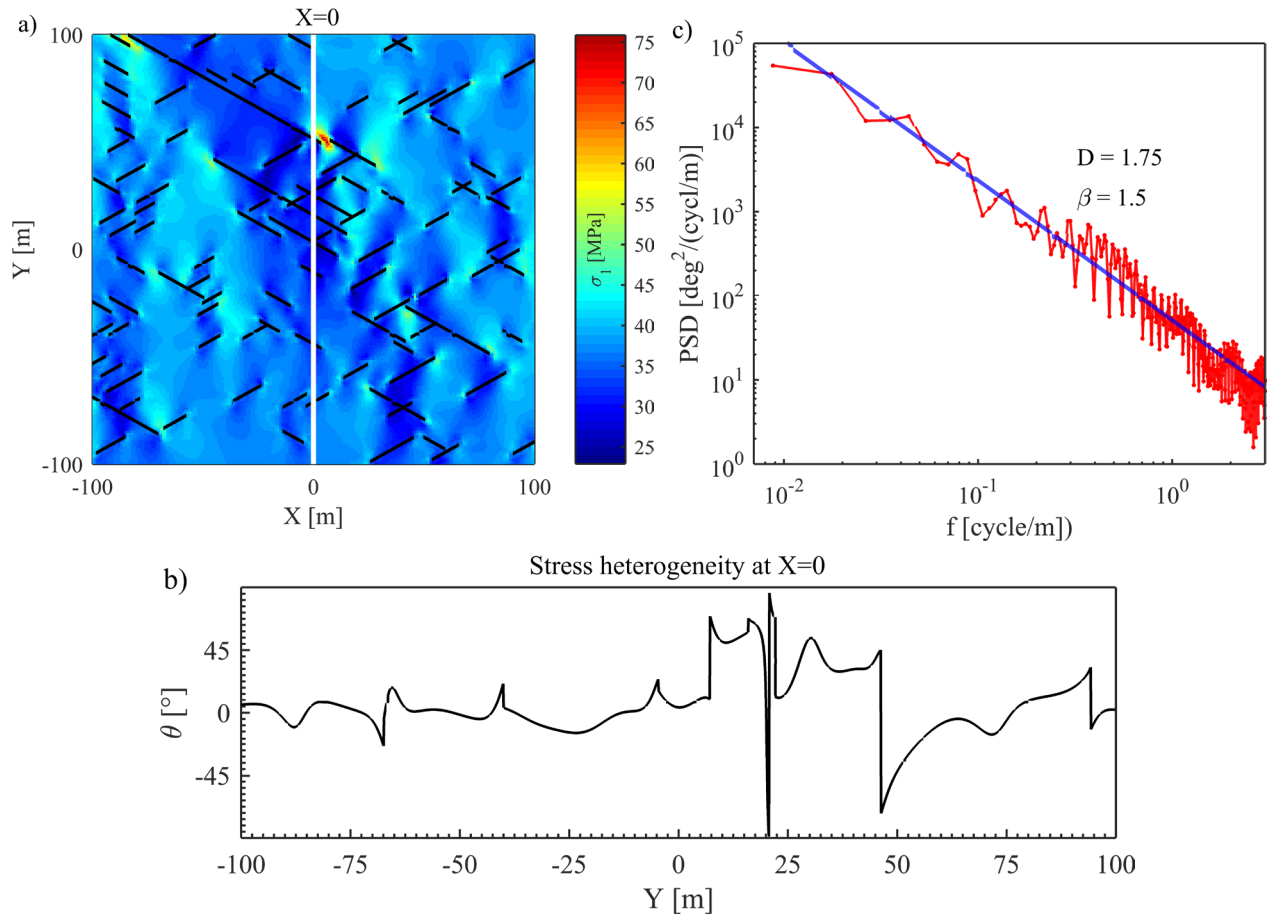


Figure 5-2. (a) Stress field as a result of applying far-field stresses and slip on fracture surfaces in the depicted fracture network with length exponent of  $\alpha=3$ . (b) Stress orientation heterogeneity  $\theta$ , on the borehole located at  $X=0$ , deviation from the average. (c) Power Spectral Density (PSD) plot of the stress profile in (b) using the FFT with pre-filtering of data using Hanning window.

## 5.4 Results of the parameter study

### 5.4.1 Relation between scaling of stress and fracture length exponent

Firstly, we explored the effect of fracture length exponent  $\alpha$  on the resulting stress variability and its scaling exponent ( $D$ ). Thus, synthetic networks (DFN realizations) with power-law exponents from 1.5-3.5 with steps of 0.25 were generated. To compare different realizations with different length exponents, the fracture intensity  $P_{21}$  was kept constant and equal to  $0.02 \text{ m}^{-1}$  (i.e. the total fracture length inside the domain is 800 m) for all of the realizations. For each length exponent, 100 random realizations were generated. For each realization a vertical borehole was located at the center of the study domain and the corresponding stress orientation profile  $\theta$  was computed with the methodology presented in section 3. Then, the resulting stress profiles were expressed in the frequency domain using FFT with Hanning window filtering. Figure 5-3a depicts the box-plot of  $D$  as a function of fracture length exponent  $\alpha$ . It is obvious

that the large variability of  $D$  does not imply a direct relation between  $D$  and  $a$ . However, a significant relation between the  $D$  and  $a$  was not resolved.

#### 5.4.2 Relation between scaling of stress and fracture intensity ( $P_{21}$ )

Fracture intensity is an important parameter, which impacts the mechanical response of a fractured rock mass. Thus, it is expected to influence the stress heterogeneities and its scaling  $D$ . We generated DFN realizations with the same power-law exponent of 3 but with different  $P_{21}$  values that range from  $0.005 \text{ m}^{-1}$  to  $0.02 \text{ m}^{-1}$  in steps of  $0.025 \text{ m}^{-1}$ . Because of computational restrictions in the DDM code, the value of  $P_{21}$  may not exceed  $0.02 \text{ m}^{-1}$ .

A similar procedure to the previous section was implemented and 100 DFN realizations with different values of  $P_{21}$  were generated. A vertical borehole was located in the center of each realization and  $\theta$  was computed along it. Then, profile of  $\theta$  was characterized using FFT with Hanning pre-filtering. Figure 5-3b displays the box-plot of the 100 realizations for each value of  $P_{21}$ . The large fraction of realizations are fractal except for  $P_{21} = 0.005$  and some outliers from other intensities.

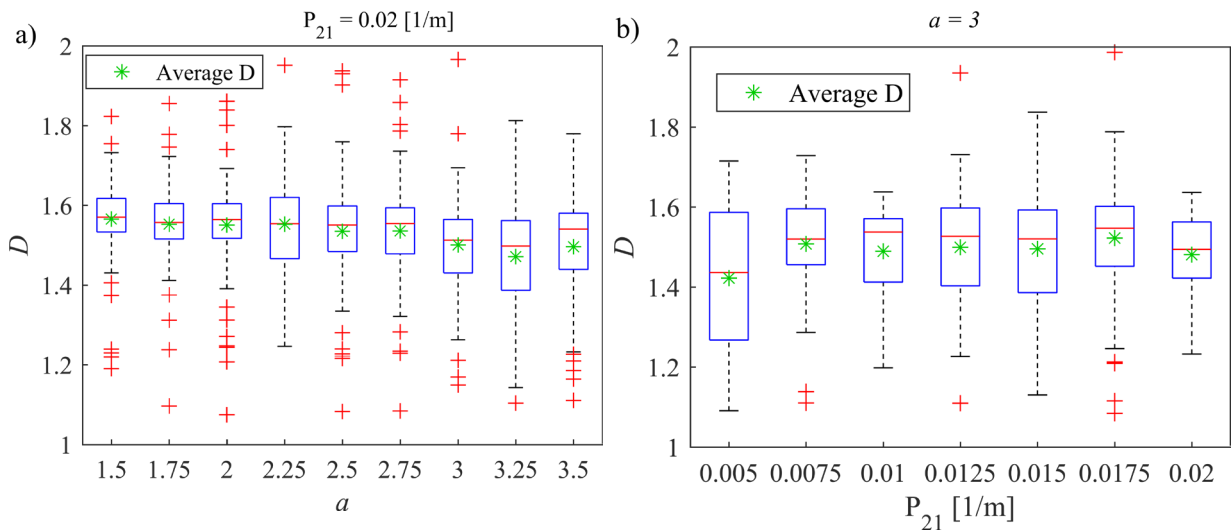


Figure 5-3. (a) Box-plot of  $D$  values of stress perturbations for each length exponent containing 100 realizations with the same fracture intensity  $P_{21}$  of  $0.02 \text{ m}^{-1}$ . DFN realizations are generated using the methodology described in section 5.3.2 with the simulation parameters listed in Table 5-1. (b) Box-plot of  $D$  values of stress perturbations for each fracture intensity  $P_{21}$  containing 100 realizations with the same length exponent  $a$  of 3.

#### 5.5 Discussion and conclusions

The analyses of stress orientation variability along the Basel geothermal borehole BS-1 suggest that the variation follow a fractal behavior over slightly more than two orders of magnitude from about 1m to 150 m with a dimension of 1.75 over this range (Valley and Evans 2009;

Valley and Evans 2014a). Since the local stress variations are mostly associated with fractures and faults, the fracture network characteristics such as fracture density and length distribution potentially influence the scaling characteristics of these stress perturbations. Thus, we adopted the hypothesis that local stress variations in boreholes are mainly generated by the slip on fractures, to quantify the impact of fracture network attributes on the scaling of stress heterogeneities.

We generated synthetic fracture networks following a power-law length distribution with uniformly distributed fracture centers. Fracture network characteristics (such as the area of the study domain, minimum and maximum fracture length) are calibrated to generate stress heterogeneities that are comparable to the data from Basel-1 borehole. In addition, the minimum fracture set spacing and persistency was defined to respect the fracture interactions during the nucleation process. An efficient and fast numerical code was employed to simulate the geomechanical response of the synthetic fracture networks to loading through application of far-field stresses at the model boundaries. The computation of the stress field and the probable failures with Mohr-Coulomb failure criterion resulted in slip on fractures. The stress redistribution permitted the extraction of stress heterogeneity on a single borehole in the study domain. Then, we applied the same methodology (i.e. FFT with a Hanning window pre-filtering) to characterize the scaling characteristics of resulting stress profiles. Here, we list the main conclusions attained from the current analysis:

1. The scaling characteristic of stress heterogeneity along a borehole is not necessarily similar to that of another borehole in a different location. This implies that the fractal dimension  $D$  of stress is dependent on the borehole location and is not a universal parameter of the fracture network. This observation was confirmed by observations made in two boreholes drilled Soultz-sou-e-Foret geothermal reservoir, where the fractal dimensions of stress heterogeneities were 1.68 and 1.75 for GPK3 and GPK4 (Valley and Evans 2014b), respectively.
2. If the fracture intensity is kept constant and the length exponent varies between 1.5-3.5, we computed the fractal dimension along a borehole located in the center of 100 realizations. The resulting fractal dimensions  $D$  for 99 percent of the realizations of any length exponent showed a relatively large possible range from 1 to 2.
3. If the fracture length exponent is kept constant and fracture intensity varies between 0.005-0.02  $\text{m}^{-1}$ , we computed the scaling exponent of 100 realizations along the borehole in the center. The fractal dimensions of stress profiles varied in a relatively large rang between 1 and 2. However, there were quite a few realizations, which the



corresponding scaling exponents of stress heterogeneities may not be fractal (i.e.  $D < 1$ ). At the moment, the research is going on to understand the reason of such  $D$  values less than 1. One possible explanation may be the discretization limitations and associated computational problems.

The conclusions are made with the resolution limitations and computational restrictions that were discussed. Thus, further analyses and developments require fast and efficient modeling of the stress heterogeneity in wavelengths more than two orders of magnitude. However, this chapter is presenting the preliminary results and will be further promoted in the following months. At this stage, we have not included the scaling of associated microearthquakes. Hence, one of the following steps would be to finalize the possible relations among the frequency size distribution of microearthquakes (b-value), fractal dimension of stress  $D$ , fracture intensity  $P_{21}$  and fracture length exponent ( $a$ ).



# 6 Conclusions and outlook

---

## 6.1 Conclusions

The primary objective of this thesis was to investigate the physical linkage between fracture network, stress variability and induced seismicity in the context of EGS technology. The initial working hypothesis of this work was that fracture network properties such as fracture length distribution control the stress variability and seismogenic response of rock mass to hydraulic stimulation. Evidence on scaling properties of these distinct concepts in self-organized critical systems supported this working hypothesis. This thesis has extensively explored these scaling relationships and opened opportunities for practical implications in geothermal reservoir characterization. However, not all of the chapters are developed based on the initial hypothesis.

The starting point of this study was to clarify the limitations of fracture network sampling and characterization from borehole datasets with a focus on the power-law scaling characteristics (Chapter 2). The study was supported by synthetic fracture networks that were generated using dual power-law model. The investigation among different techniques presented in literature revealed that two-point correlation dimension is the best estimate of the fractal dimension of fracture patterns (i.e. fracture spacing) along deep boreholes drilled into Basel and Soultz-sous-Forêts EGS sites. This constitutes strong evidence that fracturing in rock masses penetrated by the wells follows a fractal organization, while no systematic variation of fractal dimension with depth was resolved in any of the studied boreholes. However, the scaling characteristics of 1D borehole data is not sufficient to constrain the 3D spatial distribution of fracture network using stereological relationships. It is evident that 1D sampling cannot be used to infer the three-dimensional properties of our target parameters such as spatial distribution of fracture centers and fracture length distribution. This limitation hinders the ability to verify the developed methodologies, even if more datasets from more sites were available. Nevertheless, the fundamental limitation on the validity of the initial working hypothesis does not affect the applicability of the practical tools developed in this thesis.

One can hope to overcome this limitation by working on synthetic datasets generated by stochastic models, known as discrete fracture networks (DFN). However, these DFNs must be constrained with other available sources of information such as induced microseismicity cloud and in-situ stress data derived from borehole image logs and well testing analysis.

One possible approach is to generate synthetic induced seismicity patterns that follow certain statistics. Detailed analysis of induced events in Basel EGS site showed the clustering and rupture size distribution of seismicity patterns were quite similar to that of the fracture networks (Chapter 3). Thus, dual power-law model was applied to present a statistical seismicity model, which may be calibrated by early seismicity patterns. This development provided a practical implication to forecast maximum magnitude during hydraulic stimulation as a function of perturbed volume. This model was capable to interpret the effect of microseismic specific influential factors including the effect of hypocentral location uncertainties, existence of a fault zone and repeating events on the observed spatial organization. However, the initiation of such a seismicity model requires the data from early seismicity (learning phase).

To overcome this restriction, one can generate synthetic catalogues using physical models developed in the context of thermo-hydromechanical (THM) modeling of fracture reservoirs. In such cases, a full control on all parameters at all dimension is principally possible. Nevertheless, the major limitation arises from the gap in the current state-of-the-art in geomechanical simulations. Indeed, in order to generate relevant datasets (i.e. earthquake catalogues) for fractal analyses, one should be able to run models that are valid over 3 to 4 order of length scale. This requires extremely fine resolutions that are demanding very long CPU times.

Although induced seismicity data provide some information that may reflect some geometrical aspects of the fracture network, this information becomes available only after the execution of hydraulic stimulation and thus is not available in time for stimulation design purposes. One possible approach is to constrain the DFNs using the probabilistic methods. Thus, stress-based tomographical approach was introduced based on Bayesian statistics, to constrain the fracture network geometry from stress heterogeneities inferred from image logs along deep boreholes (Chapter 4). The main working hypothesis of this approach is that the stress variability is a result of slip on fracture planes. Final visualization of the inversion results provided a probability map, showing that major features are accurately determined (for both simple synthetic and out-crop based DFNs). Although some fractures do not intersect the borehole, their impact may be significant on the observed stress heterogeneities. However, this impact is sufficient for imaging larger fractures. This may not be true for smaller fractures, if they are far from the borehole. Thus, the proposed methodology was sensitive to larger fractures compared to smaller ones. Since larger fractures provide the major path for the fluid flow and result in higher seismic magnitudes, they are critical for case-specific hazard and risk assessments. It is

evident that, developed methodology in Chapter 4 does not depend on the scaling relationships and is independent of this initial working hypothesis.

Another possible approach to constrain the DFN using stress data is to investigate analytical relations between the scaling exponents of stress variability (based on the initial hypothesis) along deep boreholes, scaling properties of 2D and 3D fracture network attributes (e.g. fracture length and location). The preliminary analyses (Chapter 5) showed that the scaling characteristics of stress heterogeneities along a 1D sampling line (borehole) cutting through a 2D fracture network is not a constant value and varies from one borehole location to another. The observations of spatial variation of the stress scaling is consistent with field at Soultz-sous-Forêt geothermal reservoir, where the fractal dimension obtained in closely located well GPK3 and GPK4 differs (Valley and Evans 2014b). Currently, the control on these variations is not fully understood and may be explained by the similarity to the non-uniqueness observed in stereological fractal relationships for fracture networks (Chapter 2).

furthermore, no well-established relations among the fractal dimension of stress perturbation, fracture length exponent, fractal dimension of fracture locations and fracture intensity is resolved. With the developed methodologies, we could generate models that were valid over about two order of magnitude, but only in a 2D plane strain configuration. Practical applications of this approach requires generating 3D mechanical models of the target rock mass with sufficient resolutions to generate fractal stress profiles in more than three orders of magnitude. However, this approach would largely benefit from 3D modeling capabilities as it has been currently tested only on 2D synthetic cases. A 3D geomechanical simulator would also enable verification of the approach with field data. However, robust and efficient geomechanical modeling tools are lacking and this objective is out of reach at the moment.

## 6.2 Outlook and perspective

Within this thesis, dual power-law model has been applied to generate synthetic fracture networks with fractal statistics (Chapters 1 and 2). However, the application of this model to study the mechanical properties of fractured rocks is difficult. Thus, a simplified algorithm of DFN generation with respect to simple mechanical rules was applied in Chapters 3 and 4. This indicates the necessity to develop DFNs with respect to mechanical interactions between fractures. One possible development of the work in chapter 1 is to perform stereological analysis using novel DFN generation algorithms such as the model presented by Davy et al. (2010).

The application of seismic forecast during injection presented in Chapter 3 also depends on the dual power-law model investigated in this thesis. The proposed approach may also be updated using novel DFN generation algorithms. Moreover, the proposed approach should be further tested on any injection induced seismic datasets. In this case, data stemming from underground laboratory experiment would be of value when available. Such dataset will be available from the ISC experiment at the Grimsel test site in the near future and will also be available from the new underground lab at Bedretto Tunnel. This gives excellent perspective to prolongate the work initiated in the thesis in the near future.

The concept of stress-based tomography has been presented to image the fracture network using stress variability. However, practical applications of this approach requires the development of the current geomechanical simulator (DDM approach) to three dimensions. Data collected in deep underground laboratories with extensive characterization of the stress field and fracture network could be an excellent opportunity to further develop and test the approach. Stress-based tomography may also be compared with other tomographical approaches such as thermal or tracer tomography. The future research can also focus on coupling all the information from hydraulic, thermal and mechanical aspects toward a full thermo-hydromechanical inversion of the fractured rock mass.

# Bibliography

---

- Achtziger-Zupančič P, Loew S, Mariéthoz G (2017) A new global database to improve predictions of permeability distribution in crystalline rocks at site scale *Journal of Geophysical Research: Solid Earth* 122:3513-3539
- Afshari Moein, M. J., Tormann, T., Valley, B., & Wiemer, S. (2018). Maximum magnitude forecast in hydraulic stimulation based on clustering and size distribution of early microseismicity. *Geophysical Research Letters*, 45, 6907–6917.  
<https://doi.org/10.1029/2018GL077609>
- Aki K (1965) Maximum likelihood estimate of  $b$  in the formula  $\log N = a - bM$  and its confidence limits *Bull Earthq Res Inst, Tokyo Univ* 43:237-239
- Allegre CJ, Lemouel JL, Provost A (1982) Scaling Rules in Rock Fracture and Possible Implications for Earthquake Prediction *Nature* 297:47-49 doi:DOI 10.1038/297047a0
- Amadei B, Stephansson O (1997) Rock stress and its measurement. Springer Science & Business Media,
- Amann F et al. (2017) The seismo-hydro-mechanical behaviour during deep geothermal reservoir stimulations: open question tackled in a decameter-scale in-situ stimulation experiment *Solid Earth Discussions* 2017:se-2017-2079
- Anderson EM (1951) The dynamics of faulting and dyke formation with applications to Britain. Hafner Pub. Co.,
- Aster RC, Borchers B, Thurber CH (2011) Parameter estimation and inverse problems vol 90. Academic Press,
- Bachmann CE, Wiemer S, Goertz-Allmann B, Woessner J (2012) Influence of pore-pressure on the event-size distribution of induced earthquakes *Geophysical Research Letters* 39

- Baecher GB, Lanney NA Trace length biases in joint surveys. In: 19th US Symposium on Rock Mechanics (USRMS), 1978. American Rock Mechanics Association,
- Baghbanan A, Jing LR (2007) Hydraulic properties of fractured rock masses with correlated fracture length and aperture International Journal of Rock Mechanics and Mining Sciences 44:704-719 doi:10.1016/j.ijrmms.2006.11.001
- Baisch S, Weidler R, Vörös R, Wyborn D, de Graaf L (2006) Induced seismicity during the stimulation of a geothermal HFR reservoir in the Cooper Basin, Australia Bulletin of the Seismological Society of America 96:2242-2256
- Bak P, Tang C, Wiesenfeld K (1988) Self-organized criticality Phys Rev A Gen Phys 38:364-374
- Barton CA, Zoback MD (1992) Self-similar distribution and properties of macroscopic fractures at depth in crystalline rock in the Cajon Pass Scientific Drill Hole Journal of Geophysical Research: Solid Earth (1978–2012) 97:5181-5200
- Barton CA, Zoback MD (1994) Stress perturbations associated with active faults penetrated by boreholes: Possible evidence for near-complete stress drop and a new technique for stress magnitude measurement Journal of Geophysical Research: Solid Earth 99:9373-9390
- Barton CA, Zoback MD, Burns KL (1988) In-situ stress orientation and magnitude at the Fenton geothermal site, New Mexico, determined from wellbore breakouts Geophysical Research Letters 15:467-470
- Bense V, Gleeson T, Loveless S, Bour O, Scibek J (2013) Fault zone hydrogeology Earth-Science Reviews 127:171-192
- Berkowitz B, Hadad A (1997) Fractal and multifractal measures of natural and synthetic fracture networks J Geophys Res-Sol Ea 102:12205-12218 doi:Doi 10.1029/97jb00304



- Berrone S, Canuto C, Pieraccini S, Scialò S (2017) Uncertainty quantification in Discrete Fracture Network models: stochastic geometry *Water Resources Research*
- Bertani R (2012) Geothermal power generation in the world 2005–2010 update report *geothermics* 41:1-29
- Blake K, Davatzes NC Crustal stress heterogeneity in the vicinity of Coso Geothermal Field, CA. In: *Proceedings, Thirty-Sixth Workshop on Geothermal Reservoir Engineering*, 2011. p 11
- Blake K, Davatzes NC Borehole image log and statistical analysis of FOH-3D, Fallon Naval Air Station, NV. In: *Proceedings, Thirty-Seventh Workshop on Geothermal Reservoir Engineering* Stanford University, Stanford, California, 2012.
- Boadu F, Long L The fractal character of fracture spacing and RQD. In: *International journal of rock mechanics and mining sciences & geomechanics abstracts*, 1994. vol 2. Elsevier, pp 127-134
- Bodin T, Sambridge M, Tkalčić H, Arroucau P, Gallagher K, Rawlinson N (2012) Transdimensional inversion of receiver functions and surface wave dispersion *Journal of Geophysical Research: Solid Earth* 117
- Bommer JJ et al. (2006) Control of hazard due to seismicity induced by a hot fractured rock geothermal project *Engineering Geology* 83:287-306
- Bonneau F, Caumon G, Renard P (2016) Impact of a stochastic sequential initiation of fractures on the spatial correlations and connectivity of discrete fracture networks *Journal of Geophysical Research: Solid Earth* 121:5641-5658
- Bonnet E, Bour O, Odling NE, Davy P, Main I, Cowie P, Berkowitz B (2001) Scaling of fracture systems in geological media *Reviews of Geophysics* 39:347-383  
doi:10.1029/1999RG000074
- Bour O, Davy P (1997) Connectivity of random fault networks following a power law fault length distribution *Water Resources Research* 33:1567-1583

- Bour O, Davy P (1998) On the connectivity of three-dimensional fault networks *Water Resources Research* 34:2611-2622
- Bour O, Davy P (1999) Clustering and size distributions of fault patterns: theory and *Geophys Res Lett* 26:2001-2004
- Bour O, Davy P, Darcel C, Odling N (2002) A statistical scaling model for fracture network geometry, with validation on a multiscale mapping of a joint network (Hornelen Basin, Norway) *Journal of Geophysical Research: Solid Earth* 107
- Brauchler R, Hu R, Hu L, Jiménez S, Bayer P, Dietrich P, Ptak T (2013) Rapid field application of hydraulic tomography for resolving aquifer heterogeneity in unconsolidated sediments *Water Resources Research* 49
- Brooks S, Gelman A, Jones G, Meng X-L (2011) *Handbook of markov chain monte carlo*. CRC press,
- Chilès J (1988) Fractal and geostatistical methods for modeling of a fracture network *Mathematical Geology* 20:631-654
- Clemo T, Smith L (1997) A hierarchical model for solute transport in fractured media *Water Resources Research* 33:1763-1783 doi:10.1029/97WR01005
- Cornet F, Bérard T A case example of integrated stress profile evaluation. In: 3rd International Symposium on Rock Stress, edited by K. Sugawara, Y. Obara, and A. Sato, 2003. pp 23-24
- Crouch SL, Starfield AM, Rizzo F (1983) Boundary element methods in solid mechanics *Journal of Applied Mechanics* 50:704
- Darcel, Bour O, Davy P (2003a) Cross-correlation between length and position in real fracture networks *Geophysical research letters* 30
- Darcel, Bour O, Davy P (2003b) Stereological analysis of fractal fracture networks *Journal of Geophysical Research: Solid Earth* 108:n/a-n/a doi:10.1029/2002JB002091

- Darcel, Bour O, Davy P, De Dreuzy J (2003c) Connectivity properties of two-dimensional fracture networks with stochastic fractal correlation *Water resources research* 39
- Darcel C (2002) *Corrélations dans les réseaux de fractures: caractérisation et conséquences sur les propriétés hydrauliques*. Université Rennes 1
- Davatzes NC, Hickman SH (2010) Stress, fracture, and fluid-flow analysis using acoustic and electrical image logs in hot fractured granites of the Coso geothermal field, California, USA
- Davies R, Foulger G, Bindley A, Styles P (2013) Induced seismicity and hydraulic fracturing for the recovery of hydrocarbons *Marine and Petroleum Geology* 45:171-185
- Davy, Le Goc R, Darcel C, Bour O, De Dreuzy J-R, Munier R (2010) A likely universal model of fracture scaling and its consequence for crustal hydromechanics *Journal of Geophysical Research: Solid Earth* 115
- Davy, Sornette A, Sornette D (1990a) Some consequences of a proposed fractal nature of continental faulting *Nature* 348:56-58
- Davy P (1993) On the frequency-length distribution of the San Andreas fault system *Journal of Geophysical Research: Solid Earth* 98:12141-12151
- Davy P, Sornette A, Sornette D (1990b) Some consequences of a proposed fractal nature of continental faulting *Nature* 348:56-58
- Day-Lewis A, Zoback M, Hickman S (2010) Scale-invariant stress orientations and seismicity rates near the San Andreas Fault *Geophysical Research Letters* 37:n/a-n/a  
doi:10.1029/2010gl045025
- de Dreuzy J-R, Davy P, Bour O (2001) Hydraulic properties of two-dimensional random fracture networks following a power law length distribution 1. Effective connectivity *Water Resources Research* 37:2065-2078

- de Dreuzy JR, Davy P, Bour O (2002) Hydraulic properties of two-dimensional random fracture networks following power law distributions of length and aperture *Water Resources Research* 38
- Deere D, Deere D The rock quality designation (RQD) index in practice. In: *Symposium on Rock Classification Systems for Engineering Purposes*, 1987, Cincinnati, Ohio, USA, 1988.
- Deichmann N, Kraft T, Evans KF (2014) Identification of faults activated during the stimulation of the Basel geothermal project from cluster analysis and focal mechanisms of the larger magnitude events *Geothermics* 52:84-97
- Dershowitz W, Lee G, Geier J, Hitchcock S, La Pointe P (1993) *FracMan user documentation* Golder Associates Inc, Seattle WA
- Dezayes C, Genter A, Valley B (2010) Structure of the low permeable naturally fractured geothermal reservoir at Soultz *Comptes Rendus Geoscience* 342:517-530  
doi:<https://doi.org/10.1016/j.crte.2009.10.002>
- Dorbath L, Evans K, Cuenot N, Valley B, Charléty J, Frogneux M (2010) The stress field at Soultz-sous-Forêts from focal mechanisms of induced seismic events: Cases of the wells GPK2 and GPK3 *Comptes Rendus Geoscience* 342:600-606  
doi:<https://doi.org/10.1016/j.crte.2009.12.003>
- Dorn C, Linde N, Le Borgne T, Bour O, Baron L (2011) Single-hole GPR reflection imaging of solute transport in a granitic aquifer *Geophysical Research Letters* 38
- Dreuzy JR, Méheust Y, Pichot G (2012) Influence of fracture scale heterogeneity on the flow properties of three-dimensional discrete fracture networks (DFN) *Journal of Geophysical Research: Solid Earth* 117
- Dyer BC, Schanz U, Spillmann T, Ladner F, Häring MO (2010) Application of microseismic multiplet analysis to the Basel geothermal reservoir stimulation events *Geophysical Prospecting* 58:791-807 doi:[10.1111/j.1365-2478.2010.00902.x](https://doi.org/10.1111/j.1365-2478.2010.00902.x)

- Edwards B, Kraft T, Cauzzi C, Kästli P, Wiemer S (2015) Seismic monitoring and analysis of deep geothermal projects in St Gallen and Basel, Switzerland *Geophysical Journal International* 201:1022-1039
- Ellsworth WL (2013) Injection-induced earthquakes *Science* 341:1225-942
- Eshelby JD The determination of the elastic field of an ellipsoidal inclusion, and related problems. In: *Proceedings of the Royal Society of London A: Mathematical, Physical and Engineering Sciences*, 1957. vol 1226. The Royal Society, pp 376-396
- Evans, Genter A, Sausse J (2005a) Permeability creation and damage due to massive fluid injections into granite at 3.5 km at Soultz: 1. Borehole observations *Journal of Geophysical Research: Solid Earth* 110
- Evans et al. (2005b) Microseismicity and permeability enhancement of hydrogeologic structures during massive fluid injections into granite at 3 km depth at the Soultz HDR site *Geophysical Journal International* 160:388-412 doi:10.1111/j.1365-246X.2004.02474.x
- Evans K (2015) Reservoir creation. In: Hirschberg S, Wiemer S, Burgherr P (eds). vdf Hochschulverlag, p 118. doi:10.3218/3655-8
- Evans KF (2005) Permeability creation and damage due to massive fluid injections into granite at 3.5 km at Soultz: 2. Critical stress and fracture strength *Journal of Geophysical Research: Solid Earth* 110
- Evans KF, Cornet FH, Hashida T, Hayashi K, Ito T, Matsuki K, Wallroth T (1999) Stress and rock mechanics issues of relevance to HDR/HWR engineered geothermal systems: review of developments during the past 15 years *Geothermics* 28:455-474 doi:[http://dx.doi.org/10.1016/S0375-6505\(99\)00023-1](http://dx.doi.org/10.1016/S0375-6505(99)00023-1)
- Evans KF, Genter A, Sausse J (2005c) Permeability creation and damage due to massive fluid injections into granite at 3.5 km at Soultz: 1. Borehole observations *Journal of Geophysical Research: Solid Earth* 110

- Evans KF et al. (2005d) Microseismicity and permeability enhancement of hydrogeologic structures during massive fluid injections into granite at 3 km depth at the Soultz HDR site *Geophysical Journal International* 160:388-412 doi:10.1111/j.1365-246X.2004.02474.x
- Evans KF, Zappone A, Kraft T, Deichmann N, Moia F (2012) A survey of the induced seismic responses to fluid injection in geothermal and CO<sub>2</sub> reservoirs in Europe *Geothermics* 41:30-54
- Fairhurst C (2003) Stress estimation in rock: a brief history and review *International Journal of Rock Mechanics and Mining Sciences* 40:957-973
- Ferrari F, Ziegler M, Apuani T, Loew S (2017) Geostatistical analyses of exfoliation and tectonic joint set spacing in alpine granites (Aar Valley, Switzerland) *Bulletin of Engineering Geology and the Environment*:1-24
- Gaucher E, Schoenball M, Heidbach O, Zang A, Fokker PA, van Wees J-D, Kohl T (2015) Induced seismicity in geothermal reservoirs: A review of forecasting approaches *Renewable and Sustainable Energy Reviews* 52:1473-1490
- Gelman A, Carlin JB, Stern HS, Dunson DB, Vehtari A, Rubin DB (2014) *Bayesian data analysis vol 2*. CRC press Boca Raton, FL,
- Gelman A, Carlin JB, Stern HS, Rubin DB (2004) *Bayesian data analysis*. Texts in statistical science series. Chapman & Hall/CRC, Boca Raton, FL,
- Genter A, Evans K, Cuenot N, Fritsch D, Sanjuan B (2010) Contribution of the exploration of deep crystalline fractured reservoir of Soultz to the knowledge of enhanced geothermal systems (EGS) *Comptes Rendus Geoscience* 342:502-516  
doi:<http://dx.doi.org/10.1016/j.crte.2010.01.006>
- Geyer C (2011) Introduction to markov chain monte carlo *Handbook of markov chain monte carlo* 20116022:45

- Ghassemi A (2012) A review of some rock mechanics issues in geothermal reservoir development *Geotechnical and Geological Engineering* 30:647-664
- Giardini D (2009) Geothermal quake risks must be faced *Nature* 462:848  
doi:10.1038/462848a
- Gillespie P, Howard C, Walsh J, Watterson J (1993) Measurement and characterisation of spatial distributions of fractures *Tectonophysics* 226:113-141
- Gischig VS, Wiemer S (2013) A stochastic model for induced seismicity based on non-linear pressure diffusion and irreversible permeability enhancement *Geophysical Journal International* 194:1229-1249
- Goertz-Allmann BP, Goertz A, Wiemer S (2011) Stress drop variations of induced earthquakes at the Basel geothermal site *Geophysical Research Letters* 38:n/a-n/a  
doi:10.1029/2011GL047498
- Goertz-Allmann BP, Wiemer S (2012) Geomechanical modeling of induced seismicity source parameters and implications for seismic hazard assessment *Geophysics* 78:KS25-KS39
- Goff JA, Holliger K (1999) Nature and origin of upper crustal seismic velocity fluctuations and associated scaling properties: Combined stochastic analyses of KTB velocity and lithology logs *Journal of Geophysical Research: Solid Earth* 104:13169-13182
- Gutenberg B, Richter C (1954) *Seismicity of the earth and associated phenomena*. Princeton University Press,
- Hardebeck J (2010) Aftershocks are well aligned with the background stress field, contradicting the hypothesis of highly heterogeneous crustal stress *Journal of Geophysical Research: Solid Earth* 115
- Häring MO, Schanz U, Ladner F, Dyer BC (2008) Characterisation of the Basel 1 enhanced geothermal system *Geothermics* 37:469-495

- Harthong B, Scholtès L, Donzé F-V (2012) Strength characterization of rock masses, using a coupled DEM–DFN model *Geophysical Journal International* 191:467-480
- Hentschel H, Procaccia I (1983a) The infinite number of generalized dimensions of fractals and strange attractors *Physica D: Nonlinear Phenomena* 8:435-444
- Hentschel HGE, Procaccia I (1983b) The infinite number of generalized dimensions of fractals and strange attractors *Physica D: Nonlinear Phenomena* 8:435-444  
doi:[https://doi.org/10.1016/0167-2789\(83\)90235-X](https://doi.org/10.1016/0167-2789(83)90235-X)
- Hickman S, Zoback M (2004) Stress orientations and magnitudes in the SAFOD pilot hole *Geophysical Research Letters* 31
- Hickman S, Zoback M, Barton C, Benoit R, Svitek J, Summers R Stress and permeability heterogeneity within the Dixie Valley geothermal reservoir: Recent results from well 82-5. In: *Proceedings 25th Workshop on Geothermal Reservoir Engineering, 2000*. pp 256-265
- Hickman SH, Davatzes NC (2010) In-situ stress and fracture characterization for planning of an EGS stimulation in the Desert Peak Geothermal Field, Nevada
- Hirata T, Satoh T, Ito K (1987) Fractal structure of spatial distribution of microfracturing in rock *Geophysical Journal International* 90:369-374 doi:10.1111/j.1365-246X.1987.tb00732.x
- Hirschberg S, Wiemer S, Burgherr P (2014) *Energy from the Earth: Deep Geothermal as a Resource for the Future?* vol 62. vdf Hochschulverlag AG,
- Hsu Y-J, Rivera L, Wu Y-M, Chang C-H, Kanamori H (2010) Spatial heterogeneity of tectonic stress and friction in the crust: new evidence from earthquake focal mechanisms in Taiwan *Geophysical Journal International* 182:329-342
- Husen S (2010) Earthquake location accuracy CORSSA



- Illman WA, Liu X, Takeuchi S, Yeh TCJ, Ando K, Saegusa H (2009) Hydraulic tomography in fractured granite: Mizunami Underground Research site, Japan Water resources research 45
- Jalali M (2013) Thermo-Hydro-Mechanical Behavior of Conductive Fractures using a Hybrid Finite Difference–Displacement Discontinuity Method
- Jalali M, Valley B Hydromechanical and Thermomechanical Behaviour of Elastic Fractures during Thermal Stimulation of Naturally Fractured Reservoirs. In: EGU General Assembly Conference Abstracts, 2015. p 8370
- Jiménez S, Mariethoz G, Brauchler R, Bayer P (2016) Smart pilot points using reversible-jump Markov-chain Monte Carlo Water Resources Research 52:3966-3983
- Kanamori H, Anderson DL (1975) Theoretical basis of some empirical relations in seismology Bulletin of the Seismological Society of America 65:1073-1095
- Karra S, O'Malley D, Hyman J, Viswanathan H, Srinivasan G (2018) Modeling flow and transport in fracture networks using graphs Physical Review E 97:033304
- Kim TH (2007) Fracture characterization and estimation of fracture porosity of naturally fractured reservoirs with no matrix porosity using stochastic fractal models. Texas A&M University
- Kim Y-S, Sanderson DJ (2005) The relationship between displacement and length of faults: a review Earth-Science Reviews 68:317-334  
doi:<https://doi.org/10.1016/j.earscirev.2004.06.003>
- Kraft T, Deichmann N (2014) High-precision relocation and focal mechanism of the injection-induced seismicity at the Basel EGS Geothermics 52:59-73
- La Pointe P A method to characterize fracture density and connectivity through fractal geometry. In: International Journal of Rock Mechanics and Mining Sciences & Geomechanics Abstracts, 1988. vol 6. Elsevier, pp 421-429

- Langenbruch C, Shapiro SA (2014) Gutenberg-Richter relation originates from Coulomb stress fluctuations caused by elastic rock heterogeneity *Journal of Geophysical Research: Solid Earth* 119:1220-1234 doi:10.1002/2013JB010282
- Lecampion B, Lei T (2010) Reconstructing the 3D initial stress state over reservoir geomechanics model from local measurements and geological priors: a Bayesian approach *Schlumberger J of Modeling, Design, and Simulation* 1:100--104
- Ledésert B, Dubois J, Genter A, Meunier A (1993) Fractal analysis of fractures applied to Soultz-sous-Forêts hot dry rock geothermal program *Journal of Volcanology and Geothermal Research* 57:1-17
- Lee J, Kitanidis P (2013) Bayesian inversion with total variation prior for discrete geologic structure identification *Water Resources Research* 49:7658-7669
- Lei Q, Latham JP, Tsang CF, Xiang J, Lang P (2015) A new approach to upscaling fracture network models while preserving geostatistical and geomechanical characteristics *Journal of Geophysical Research: Solid Earth* 120:4784-4807
- Lin W, Yamamoto K, Ito H, Masago H, Kawamura Y (2008) Estimation of minimum principal stress from an extended leak-off test onboard the Chikyu drilling vessel and suggestions for future test procedures *Scientific drilling* 6:43-47
- Ljunggren C, Chang Y, Janson T, Christiansson R (2003) An overview of rock stress measurement methods *International Journal of Rock Mechanics and Mining Sciences* 40:975-989
- Lockner D, Naka H, Tanaka H, Ito H, Ikeda R Permeability and strength of core samples from the Nojima fault of the 1995 Kobe earthquake. In: *Proceedings of the international workshop on the Nojima fault core and borehole data analysis, 2000*. Citeseer, pp 22-23
- Lovejoy S, Schertzer D (1986) Scale invariance, symmetries, fractals, and stochastic simulations of atmospheric phenomena *Bulletin of the American meteorological society* 67:21-32

- Manning CE (1994) Fractal clustering of metamorphic veins *Geology* 22:335-338
- Mardia KV, Nyirongo VB, Walder AN, Xu C, Dowd PA, Fowell RJ, Kent JT (2007) Markov Chain Monte Carlo Implementation of Rock Fracture Modelling *Mathematical Geology* 39:355-381 doi:10.1007/s11004-007-9099-3
- McClure MW, Horne RN (2011) Investigation of injection-induced seismicity using a coupled fluid flow and rate/state friction model *Geophysics* 76:WC181-WC198
- McGarr A (2014) Maximum magnitude earthquakes induced by fluid injection *Journal of Geophysical Research: Solid Earth* 119:1008-1019
- McNamara DD, Massiot C, Lewis B, Wallis IC (2015) Heterogeneity of structure and stress in the Rotokawa Geothermal Field, New Zealand *Journal of Geophysical Research: Solid Earth* 120:1243-1262
- Meakin P (1991) Fractal aggregates in geophysics *Reviews of Geophysics* 29:317-354
- Merceron T, Velde B (1991) Application of Cantor's method for fractal analysis of fractures in the Toyoha Mine, Hokkaido, Japan *Journal of Geophysical Research: Solid Earth* 96:16641-16650
- Mignan A, Woessner J (2012) Estimating the magnitude of completeness for earthquake catalogs *Community Online Resource for Statistical Seismicity Analysis* doi:10.5078/corssa-00180805
- Mittag RJ (2003) Fractal analysis of earthquake swarms of Vogtland/NW-Bohemia intraplate seismicity *Journal of Geodynamics* 35:173-189
- Moeck I et al. The St. Gallen project: development of fault controlled geothermal systems in urban areas. In: *Proceedings World Geothermal Congress, 2015*.
- Moein M, Valley B, Ziegler M (2016) Preliminary fractal analysis of fracture spacing inferred from an acoustic televiewer log run in the Basel-1 geothermal well (Switzerland). In: *Rock Mechanics and Rock Engineering: From the Past to the Future*. CRC Press, pp 1103-1107

- Mondal A, Efendiev Y, Mallick B, Datta-Gupta A (2010) Bayesian uncertainty quantification for flows in heterogeneous porous media using reversible jump Markov chain Monte Carlo methods *Advances in Water Resources* 33:241-256
- Moriya H, Niitsuma H, Baria R (2003) Multiplet-clustering analysis for estimation of fine detail structures in seismic clouds at Soultz field, France *Bull seism Soc Am* 93:1606-1620
- Odling (1992) Network properties of a two-dimensional natural fracture pattern *Pure and Applied Geophysics* 138:95-114
- Odling et al. (1999) Variations in fracture system geometry and their implications for fluid flow in fractured hydrocarbon reservoirs *Petroleum Geoscience* 5:373-384
- Pierdominici S, Mariucci MT, Montone P (2011) A study to constrain the geometry of an active fault in southern Italy through borehole breakouts and downhole logs *Journal of Geodynamics* 52:279-289
- Pollard D, Segall P (1987) Theoretical displacements and stresses near fractures in rock: with applications to faults, joints, veins, dikes, and solution surfaces *Fracture mechanics of rock* 277:277-349
- Power WL, Tullis TE (1991) Euclidean and fractal models for the description of rock surface roughness *Journal of Geophysical Research: Solid Earth* (1978–2012) 96:415-424
- Preisig G et al. (2015) Development of connected permeability in massive crystalline rocks through hydraulic fracture propagation and shearing accompanying fluid injection *Geofluids* 15:321-337
- Rajabi M, Tingay M, King R, Heidbach O (2017) Present-day stress orientation in the Clarence-Moreton Basin of New South Wales, Australia: a new high density dataset reveals local stress rotations *Basin Research* 29:622-640
- Renshaw CE (1999) Connectivity of joint networks with power law length distributions *Water Resources Research* 35:2661-2670

- Roy A, Perfect E, Dunne WM, McKay LD (2014) A technique for revealing scale-dependent patterns in fracture spacing data *Journal of Geophysical Research: Solid Earth* 119:5979-5986
- Rutqvist J (2015) Fractured rock stress-permeability relationships from in situ data and effects of temperature and chemical-mechanical couplings *Geofluids* 15:48-66
- Rutqvist J, Oldenburg C Analysis of injection-induced micro-earthquakes in a geothermal steam reservoir, the Geysers Geothermal Field, California. In: *The 42nd US Rock Mechanics Symposium (USRMS)*, 2008. American Rock Mechanics Association,
- Saar MO (2011) Geothermal heat as a tracer of large-scale groundwater flow and as a means to determine permeability fields *Hydrogeology Journal* 19:31-52
- Sahara DP, Schoenball M, Kohl T, Müller BI (2014) Impact of fracture networks on borehole breakout heterogeneities in crystalline rock *International Journal of Rock Mechanics and Mining Sciences* 71:301-309
- Sahimi M, Robertson MC, Sammis CG (1993) Fractal distribution of earthquake hypocenters and its relation to fault patterns and percolation *Physical review letters* 70:2186
- Salamon M (1963) Elastic analysis of displacements and stresses induced by the mining of seam or reef deposits *Journal of the Southern African Institute of Mining and Metallurgy* 64:128-149
- Schmitt DR, Currie CA, Zhang L (2012) Crustal stress determination from boreholes and rock cores: Fundamental principles *Tectonophysics* 580:1-26  
doi:<http://dx.doi.org/10.1016/j.tecto.2012.08.029>
- Schoenball M, Davatzes NC (2017) Quantifying the heterogeneity of the tectonic stress field using borehole data *Journal of Geophysical Research: Solid Earth*
- Scholz CH (1982) Scaling laws for large earthquakes: Consequences for physical models *Bulletin of the Seismological Society of America* 72:1-14

- Scholz CH (2002) The mechanics of earthquakes and faulting. Cambridge university press,
- Shamir G, Zoback MD (1992) Stress orientation profile to 3.5 km depth near the San Andreas fault at Cajon Pass, California Journal of Geophysical Research: Solid Earth 97:5059-5080
- Shapiro SA, Krüger OS, Dinske C (2013) Probability of inducing given-magnitude earthquakes by perturbing finite volumes of rocks Journal of Geophysical Research: Solid Earth 118:3557-3575
- Somogyvári M, Jalali M, Jimenez Parras S, Bayer P (2017) Synthetic fracture network characterization with transdimensional inversion Water Resources Research 53:5104-5123
- Sornette D (2006) Critical phenomena in natural sciences: chaos, fractals, selforganization and disorder: concepts and tools. Springer Science & Business Media,
- Sornette D, Davy P, Sornette A (1990) Structuration of the lithosphere in plate tectonics as a self-organized critical phenomenon Journal of Geophysical Research: Solid Earth 95:17353-17361
- Spyropoulos C, Scholz CH, Shaw BE (2002) Transition regimes for growing crack populations Physical Review E 65:056105
- Srivastava M Field verification of a geostatistical method for simulating fracture network models. In: Golden Rocks 2006, The 41st US Symposium on Rock Mechanics (USRMS), 2006. American Rock Mechanics Association,
- Tafti TA, Sahimi M, Aminzadeh F, Sammis CG (2013) Use of microseismicity for determining the structure of the fracture network of large-scale porous media Physical Review E 87:032152
- Tester JW et al. (2006) The future of geothermal energy: Impact of enhanced geothermal systems (EGS) on the United States in the 21st century Massachusetts Institute of Technology 209

- Tezuka K, Watanabe K Fracture network modeling of Hijiori hot dry rock reservoir by deterministic and stochastic crack network simulator (D/SC). In: Proceeding World Geothermal Congress 2000, 2000.
- Torabi A, Berg SS (2011) Scaling of fault attributes: A review *Marine and Petroleum Geology* 28:1444-1460
- Townend J, Zoback MD (2000) How faulting keeps the crust strong *Geology* 28:399-402
- Tsang C-F, Figueiredo B, Niemi A (2018) Importance of stress effects on inputs to fracture network models used for subsurface flow and transport studies *International Journal of Rock Mechanics and Mining Sciences* 101:13-17
- Turcotte D, Huang J (1995) Fractal distributions in geology, scale invariance, and deterministic chaos. In: *Fractals in the earth sciences*. Springer, pp 1-40
- Valley (2007) The relation between natural fracturing and stress heterogeneities in deep-seated crystalline rocks at Soultz-sous-Forêts (France). Diss., Naturwissenschaften, Eidgenössische Technische Hochschule ETH Zürich, Nr. 17385, 2007
- Valley, Evans KF Stress state at Soultz-sous-Forêts to 5 km depth from wellbore failure and hydraulic observations. In: *Proceedings, 32nd Workshop on Geothermal Reservoir Engineering*, 2007a. pp 17481-17469
- Valley, Evans KF (2009) Stress orientation to 5 km depth in the basement below Basel (Switzerland) from borehole failure analysis *Swiss Journal of Geosciences* 102:467-480 doi:10.1007/s00015-009-1335-z
- Valley, Genter A Multi-scale fracturing in the Soultz-sous-Forêts basement from borehole image analyses. In: *Proceedings EHDRA Scientific Conference*, 2007.
- Valley B, Evans K (2014a) Preliminary assessment of the scaling relationships of in-situ stress orientation variations indicated by wellbore failure data, The 2014 ISRM European Rock Mechanics Symposium (EUROCK 2014). In: Alejano LR, Peruchó Á,

- Olalla C, Jiménez R (eds) Eurock 2014: Rock Engineering and Rock Mechanics: Structures in and on Rock Masses. CRC Press, Vigo, Spain, pp 463-468
- Valley B, Evans K (2015a) Methods for characterizing deep geothermal reservoirs from borehole measurements. In: Hirschberg S, Wiemer S, Burgherr P (eds) Energy from the Earth. vdf Hochschulverlag, pp 64-81
- Valley B, Evans KF Stress state at Soultz-sous-Forêts to 5 km depth from wellbore failure and hydraulic observations. In: Proceedings, 32nd workshop on geothermal reservoir engineering, 2007b. pp 17481-17469
- Valley B, Evans KF (2010) Stress heterogeneity in the granite of the soultz EGS reservoir inferred from analysis of wellbore failure, World Geothermal Congress 2010. In: Proceedings World Geothermal Congress 2010. International Geothermal Association, Bali, Indonesia,
- Valley B, Evans KF (2014b) Preliminary Assessment of the Scaling Relationships of In-Situ Stress Orientation Variations Indicated by Wellbore Failure Data. Paper presented at the ISRM Regional Symposium - EUROCK 2014, Vigo, Spain, 2014/1/1/
- Valley B, Evans KF Estimation of the stress magnitudes in Basel enhanced geothermal system. In: Proceedings World Geothermal Congress, Melbourne, Australia, 2015b. pp 19-25
- Valley B, Jalali MR, Ziegler M, Evans KF (2014) Constraining DFN characteristics for deep geothermal projects by considering the effects of fractures on stress variability, International Discrete Fracture Network Engineering Conference DFNE 2014. In. Vancouver, BC, Canada,
- Verscheure M, Fournon A, Chilès J-P (2012) Joint inversion of fracture model properties for CO2 storage monitoring or oil recovery history matching Oil & Gas Science and Technology–Revue d'IFP Energies nouvelles 67:221-235
- Vignerresse J-L, Tikoff B, Améglio L (1999) Modification of the regional stress field by magma intrusion and formation of tabular granitic plutons Tectonophysics 302:203-224



- Watanabe K, Takahashi H Fractal characterization of subsurface fracture network for geothermal energy extraction system. In: Proceedings, eighteenth workshop on geothermal reservoir engineering, Stanford University, Stanford, CA. Report No. SGP-TR-145-17, 1993.
- Wileveau Y, Cornet F, Desroches J, Blumling P (2007) Complete in situ stress determination in an argillite sedimentary formation *Physics and Chemistry of the Earth, Parts A/B/C* 32:866-878
- Williams-Stroud S, Kilpatrick J, Cornette B, Eisner L, Hall M (2010) Moving outside of the borehole: Characterizing natural fractures through microseismic monitoring *First Break* 28
- Yale DP (2003) Fault and stress magnitude controls on variations in the orientation of in situ stress *Geological Society, London, Special Publications* 209:55-64
- Zha Y, Yeh T-CJ, Illman WA, Tanaka T, Bruines P, Onoe H, Saegusa H (2015) What does hydraulic tomography tell us about fractured geological media? A field study and synthetic experiments *Journal of Hydrology* 531:17-30
- Ziegler M, Loew S, Bahat D (2014) Growth of exfoliation joints and near-surface stress orientations inferred from fractographic markings observed in the upper Aar valley (Swiss Alps) *Tectonophysics* 626:1-20
- Ziegler M, Loew S, Moore JR (2013) Distribution and inferred age of exfoliation joints in the Aar Granite of the central Swiss Alps and relationship to Quaternary landscape evolution *Geomorphology* 201:344-362
- Ziegler M, Valley B, Evans KF Characterisation of natural fractures and fracture zones of the Basel EGS reservoir inferred from geophysical logging of the Basel-1 well. In: *World Geothermal Congress Melbourne, Australia, 2015*. pp 19-25
- Zoback MD (2010) *Reservoir geomechanics*. Cambridge University Press,

Zoback MD et al. (2003) Determination of stress orientation and magnitude in deep wells  
International Journal of Rock Mechanics and Mining Sciences 40:1049-1076  
doi:<http://dx.doi.org/10.1016/j.ijrmms.2003.07.001>

# Appendix A

This appendix presents some analysis of the Chapter 2, which is not included in the final manuscripts.

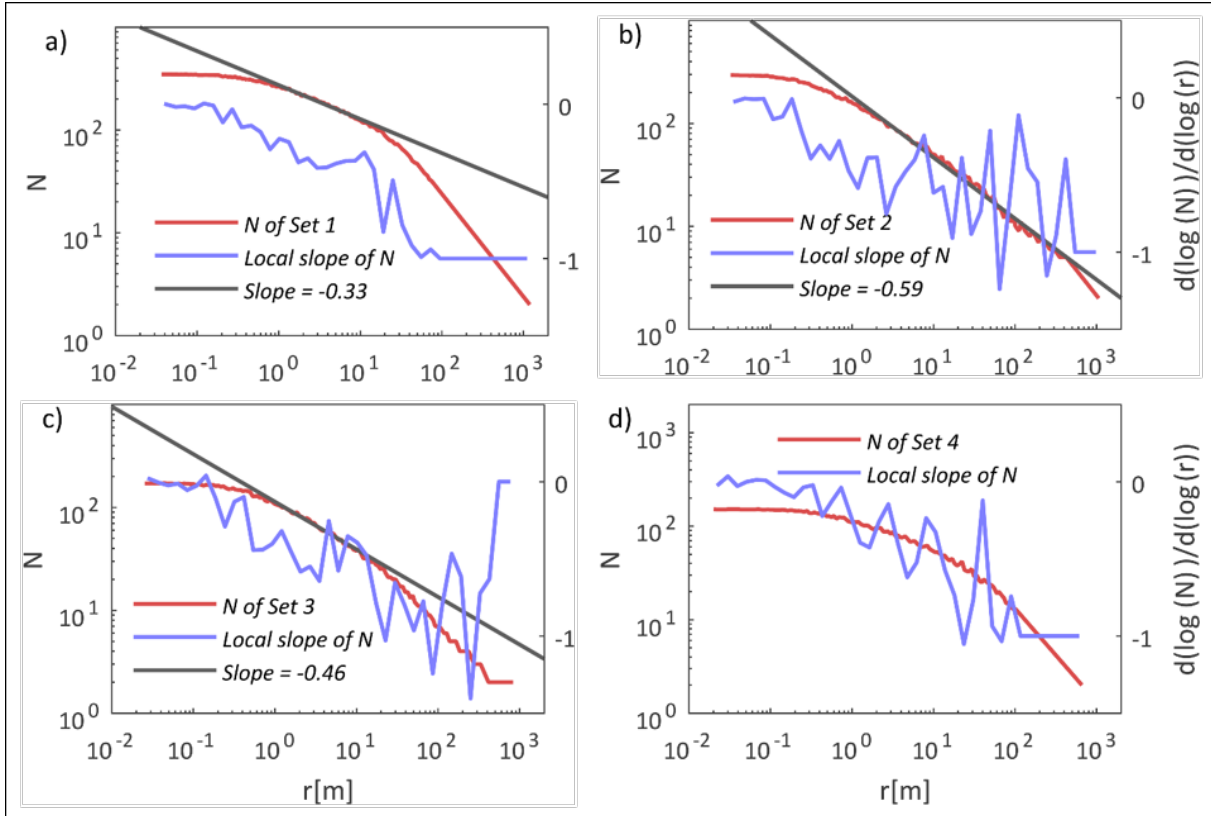


Figure A.1 Box counting analysis of different fracture sets from Basel-1 fracture sets.

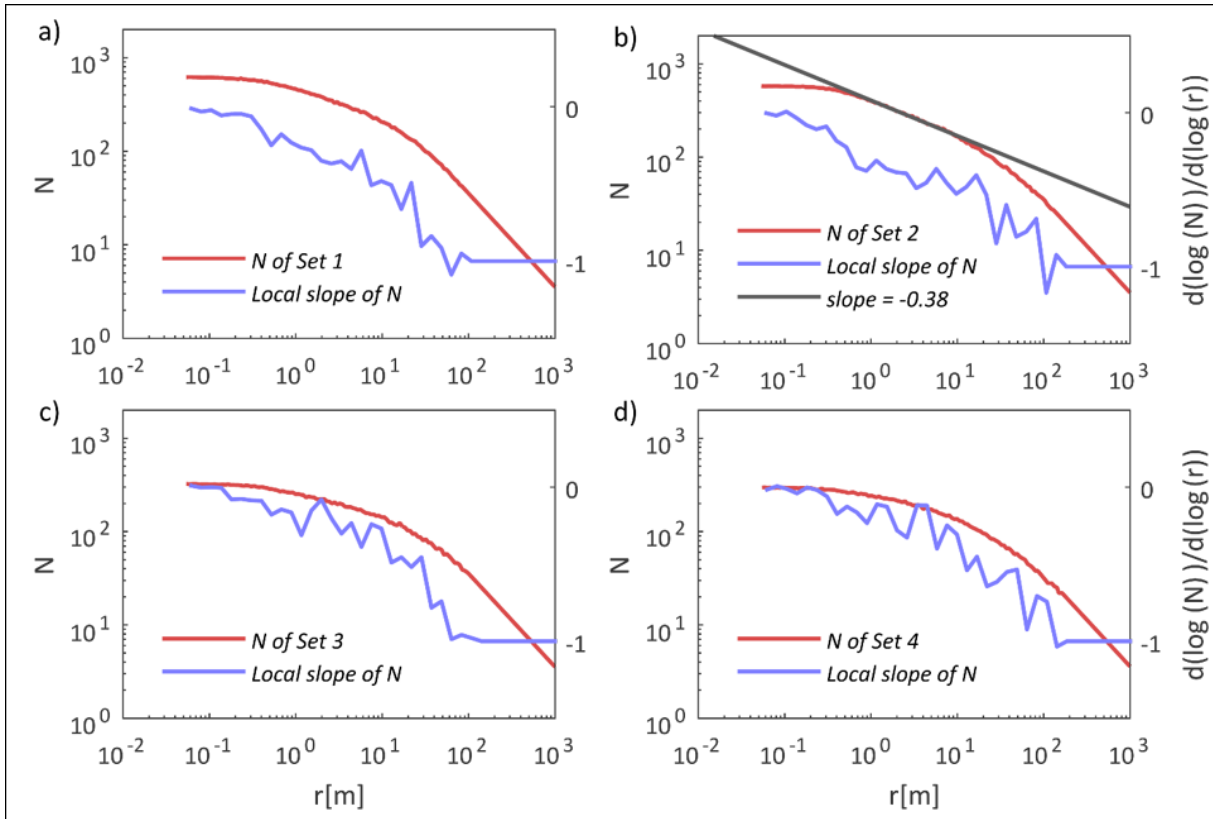


Figure A.2. Box counting analysis of different fracture sets from GPK3 fracture sets.

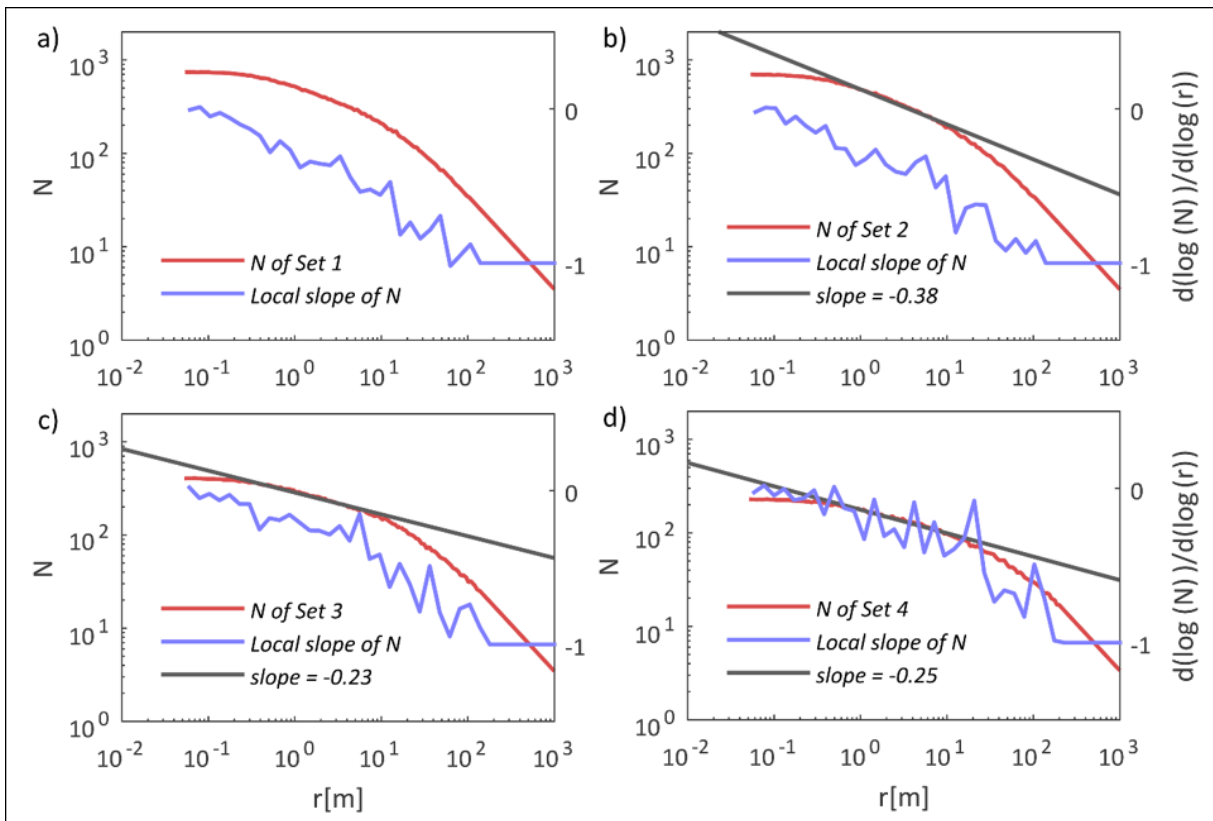


Figure A.3. Box counting analysis of different fracture sets from GPK3 fracture sets.

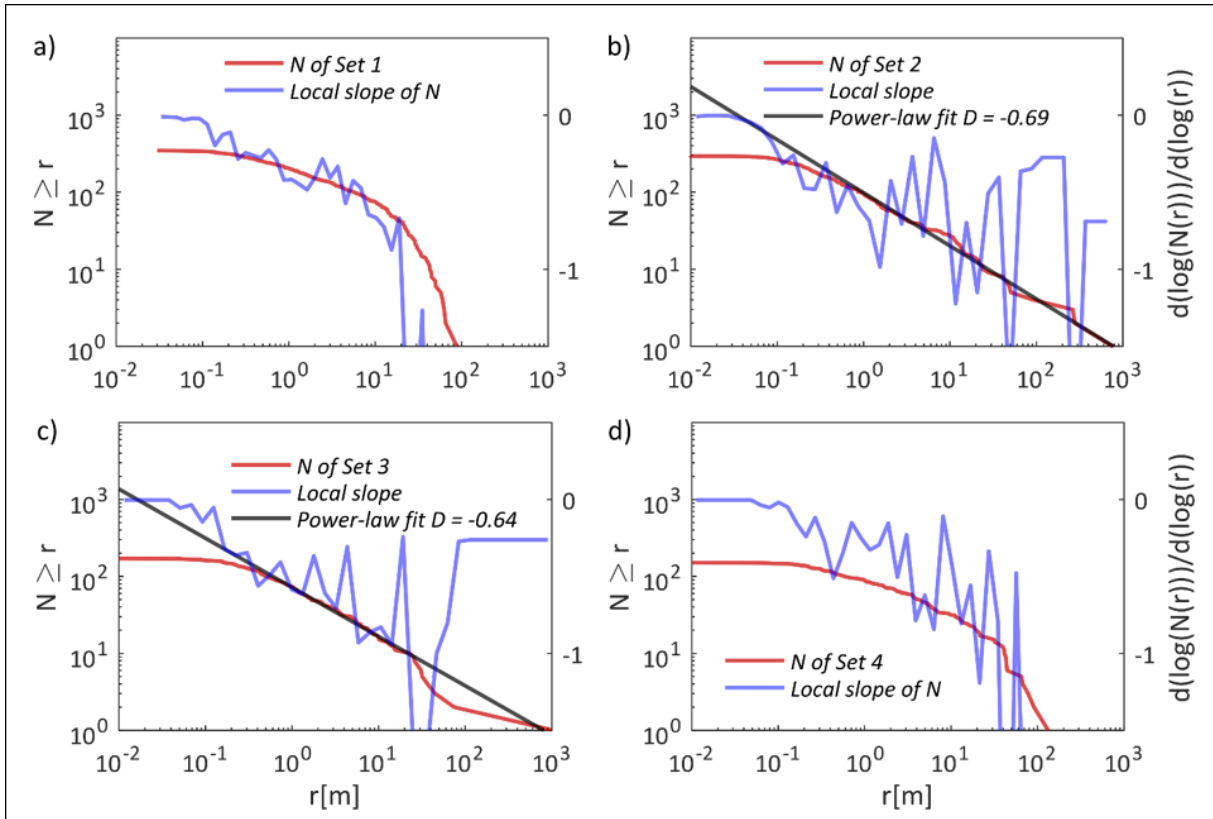


Figure A.4 Spacing distribution of different fracture sets from Basel-1 fracture sets.

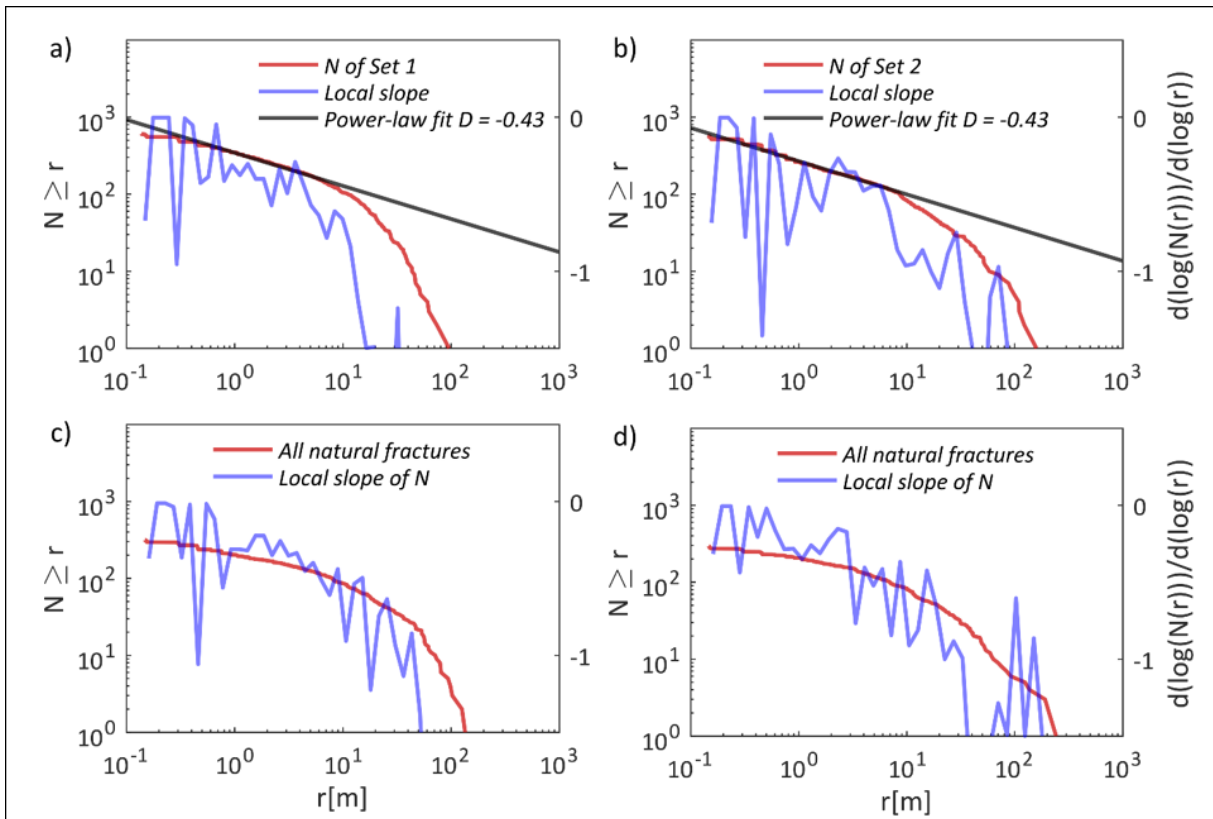


Figure A.5 Spacing distribution of different fracture sets from GPK3 fracture sets.

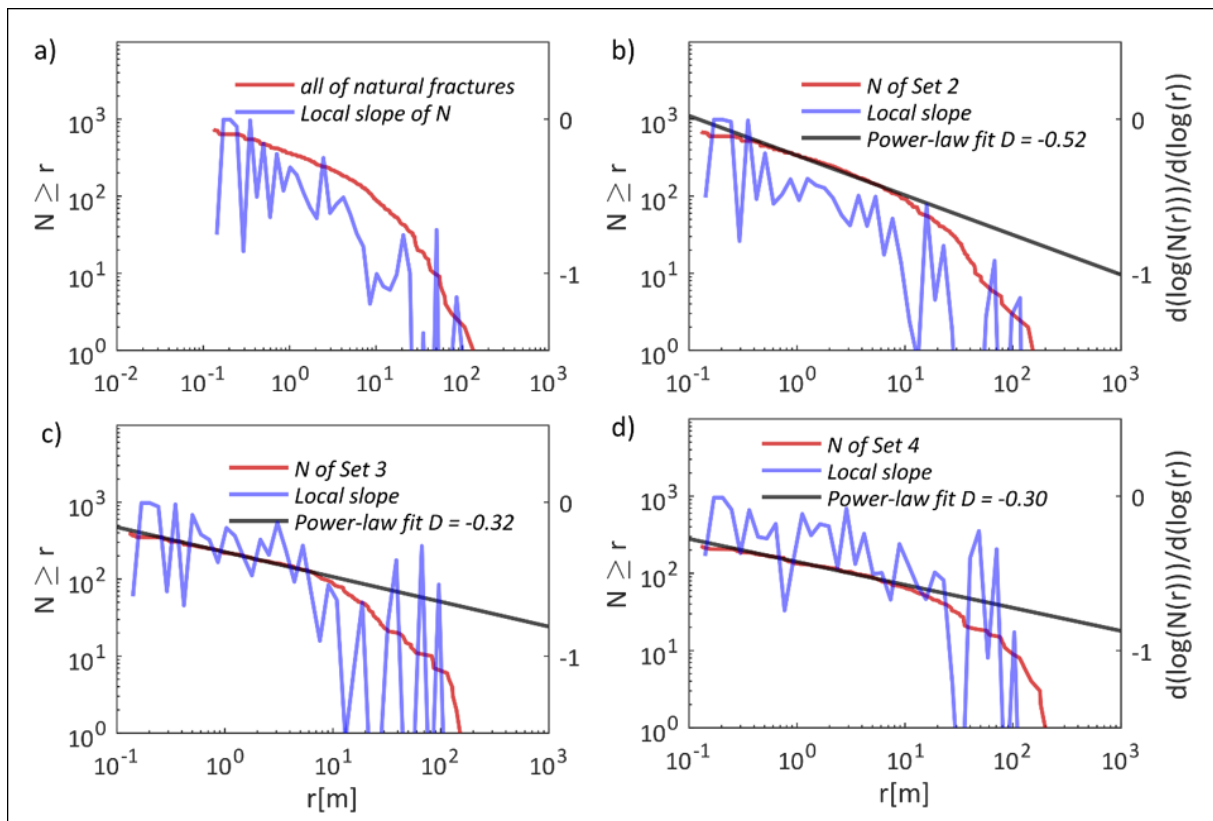


Figure A.6 Spacing distribution of different fracture sets from GPK4 fracture sets.

# Appendix B

---

Figure B.1a presents an example DFN generated using the dual power-law model. The initial parameters of this DFN are  $D=2.7$  and  $a=2.8$ . To verify the validity of the developed fracture network generator, we computed the corresponding correlation function of fracture centers and its local slope. Figure B.1b shows that the local slope is very close to the input correlation dimension (2.7). Furthermore, the cumulative fracture size distribution (Figure B.1c) follows a linear curve with a slope of -1.8 in log-log space. Bour and Davy (1999) demonstrated theoretically and numerically the correlation between the position and size of fractures in fractal network. If the frequency length distribution of fractures follows a power-law distribution with an exponent of  $a_f$  (i.e.  $n(l) = c \cdot l^{-a_f}$ ) and the fracture centers are distributed with a correlation dimension of  $D$ , equation B.1 relates  $a_f$  and  $D$ . In this equation,  $x$  is the exponent of a power-law relating the average center to center distance ( $d$ ) of a fracture to the closest fractures having a larger size in  $d(l) \sim l^x$ . Figure B.1d confirms the correlation between clustering and size distribution through the distance function. The exponent of  $x$  from the fit is very close to the computed value of  $x$  using equation 1 in the Supporting Information.

$$x = \frac{a_f - 1}{D} \quad (\text{B.1})$$

Here, we perform a sensitivity analysis on the maximum uncertainty of hypocentral ellipsoids on the 3D spatial distribution of microseismic events. We applied the same methodology, to generate random realizations with a noise in the location of hypocentres, as described in the Chapter 2. Figure B.2 shows that the effect of 9.3 m uncertainty is almost negligible on the resulting correlation dimension, while 93 m and 186 m uncertainties increase the correlation dimension to almost 3. This suggest that, if the uncertainty of hypocentral locations are high, the spatial clustering shows a uniform distribution in 3D space.

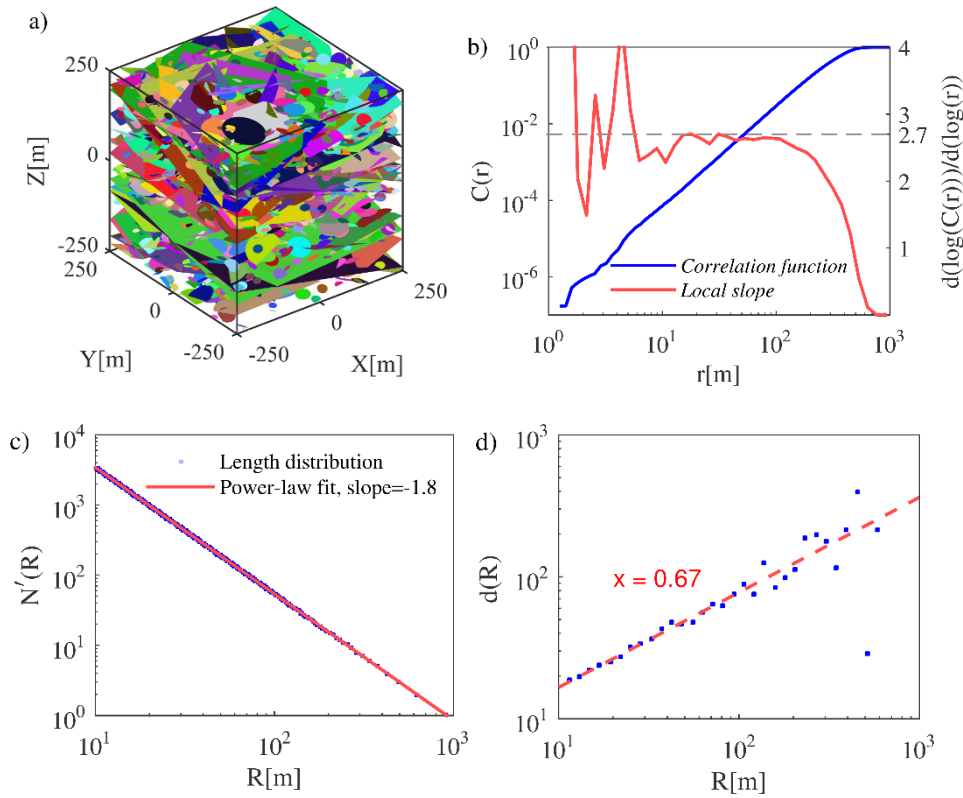


Figure B.1. a) A synthetic network generated using dual power-law model ( $D=2.7$  and  $a=2.8$ ). b) Correlation function and its local slope of the generated network. c) Complementary cumulative length distribution of the generated network ( $N'$  is the number of fractures larger than size of  $R$ ). d) Correlation between size and spatial distribution through distance function.

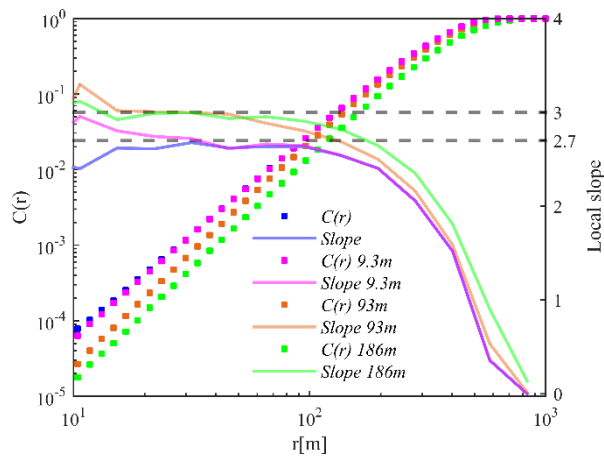


Figure B.2. A sensitivity analysis on the number of hypocentral uncertainty on the model presented in Figure 3-2a.

Here, we present the sensitivity of the correlation function to the number of repeating events. Applying the same methodology as presented in the Chapter 3, we change the number of repeaters. Figure B.3 shows that the sudden drop of the local slope is considerable when



approximately 100 repeaters exist. This is specific to the rupture model presented in Figure 3-2a.

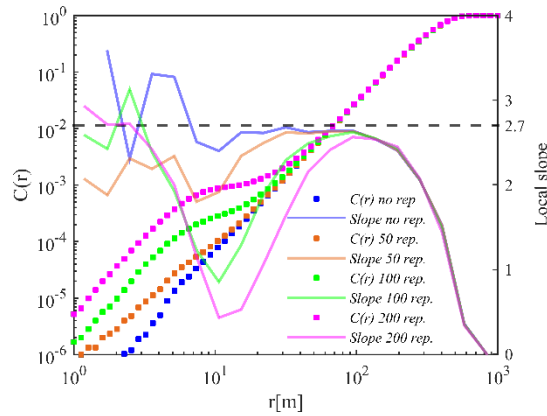


Figure B.3. A sensitivity analysis on the number of repeating events on the model presented in Figure 3-2a.

Here, we analyze the existence of three fractured zones with the same number of fractures but varying width. The sensitivity analysis shows that the denser the fractured zone, the higher impact on the correlation function as in Figure B.4.

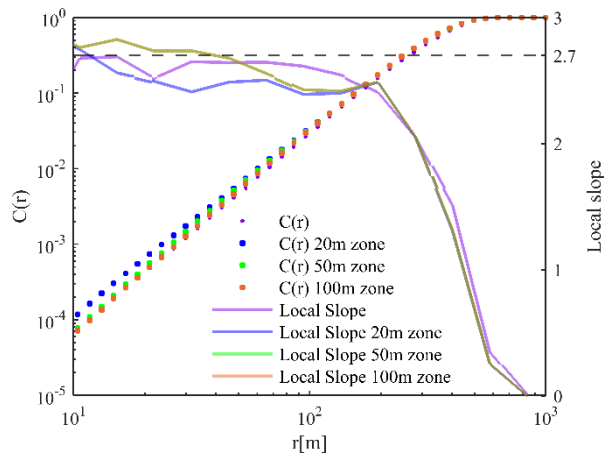


Figure B. 5. A sensitivity analysis on the width of the fractured zone on the model presented in Figure 3-2a.



# Appendix C

---

If the stress orientation profile from the synthetic case is selected as the only observation in the inversion process, the resulting probability map is not able to image the major features within the network. Figure C.1 (right) shows the resulting probability map compare to the initial DFN (left). The inversion is performed using the profile of Figure 4-3d and the initial information from Tables 4-1 and 4-2.

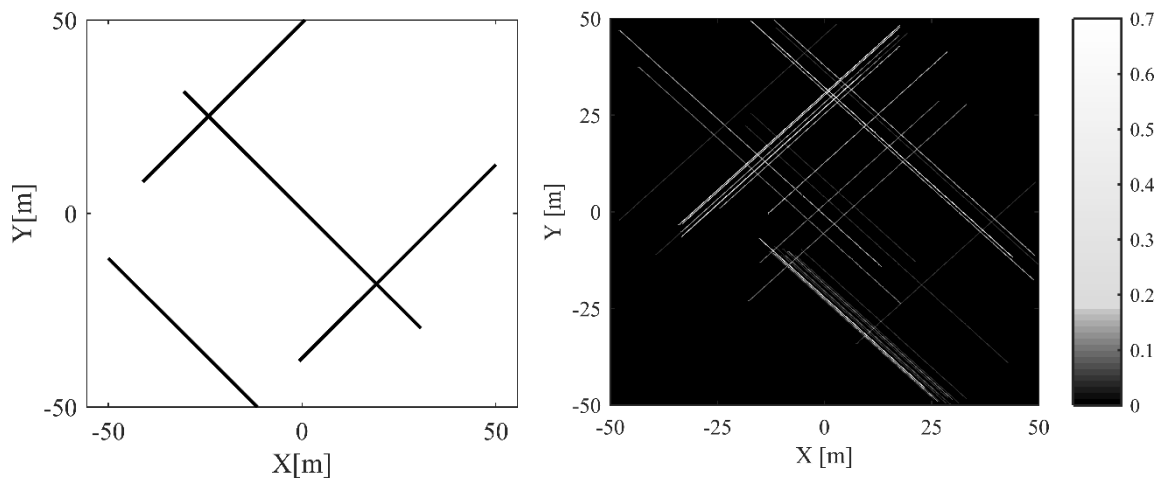


Figure C.1. The simple synthetic fracture network compared to the fracture probability map obtained from the inversion of stress orientation data.

The inversion process requires an initial DFN (as shown in Figure 4-2), which is randomly populated based on the prior information of Table 4-2. The following figure presents the initial DFN realizations to reconstruct the fracture network using the stress-based tomography. Figure C.2 (left and right) belong to the synthetic and outcrop-based fracture networks (presented as the test cases within the Chapter 4).

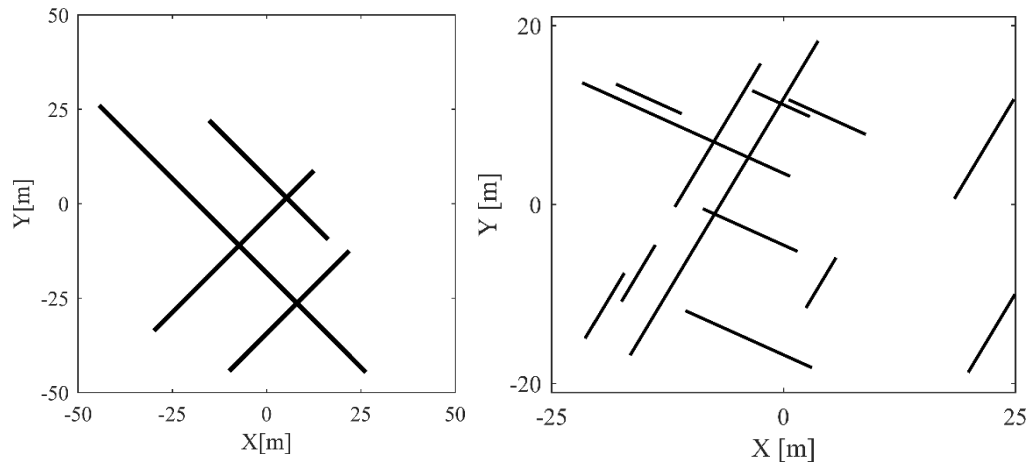


Figure C.2. The initial DFN realization in the inversion process of (left) synthetic network (right) outcrop-based network.

As it is discussed in the results, we assumed a very low friction angle to reconstruct the stress variabilities similar to the real field observations. However, one may question the impact of higher friction angles on the inversion process. Thus, a higher friction angle of  $35^\circ$  is selected to reconstruct the fracture network using stress based tomography. The other inversion parameters are kept unchanged (listed in table Tables 4-1 and 4-2). Figure C.3 represents the resulting probability map. Higher friction angles may result in lower degrees of stress variability, but stress-based tomography is still able to highlight the most important features within the network. Since the fracture strength parameters (shear and normal stiffness) are difficult to constrain, one may change them to reproduce comparable stress variabilities to borehole data.

Figure C.4 shows the strong similarity between the original and reproduced stress profile for both  $\sigma_1$  and  $\beta$  in a randomly chosen DFN from the ensemble. However, because of the higher complexity and small stress variabilities, the match is not as excellent as for the synthetic case.

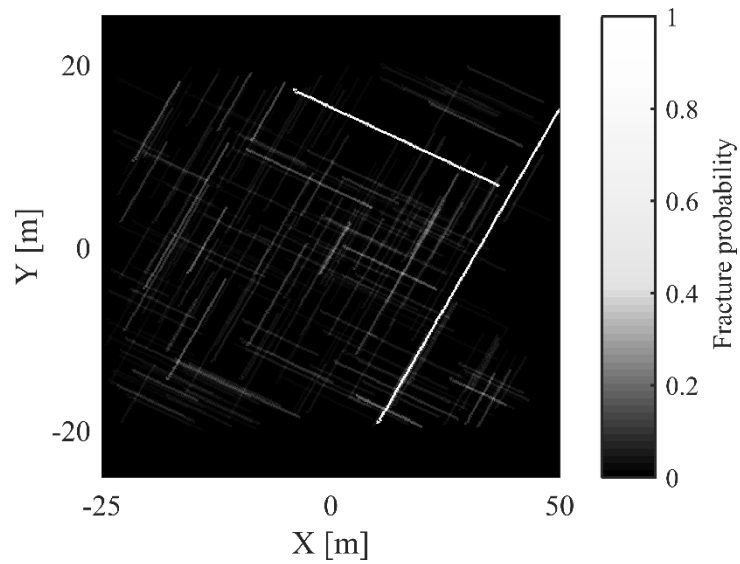


Figure C.3. Probability map of the inversion derived from the stress-based tomography of the outcrop0based case with a friction angle of  $35^\circ$ .

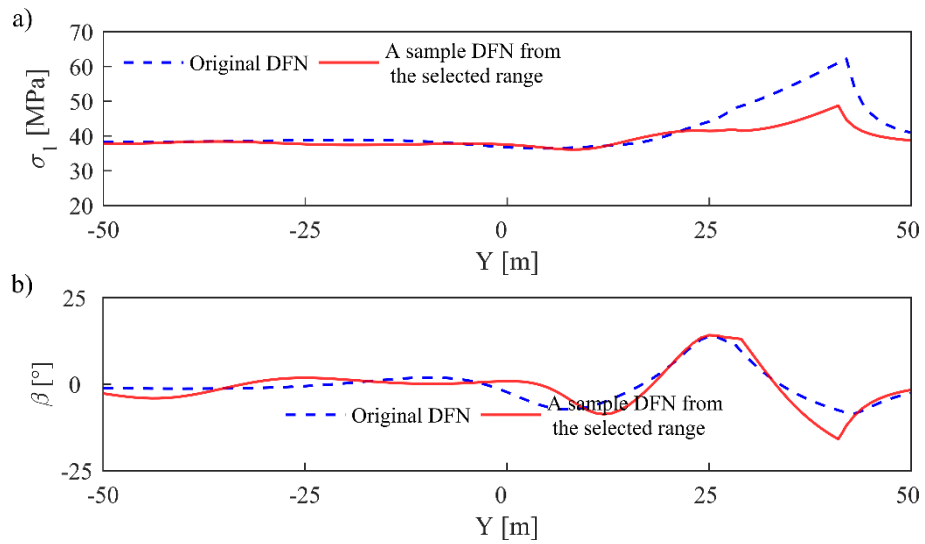


Figure C.4. Stress profiles of initial outcrop-based model with a friction angle of  $35^\circ$  compared to those of a randomly sampled DFN of the final ensemble.



## Curriculum Vitae



### Mohammad Javad, Afshari Moein

Nationality           Iran  
Birthdate             8 April 1988

### Education

March 2015- June 2018    Doctor of Science (Ph.D.), in Geothermics, Earth Science Department, Swiss Federal Institute of Technology (ETH), Zürich, Switzerland

Sep 2010 – Jan 2012    Master of Science (M.Sc.) in Reservoir Geoscience and Engineering, French Institute of Petroleum (IFP), Rueil Malmaison, France

Sep 2006 - Jun 2010       Bachelor of Science (B.Sc.) in Petroleum Engineering, Amirkabir University of Technology (Polytechnik Tehran), Tehran, Iran

### Honors and Awards

2013                    Member of National Foundation of Elites in Iran (Contributing to a research project instead of military service).

2010                    International Scholarship of TOTAL.

2010                    Rewarded 1<sup>st</sup> Rank Privileged B.Sc. Degree.

2008                    Rewarded Membership in Exceptional Talents Office, AUT

2006                    Ranked 777 in Nationwide University Entrance Exam.

### Journal Publications

Afshari Moein, M. J., Tormann, T., Valley, B., & Wiemer, S. (2018). *Maximum magnitude forecast in hydraulic stimulation based on clustering and size distribution of early microseismicity*. Geophysical Research Letters, 45, 6907–6917.

Afshari Moein, M.J., Valley, B., Evans, K.F., *Fractal scaling of fracture patterns in deep boreholes and implications to constrain discrete fracture network models*, Rock Mechanics and Rock Engineering Journal (Under review).

Afshari Moein, M.J., Somogyvari, M., Valley, B., Jalali, M.R., Loew, S., Bayer, P., *Fracture network characterization using stress-based tomography*, Journal of geophysical research, Solid-earth, (Under Review).

Afshari Moein, M.J., Valley, B., Jalali, M.R., *Linkage between scaling of fracture network, stress heterogeneities and microearthquakes*, (In Prep.).

Khormali A., Petrakov D.G., Moein M.J.A. (2016), *Experimental analysis of calcium carbonate scale formation and inhibition in waterflooding of carbonate reservoirs*, Journal of Petroleum Science and Engineering. 147, 843-850.

Shaabani, E., Rezaeian, M., Moein, M.J.A., Maarefvand, P. (2016), *Experimental investigation into rate of penetration in carbonated rocks*, International Journal of Oil, Gas and Coal Technology, 11, 339-349.

Rajabi A., Moein M.J.A., Rabbani A.R. (2015), *Improvement of petrophysical evaluation in a gas bearing carbonate reservoir—A case in Persian Gulf*, Journal of Natural Gas Science and Engineering, 24, 238-244.

Moein M.J.A., Shaabani E., Rezaeian M. (2014), *Experimental evaluation of hardness models by drillability tests for carbonate rocks*, Journal of Petroleum Science and Engineering. 113, 104-108.